Eidgenössische Technische Hochschule Zürich
Swiss Federal Institute of Technology Zurich

Master Thesis

Josephson Parametric Amplifiers with Lumped-element Coupled Resonators

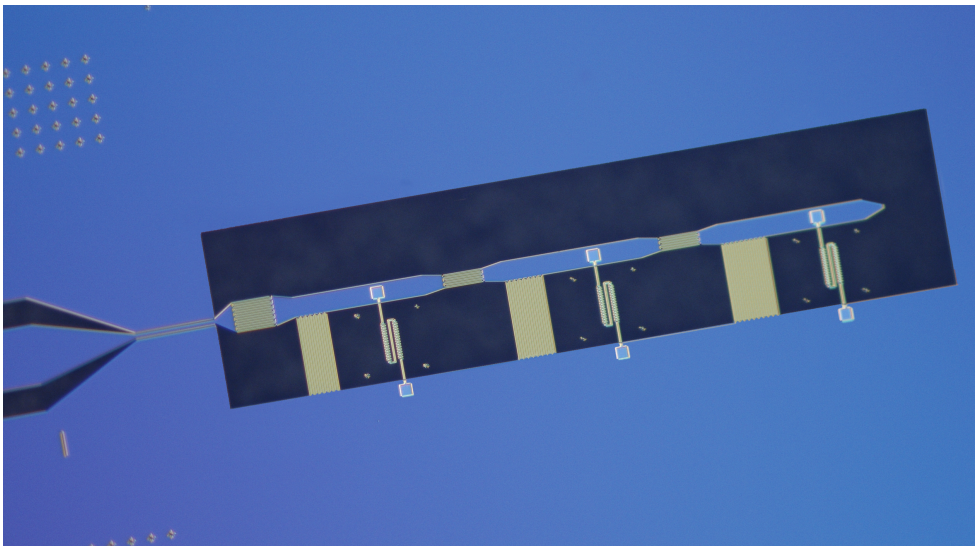

Author:
Antonio Rubio Abadal

Supervisor:
Dr. Anton Potočnik

Professor:
Prof. Andreas Wallraff

Quantum Device Lab
Laboratory for Solid State Physics
Eidgenössische Technische Hochschule Zürich

April 2015

I am a quantum engineer,
but on Sundays I have principles.

John Stewart Bell

Abstract

An array of coupled nonlinear cavities is a structure that could be used as a quantum simulator of strongly correlated quantum many-body systems. In the context of circuit quantum electrodynamics (circuit QED), such systems have been also found useful to build quantum-limited Josephson parametric amplifiers, since their multi-mode spectrum can be used to amplify signals at different frequencies while preserving their phase. In this thesis we describe and characterize lumped-element superconducting resonators both individually and in coupled arrays. A non-linearity is also added to the system by including arrays of Superconducting Quantum Interference Devices (SQUIDs), which are characterized and used to build a tunable three-mode parametric amplifier.

Contents

Chapter 1

Introduction

The progress in the control and manipulation of quantum systems has experienced remarkable advances in the last decade, as shown by the recent work in atomic ensembles, photonic systems and solid-state platforms like superconducting circuits [1]. All these different systems with their complementing advantages are opening up new possibilities for the development of quantum technologies based on quantum information processing. One clear example of such a quantum technology is the field of Cavity Quantum Electrodynamics (Cavity QED), studied both in the optical and microwave regimes and in mirror and circuit-based platforms [2–4]. In this context, a particularly attractive system is an array of coupled nonlinear cavities. These kind of systems can improve our understanding of the interaction between light and matter, but they could also be potentially used as photonic quantum simulators [5–8].

Coupled nonlinear cavities are also applicable to the construction of quantum-limited Josephson parametric amplifiers (paramps)[9]. Such amplifying devices are essential for many of the experiments routinely performed in the field of circuit QED, and have allowed for example to measure quantum trajectories [10], higher order correlation functions [11] or quantum feedback [12]. The increasing requirements for these devices have stimulated the creation of several paramps with different architectures. While several of these Josephson paramps are based on coplanar waveguide resonators [13], lumped-element resonator based paramps have recently also been studied [9, 14], since they offer advantages such as compact design and improved bandwidth characteristics.

For both the designs of parametric amplifiers and analog quantum simulators, a precise understanding and control over the different parameter contributions in the Hamiltonian which describes the system is necessitated. The basic step to achieve this understanding is the development and testing of simple models. These models are usually based on an equivalent electrical circuit when describing systems of circuit QED, as they offer simplicity but still accurate results.

In this thesis, the design and experimental characterization of lumped-element superconducting resonators have been performed, and the resonator circuit parameters have been extracted from their measurement, which has been used to create a design model for the fabrication of resonators with precise parameters. One-dimensional resonator arrays have also been studied and modelled by using both circuit theory and a Hamiltonian description, and measurements were compared to the expected results from our design model.

In addition, one-dimensional arrays of nonlinear resonators have also been built, by substituting the meander inductor with arrays of superconducting quantum interference devices (SQUIDs). These nonlinear resonator arrays show tunable resonance frequencies and performance of degenerate and non-degenerate parametric amplification. Gain curves and parametric amplification phase diagrams have been measured for both a single nonlinear resonator and an array of three nonlinear resonators and compared to the theoretical predictions.

Chapter 2

Lumped elements in microwave circuits

The lumped-element model is a simplification of a spatially-distributed electrical system which can describe its behaviour when certain conditions, as an inappreciable phase delay, are fulfilled [15]. In the field of microwave circuits, passive components like inductors or capacitors can be defined as lumped or quasi-lumped elements due to their small electrical size, in particular when its physical dimensions are much smaller than the electrical wavelength [16]. These kind of components offer practical advantages, aside from being easily modelled, such as their compact size and wider bandwidth characteristics. In this chapter we will treat their physical description and comment on their main properties.

2.1 Lumped-element model of a transmission line

To get a good understanding of lumped elements in microwave circuits it is important to first understand transmission line theory, especially as the design of microwave lumped elements is based on small sections of TEM (Transverse Electromagnetic) lines. In contrast to circuit theory, where an electrical network is represented by idealized electrical components with the same current and voltage over their dimensions, in transmission line theory we deal with a network of distributed parameters.

We can model an homogeneous transmission line as an infinite array of lumped elements [15, 16], such that a small section can be represented as shown in figure 2.1. In this figure r represents the resistance of the individual conductors, g the dielectric loss of the material between the two conductors, l the self-inductance and c the capacitance between the two conductors, all defined per unit length. We can even go one step further and neglect the losses of the system which are usually very small, specially for superconducting structures, therefore working with a lossless transmission line model, where r, $g = 0$.

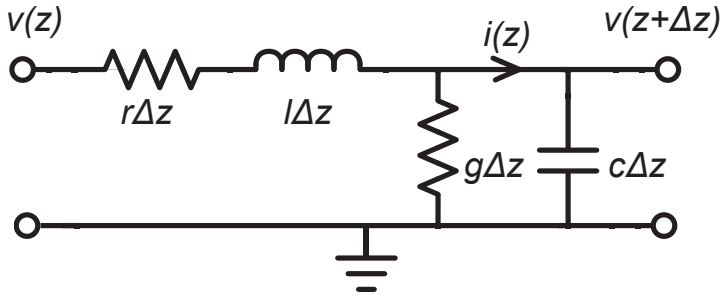

FIGURE 2.1: Lumped-element model of an infinitessimal part of a transmission line.

With this simplified model, we can apply Kirchhoff's laws and obtain the expressions

$$v(z,t) - l\,\Delta z\,\frac{\partial i(z,t)}{\partial t} = v(z+\Delta z,t), \tag{2.1}$$

$$i(z,t) - c\,\Delta z\,\frac{\partial v(z,t)}{\partial t} = i(z+\Delta z,t). \tag{2.2}$$

If we now divide these two expressions by Δz and evaluate the limit when Δz goes to 0, we can rewrite the expressions as:

$$\frac{\partial v(z,t)}{\partial z} = -l\,\frac{\partial i(z,t)}{\partial t}, \tag{2.3}$$

$$\frac{\partial i(z,t)}{\partial z} = -c\,\frac{\partial v(z,t)}{\partial t}, \tag{2.4}$$

which are known as the *telegrapher equations* for historical reasons [15]. If we consider a harmonic steady-state excitation, the previous expressions simplify to

$$\frac{dV(z)}{dz} = -j\omega l\,I(z), \tag{2.5}$$

$$\frac{dI(z)}{dz} = -j\omega c\,V(z), \tag{2.6}$$

where $j = \sqrt{-1}$. If we now take the spatial derivative of both of these expressions we get to the wave equations

$$\frac{d^2V(z)}{dz} - \gamma^2\,V(z) = 0, \tag{2.7}$$

$$\frac{d^2I(z)}{dz} - \gamma^2\,I(z) = 0, \tag{2.8}$$

where $\gamma = j\beta = j\omega\sqrt{l\,c}$ is an imaginary propagation constant. The solutions are found to be

$$V(z) = V_0^+ e^{-j\,\beta\,z} + V_0^- e^{j\,\beta\,z}, \tag{2.9}$$

$$I(z) = \frac{V_0^+}{Z_0}\,e^{-j\,\beta\,z} - \frac{V_0^-}{Z_0}\,e^{j\,\beta\,z}, \tag{2.10}$$

where $Z_0 = \sqrt{l/c}$ is the characteristic impedance of the transmission line, which is typically $Z_0 = 50\,\Omega$. Now from the travelling wave equations we can extract the wavelength which is

$$\lambda = \frac{2\pi}{\beta} = \frac{2\pi}{\omega\sqrt{l\,c}}, \tag{2.11}$$

and the phase velocity

$$v_p = \frac{\omega}{\beta} = \frac{1}{\sqrt{l\,c}}. \tag{2.12}$$

2.2 Design and description of microwave lumped elements

In the field of microwave circuits a lumped element is defined as a passive electrical component with no appreciable phase delay between its input and output terminals. This implies, as we will show next, that the size of the lumped element will always be much smaller than the operating wavelength of the circuit. If we take the travelling wave solutions for a homogeneous transmission line from the previous section, we can see that the phase delay of a particular component will be negligible when $j\beta d \approx 0$, where d is the size of the component. This can be rewritten as

$$\beta d = \omega\sqrt{lc}\,d = \frac{\omega\,d}{v_p} = \frac{2\pi v_p}{\lambda}\frac{d}{v_p} = 2\pi\frac{d}{\lambda} \approx 0, \tag{2.13}$$

which clearly shows that the phase delay will be small whenever the size of the element is much smaller than the operating wavelength. This derivation can also be written as a function of the operating frequency

$$\beta d = \omega\sqrt{lc}\,d = \omega\sqrt{(l\,d)(c\,d)} = \frac{\omega}{f_s} = 2\pi\frac{f}{f_s} \approx 0, \tag{2.14}$$

where f_s is the so-called self-resonant frequency of a homogeneous transmission line. For an arbitrary piece of TEM line the values of l and c will not be homogeneously distributed over its length but it will still have a self-resonant frequency. This is the frequency at which the total reactance of the component becomes zero [16]. This will actually happen for an infinite amount of self-resonant frequencies, but we will usually always mean the first lowest self-resonant frequency of the system.

We have seen then that a component will be considered a lumped element when the operating frequency or the size of the component is much smaller than the self-resonant frequency or the operating wavelength respectively. In microwave circuits a general guideline for constructing a lumped element is keeping the maximum dimension of the element 20 times smaller than the operating wavelength [16]. Having these basic definitions in mind, we will show how a transmission line can be terminated to obtain the main lumped-element building blocks in microwave circuits: inductors, capacitors and resistors.

2.2.1 The terminated lossless transmission line

In figure 2.2 a lossless transmission line of length d and characteristic impedance Z_0 terminated with a load of impedance Z_L is shown. If the impedance Z_L is allowed to have any arbitrary value, any incident wave coming from a source from the left port of the transmission line will be partially reflected by the load due to the impedance mismatch and therefore the total voltage and current in the transmission line will be represented by the general solution showed in equations 2.9 and 2.10. At the terminal of the load the total current and voltage will have to fullfill the condition

$$Z_L = \frac{V}{I} = \frac{V_L^+ + V_L^-}{V_L^+ - V_L^-} Z_0. \tag{2.15}$$

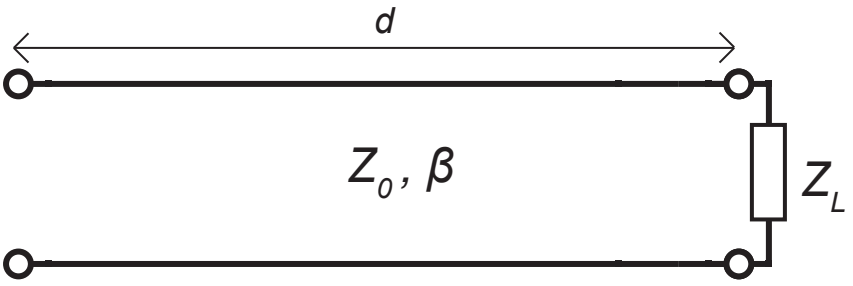

FIGURE 2.2: Transmission line of length d terminated with a load of impedance Z_L.

Having this expression we can now derive the value of the voltage reflection coefficient Γ:

$$\Gamma = \frac{V_L^+}{V_L^-} = \frac{Z_L - Z_0}{Z_L + Z_0}. \tag{2.16}$$

The reflection coefficient Γ is the ratio between the incoming and reflected voltages by the load. Now we can write the total voltage and current at the input ports of the transmission line as

$$V_{in} = V_L^+ (e^{-j\beta d} + \Gamma e^{j\beta d}), \tag{2.17}$$

$$I_{in} = \frac{V_L^+}{Z_0}(e^{-j\beta d} - \Gamma\, e^{j\beta d}). \tag{2.18}$$

From these two equations we can derive the expression for the input impedance, which is the impedance seen looking into the line from the input port:

$$Z_{in} = \frac{V_{in}}{I_{in}} = \frac{1 + \Gamma\, e^{-2j\beta d}}{1 - \Gamma\, e^{-2j\beta d}} Z_0, \tag{2.19}$$

which by using the expression of the reflection coefficient Γ we can rewrite as

$$\begin{aligned} Z_{in} &= \frac{(Z_L + Z_0)\, e^{j\beta d} + (Z_L - Z_0)\, e^{-j\beta d}}{(Z_L + Z_0)\, e^{j\beta d} - (Z_L - Z_0)\, e^{-j\beta d}}\, Z_0 \\ &= \frac{Z_L \cos\beta d + j Z_0 \sin\beta d}{Z_0 \cos\beta d + j Z_L \sin\beta d}\, Z_0 \\ &= Z_0\, \frac{Z_L + j Z_0 \tan\beta d}{Z_0 + j Z_L \tan\beta d}. \end{aligned} \tag{2.20}$$

2.2.2 Inductor

With the expression of the input impedance of a terminated lossless transmission line we will show that a load with zero impedance will yield a lumped-element inductor for short transmission lines [16]. An inductor is a passive electrical component which stores and releases magnetic energy. In its ideal representation it does not store any electrical energy and it does not dissipate power. It is characterized by its inductance, which quantifies the amount of voltage induced by a change in the current flowing through the inductor. This is mathematically expressed by the relation

$$v(t) = L\, \frac{di(t)}{dt}, \tag{2.21}$$

which if we assume an harmonic time dependence ($e^{j\omega t}$) can be rewritten as

$$v = j\omega L\, i. \tag{2.22}$$

The expression of the impedance of an inductor at a particular frequency is written as

$$Z_{\text{inductor}} = j\omega L = j\, 2\pi f L. \tag{2.23}$$

Now let us go back to equation 2.20 and consider a load with impedance $Z_L = 0$. In this case the input impedance will take the form:

$$Z_{in} = j Z_0 \tan\beta d = j Z_0 \left(\beta d + \frac{1}{3}\,(\beta d)^3 + ...\right) \tag{2.24}$$

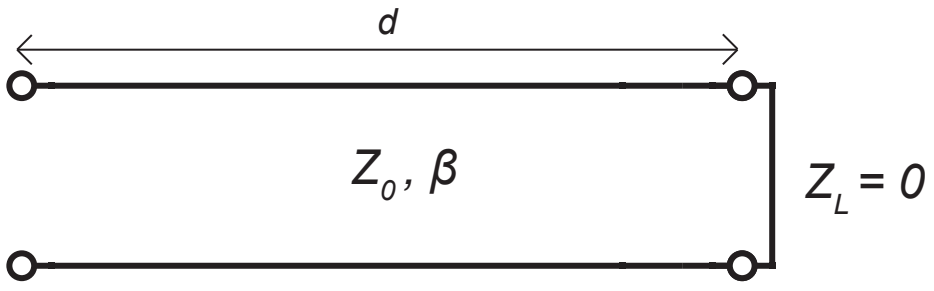

FIGURE 2.3: Transmission line of length d terminated with a load of impedance $Z_L = 0$.

which by considering the lumped-element approximation for the transmission line $\beta d \approx 0$ for small d we can approximate the input impedance as

$$Z_{in} \approx \frac{jZ_0}{1/\beta d - \beta d/3} = \frac{j\sqrt{\frac{l}{c}}}{1/\omega\sqrt{lc}\,d - \omega\sqrt{lc}\,d/3}$$

$$= \frac{1}{1/j\omega\,l\,d + j\omega\,cd/3} = \frac{1}{1/j\omega L + j\omega C/3}, \tag{2.25}$$

where $L = l\,d$ is the total inductance of the transmission line and $C = cd$ is the total capacitance of the transmission line. We can see that matches with the impedance of an ideal inductor in parallel with a parasitic capacitor. We therefore can conclude that a lumped-element inductor can be designed by a shortcutted ($Z_L = 0$) transmission line with dimensions much smaller than the operating wavelength. The value of the inductance can be engineered by changing the inductance per unit length of the transmission line, i.e. by using different geometries or materials.

2.2.3 Capacitor

An ideal capacitor is an electric passive component which does not dissipate energy and which stores and releases electrostatic energy. The electrostatic energy is stored between two conductors separated by a dielectric. It is characterized by its capacitance, which is defined as the ratio between the stored charges and the voltage. We can write this mathematically as

$$C = \frac{q}{v}, \tag{2.26}$$

which by rearranging the terms and applying a time derivative yields the relation

$$i(t) = C\,\frac{dv(t)}{dt}. \tag{2.27}$$

Assuming the harmonic time dependence we can obtain

$$i = j\omega C\,v. \tag{2.28}$$

From the above expression we can derive the impedance of the capacitor at a given frequency:

$$Z_{\text{capacitor}} = \frac{1}{j\omega C}. \tag{2.29}$$

Now, we go back to equation 2.20 and consider the case where the load has an infinite impedance. In this case the input impedance will take the form:

$$Z_{in} = \frac{-jZ_0}{\tan\beta d} = \frac{-jZ_0}{\beta d + \frac{1}{3}(\beta d)^3 + ...}. \tag{2.30}$$

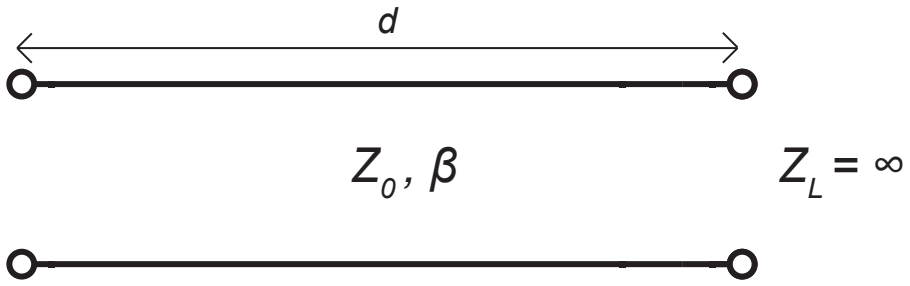

FIGURE 2.4: Transmission line of length d terminated with a load of impedance $Z_L = \infty$.

Considering the lumped-element approximation for the transmission line ($\beta d \approx 0$) we can approximate the input impedance as

$$Z_{in} \approx \frac{-jZ_0}{\beta d} + \frac{jZ_0\beta d}{3} = \frac{\sqrt{\frac{l}{c}}}{j\omega\sqrt{l\,c}\,d} + \frac{j\sqrt{\frac{l}{c}}\,\omega\sqrt{l\,c}\,d}{3}$$

$$= \frac{1}{j\omega c\,d} + \frac{j\omega l\,d}{3} = \frac{1}{j\omega C} + \frac{j\omega L}{3}, \tag{2.31}$$

where again $C = cd$ is the total capacitance of the transmission line and $L = ld$ is the total inductance of the transmission line. In this case we have seen how an open transmission line ($Z_L = \infty$) is the model for designing lumped-element capacitors, with a small parasitic inductive contribution. The distance between the two conductors and the material of the dielectric can be changed to achieve a desired capacitance.

2.3 Parasitics and effective element values

In the previous section we have shown how small sections of transmission lines can be modelled as purely capacitive or inductive lumped elements. In reality, however, ideal lumped elements are not realizable at microwave frequencies, since due to fringing fields all components will always store both magnetic and electric energy. These effects need to be taken into account for having a complete description of the system. This is usually done by a lumped-element equivalent circuit, which takes into account the parasitic reactances. Such models can be obtained either from the simulation or the measurement of the components.

To give an idea of how to model parasitic reactances in lumped-elements, we will here derive the effective inductance of a non-ideal lumped-element inductor. The main reactive parasitic contributions in inductors come from the parasitic capacitance due to the interturn and ground plane effect[16]. We can model such parasitic capacitance as a capacitor in parallel to our ideal inductor. The total

impedance of the circuit is

$$Z_{L'} = \frac{1}{j\omega L + \frac{1}{j\omega C_P}} = \frac{j\omega L}{1 - \omega^2 L\, C_P} = j\omega\, L_e, \tag{2.32}$$

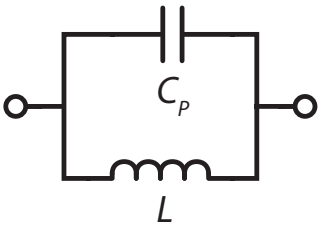

FIGURE 2.5: Equivalent circuit of a lumped-element inductance with parallel parasitic capacitance C_P.

from which we can directly extract the value of the effective inductance as

$$L_e = \frac{L}{1 - \omega^2 L\, C_P} = \frac{L}{1 - (\omega/\omega_S)^2}, \tag{2.33}$$

where $\omega_S = 1/\sqrt{L\, C_P}$ is the self-resonant frequency of the inductor. At frequencies smaller than ω_S the effective inductance will be close to L, but as the frequency gets closer to the first self-resonant frequency, the capacitive contribution will become stronger, yielding an effective larger value of the inductance.

In the case of capacitors, a parasitic inductance is modelled in series, which for the particular case of interdigital capacitors will come from the inductance of the fingers. The total impedance will then be

$$Z_{C'} = \frac{1}{j\omega C} + j\omega L_P = \frac{1}{j\omega C}\,(1 - \omega^2 L_P\, C) = \frac{1}{j\omega\, C_e}, \tag{2.34}$$

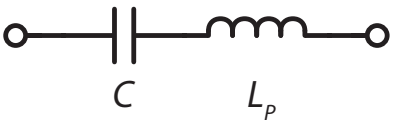

FIGURE 2.6: Equivalent circuit of a lumped-element capacitance with series parasitic inductance L_P.

where the effective capacitance is written as

$$C_e = \frac{C}{1 - \omega^2 L_P C} = \frac{C}{1 - (\omega/\omega_S)^2}. \tag{2.35}$$

Here the self-resonant frequency of the capacitor is defined as $\omega_S = 1/\sqrt{L_P C}$. Interestingly, these effective models will result in the same, but renormalized, reactive element as long as $\omega < \omega_S$. When $\omega > \omega_S$, the character of the effective elements is changed, and effective capacitors will become inductive and vice versa [16].

Chapter 3

Design of lumped-element superconducting resonators

In this chapter we will describe the main characteristics of the design of our lumped-element superconducting resonators. We will first describe the general details of the design, and then focus on each of the individual components of the resonator and how its values can be estimated by simulations and model calculations. The behaviour of parasitic reactances will also be studied with a high-frequency electromagnetic simulation to estimate the validity of the lumped-element approximation. In the last part of the chapter we will review the different alternative geometries considered for one resonator and also how these designs are adapted to couple several linear and nonlinear resonators.

3.1 General design

The structure of our resonators is based on an LC circuit where the energy oscillates from being stored in the electric field of the capacitor to the magnetic field of the inductor. These components have been designed as microwave lumped elements, based on the derivations in chapter 2. The inductors will be built as a planar meander line, while the capacitors will have a multi-finger periodic structure, known as interdigital capacitors. A typical structure of a resonator can be seen in figure 3.1, in which we can identify the shunt interdigital capacitor, the meander line inductor and the interdigital coupling capacitor. In the design of the figure, the capacitor and the inductor form a parallel LC circuit connected by a thick island line, in series with the external coupling capacitor.

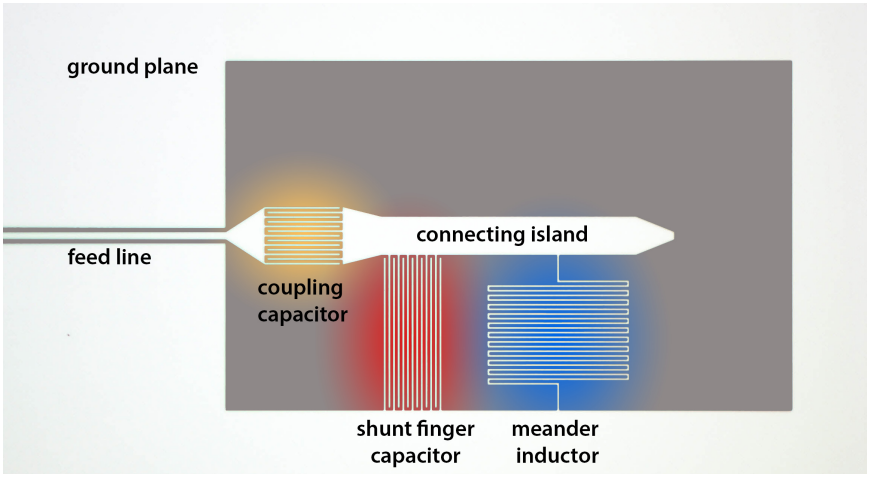

FIGURE 3.1: Picture of a single lumped-element resonator. The white region corresponds to the niobium while the gray region to the sapphire.

Our design choice is based on maximizing the distance between the components and the ground plane, which reduces the stray capacitance contribution. Also a rather large width of the island has been chosen to reduce the undesirable contribution to the inductance from the island. The length of the island was optimized to also reduce the island inductance but at the same time reduce the mutual capacitance between the capacitor and the inductor.

The circuit is structured into a superconducting layer of niobium on top of a sapphire substrate. The fabrication process is done on a niobium-sputtered 2-inch sapphire wafer, with a niobium thickness of 150 nm and a sapphire substrate thickness of 0.43 mm, using a photolithographic process. Niobium, a type II superconductor, becomes superconducting at a $T_c \approx 9.2$ K. Although superconductors are dissipationless, our resonators will be modelled as a RLC circuit, since other losses are important, such as dielectric losses in the capacitor electric fields.

The design of parametric amplifiers requires non-linear resonators. For these we will use a similar design with the meander inductor being substituted by an array of SQUIDs made of aluminium. These SQUIDs will be fabricated on top of the niobium and sapphire structures by using electron-beam lithography, since the feature sizes will be much smaller than the linear structures. Aluminium is superconducting at $T_c \approx 1.2$ K, and will therefore require dilution refrigerator temperatures to be measured.

3.2 Interdigital Capacitors

At microwave frequencies there are several capacitor design possibilities, and for our purposes, interdigital capacitors offer the simplicity of an integrated capacitor without the need of a multilevel process in the fabrication and with moderate

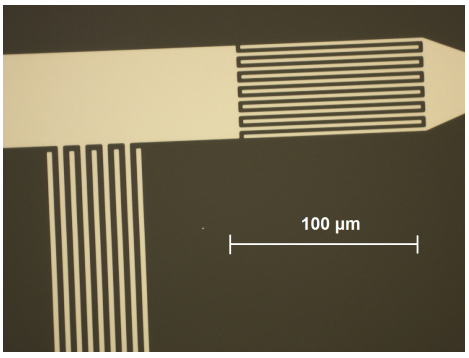

FIGURE 3.2: Detailed micrograph of the two finger capacitors in our resonators.

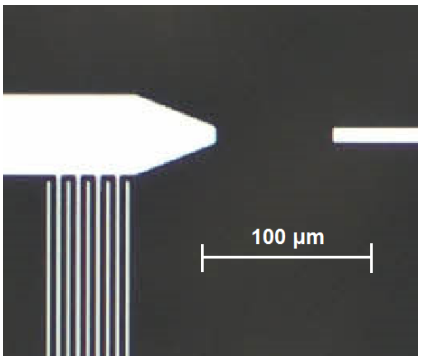

FIGURE 3.3: Detailed micrograph of a coupling gap capacitor in our resonators.

capacitance values. A micrograph where two of our interdigital capacitors can be seen is shown in figure 3.2. Interdigital capacitors usually display higher quality factors than overlay capacitors, but tend to be larger in size as the capacitance per area is much less than for the overlay type [16].

An interdigital capacitor has a multifinger periodic structure and the capacitance is given by the narrow gaps between the superconducting fingers. These gaps tend to be long and meandered in order to maximize the exposed area between the two superconducting structures, forming two electrodes of interdigitated fingers. The capacitance can be increased either by increasing the finger length or the number of fingers. However, by doing the latter we will also reduce the parasitic series capacitance, which would otherwise increase by making longer fingers.

3.2.1 Capacitors design parameters

There are several parameters of the interdigital capacitor that can be adapted during the design, such as the finger length, the gap and finger widths or the distance between the sides. However, for most of our resonators we will vary only the number of fingers of the capacitor and keep the other parameters constant. In table 3.1 we show the typical chosen parameters for both shunt and coupling capacitors.

SHUNT CAPACITOR		COUPLING CAPACITOR	
Finger length	197 μm	Finger length	97 μm
Finger width	3 μm	Finger width	3 μm
Finger gap	3 μm	Finger gap	3 μm
Standard num. of fingers	9	Typ. num. of fingers	0-20

TABLE 3.1: Design details of the interdigital capacitors used in our resonators.

To achieve very weakly coupled resonators, it is also necessary to use so-called gap coupling capacitors, as the one shown in figure 3.3. The width is always of

10 μm, and the gap length ranges from 3 to 70 μm for extremely weakly coupled samples.

3.2.2 Maxwell simulations

To estimate the expected capacitance values before fabrication we perform dc simulations of our capacitive structures using the commercial electromagnetic field finite element simulation program Ansoft Maxwell. Simulations for single resonators with different design parameters have been performed by removing the meander inductor from the design. Results of these simulations are shown in figure 3.4, where shunt capacitance is plotted against the number of shunt capacitor fingers. In the figure we can recognise the linear dependence of the capacitance.

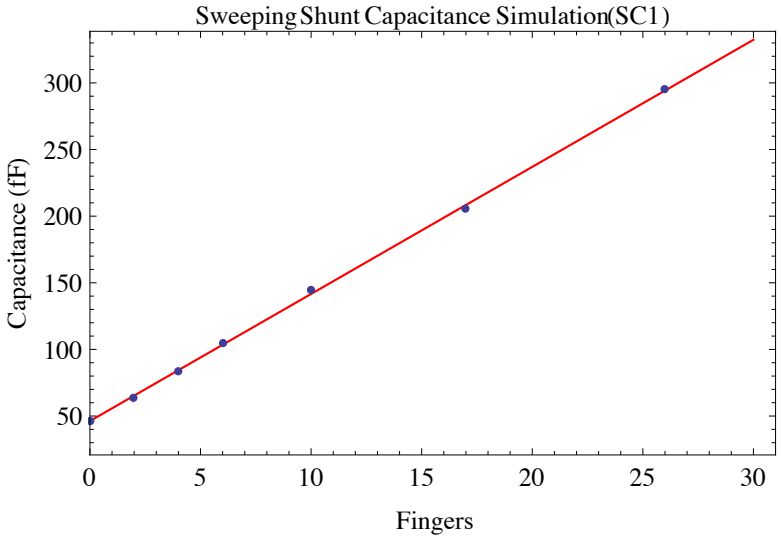

FIGURE 3.4: Plot of the simulated shunt capacitance of SC1 as a function of the number of shunt capacitor fingers. The red curve shows a linear fit.

3.3 Meander inductors

A meander line inductor is a printed inductor with a two-dimensional structure, where the conductor line (superconductor) is meandered back and forth to maximize its total length and with it its inductance [16, 17]. In a similar fashion to interdigital finger capacitors it offers the advantage of not requiring a multilevel process in its fabrication, though it also displays smaller inductance per unit area compared to coil or spiral inductors [16]. To get the maximum inductance for a given area the meander turns have to be close together (3 μm in our case). This will lead to a reduction of the inductance due to negative mutual inductance [17] and it will also increase the parasitic capacitance between turns [16]. However it will still maximize the inductance for a given area.

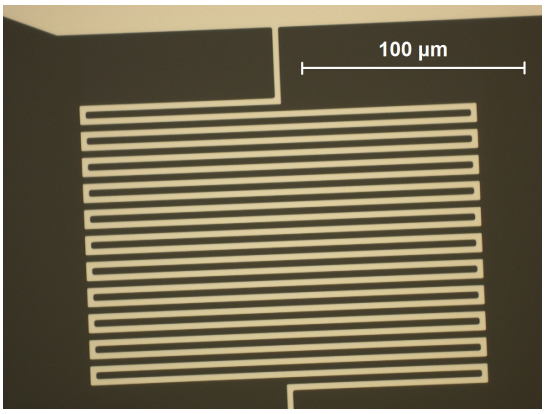

FIGURE 3.5: Detailed picture of a meander inductor with 21 meander turns in one of our resonators.

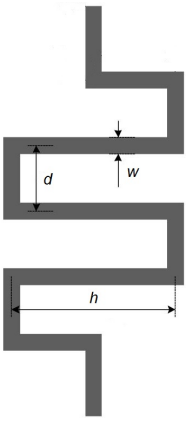

FIGURE 3.6: Design parameters of a meander inductor with three turns [17].

3.3.1 Inductors design parameters

The main parameters necessary to characterize a meander inductor are the width of the meander line, the length and spacing of the turns, the number of turns and the distance between the edges of the inductor. In our resonators we will only change the number of turns with the rest of parameters fixed. Table 3.2 shows the usual values of the main parameters of the inductor.

MEANDER INDUCTOR	
Offset Length	200 μm
Width of the line (w)	3 μm
Length of the turns (h)	180 μm
Gap between turns (d)	3 μm
Standard number of turns	21

TABLE 3.2: Design details of the meander inductors used in our resonators.

3.3.2 Estimation of the inductance

When considering only the inductive contribution of the inductor in the whole resonator, the geometry is simple and general enough to avoid the use of electromagnetic simulations, and therefore we shall be able to characterize our inductors by directly calculating the expected inductance. To do so we will use the method derived by Stojanovic et al. [17] for meander line inductors. By doing so, we obtain results of the dependence on the number of turns, as shown in figure 3.7.

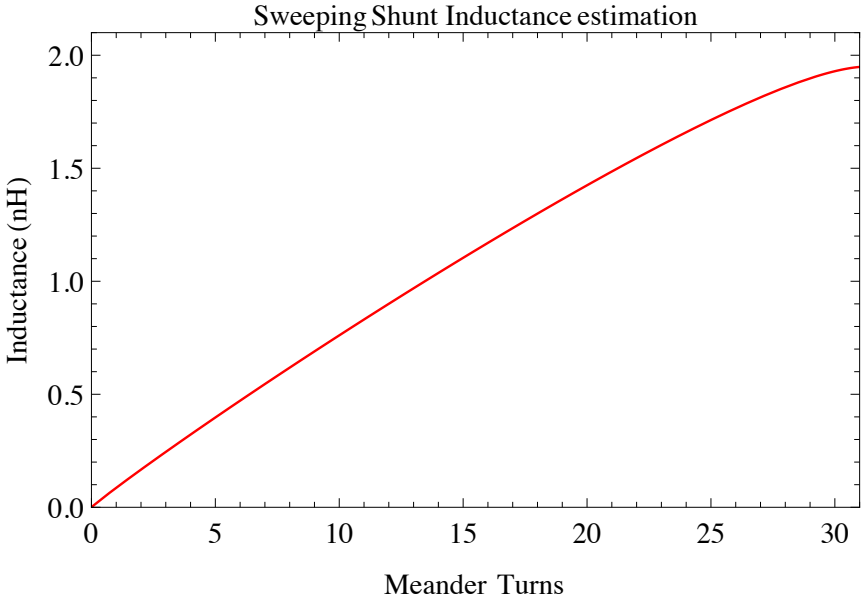

FIGURE 3.7: Plot of the estimated inductance of the meander inductor as a function of the number of meander turns. The inductance for the standard number of turns (21) is of 1.5 nH.

Yet from measurements and other simulations, we have seen that the contribution from the island of the resonator to the total inductance will be relevant, which for most of our samples will have a value close to 0.2 nH.

An important effect which should be taken into account for superconducting inductors is kinetic inductance. In a superconductor, the total inductance will have a contribution from the geometry of the line (geometric inductance) and another due to the change in the kinetic energy of the Cooper pairs subjected to high frequency currents (kinetic inductance). Since the second contribution depends on the density of Cooper pairs in the superconductor, it will also depend on the temperature at which the samples are measured. Within the Ginzburg-Landau theory, for one-dimensional superconductors and for temperatures close to T_c, the dependence of the kinetic inductance on temperature can be expressed as [18]

$$L_K(T) \approx L_K(T=0)\left(\frac{1}{1-T/T_c}\right). \tag{3.1}$$

In our resonators the contribution of the kinetic inductance has been extracted from measurements to be around 3 %, which is shown in appendix B, and can therefore be neglected.

3.4 High-frequency simulation of parasitics

To be able to quantify the parasitics in our resonators, we also performed high-frequency electromagnetic finite element simulation of our structures, by using the

Sonnet software. We analysed each of the lumped-element components individually and together as the whole structure. For each component we obtained the first self-resonant frequency and therefore quantify their parasitic contribution. In table 3.3 the number of fingers for the capacitors and the numbers of turns for the inductor are indicated, together with the first self-resonance frequency obtained from simulation.

	Fingers/Turns	Self-resonant frequency (GHz)
Shunt Capacitor	25	81.3
Shunt Capacitor (2)	50	230.0
Shunt Inductor	21	39.5
Coupling Capacitor	3	490.2

TABLE 3.3: Design parameter and simulated self-resonant frequency of each of the components of our resonators. Self-resonant frequencies were simulated using Sonnet.

Simulating the whole resonator we obtain the resonance frequency and the first self-resonant frequency, which is given in table 3.4.

Sample	Resonant frequency (GHz)	First parasitic frequency (GHz)
M36 IL0 4	6.97	48.95

TABLE 3.4: Results from the simulation of the structure of a whole resonator.

Having the first parasitic frequency of the whole system, we can estimate the ratio between the first self-resonant frequency of each of the elements compared to the typical operating frequency. By using the expected values of inductance and capacitance of each one of the elements and the self-resonant frequency we can extract the approximate parasitic contribution to each of them considering a model of a series or parallel LC circuit. We also show the parasitic renormalization factor as described in eqs. 2.35, 2.34. These results are shown in table 3.5.

	f_s/f_0	Approx. parasitics	Renormalization factor
Shunt Capacitor	11.6	15 pH	1.0075
Shunt Capacitor (2)	32.9	1 pH	1.0009
Shunt Inductor	5.64	11 fF	1.0325
Coupling Capacitor	70.0	8 pH	1.0002

TABLE 3.5: Ratio between the self-resonant and LC resonance frequency for each of the components and estimation of the reactive parasitics. We also show the parasitic renormalization factor, which have been obtained by using equations 2.33 and 2.35.

3.5 Multiple coupled resonators

The main focus in this thesis has been the measurement of arrays of 2 and 3 coupled resonators, even though arrays of 4, 6, 9 and even 15 coupled resonators

have also been fabricated. In figures 3.8 and 3.9 we show samples with 2 and 3 resonators respectively.

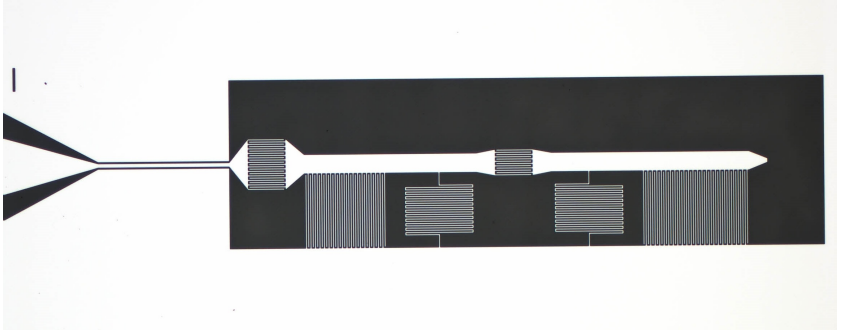

FIGURE 3.8: Picture of a sample with two coupled resonators.

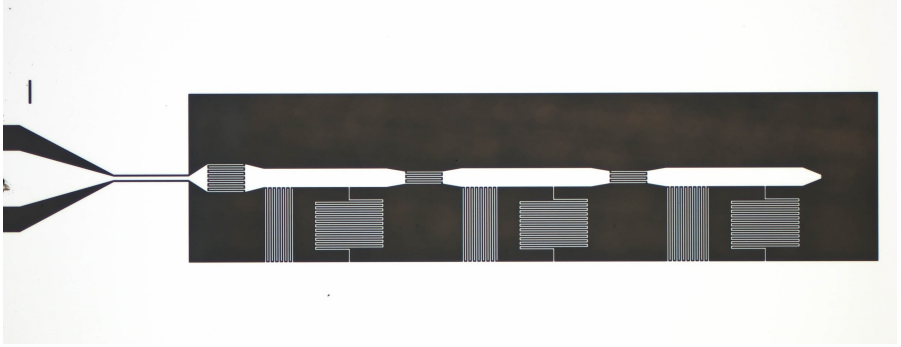

FIGURE 3.9: Picture of a sample with three coupled resonators.

The aim of this particular design for multiple coupled resonators is that each resonator has approximately the same environment. With this design guide the distances between the resonators were kept the same and equal to the distances to the ground planes for resonators at the edges. In the case of the dimer the position of the inductor and the capacitor were exchanged in the right resonators for symmetry reasons. This also helps to obtain an electromagnetic field environment as similar as possible for both resonators, which is especially important when introducing arrays of SQUIDs instead of meander inductors.

3.6 Nonlinear resonators

Single nonlinear resonators and arrays of 2 and 3 nonlinear resonators were also fabricated, by shunting the resonator with an array of SQUIDs instead of the meander inductor. A close picture of the arrays can be seen in figures 3.11 and 3.12, while the dimensions of an individual asymmetric SQUID are indicated in figure 3.10. A summary of the design parameters of an individual SQUID are given in table 3.6.

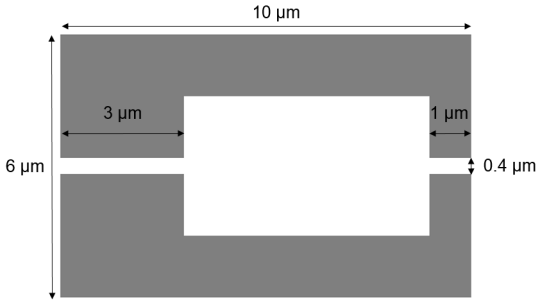

FIGURE 3.10: Asymmetric SQUID with its dimensions.

SQUID parameters	
Oxide thickness	2-3 nm
Left junction overlap	2.4 μm^2
Right junction overlap	0.8 μm^2
Loop area	19.2 μm^2
Asymmetry	1/3

TABLE 3.6: Asymmetric SQUID design parameters.

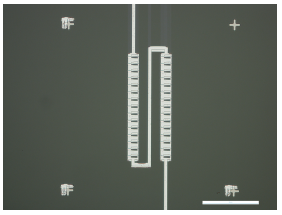

FIGURE 3.11: Picture of an array of 30 aluminum SQUIDs.

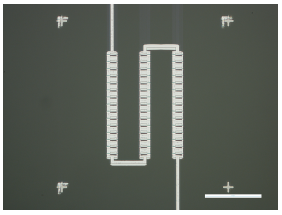

FIGURE 3.12: Picture of an array of 45 aluminum SQUIDs.

In figures 3.13, 3.14 we show one nonlinear resonator and an array of 3 coupled nonlinear resonators. The measurements of these two samples are described in chapter 7.

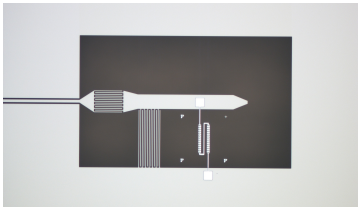

FIGURE 3.13: Picture of a nonlinear resonator.

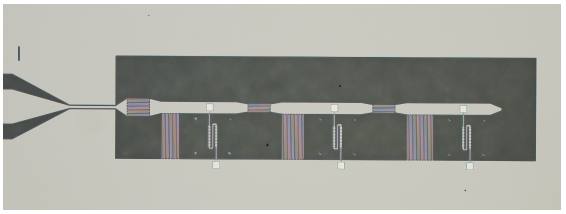

FIGURE 3.14: Picture of an array of three nonlinear resonators.

Chapter 4

Modelling of coupled RLC resonators

The characterization of microwave superconducting resonators requires a proper model (from simulations and measurements of each particular sample) which will correctly describe our system. From the side of electrical circuits, it is desirable to find the equivalent circuit model and the corresponding effective parameters that describe our microwave components. However, a Hamiltonian description of the system will also be required to understand the behaviour of Josephson parametric amplifiers and to precisely engineer the Hamiltonian for multiple-cavity quantum simulations.

In this chapter we construct a basic equivalent-circuit model for a single resonator and show how this can be mapped into a Hamiltonian description through input-output theory. From this model, we show what kind of measurements will allow us to extract the effective inductances and capacitances of the designed lumped-element components of the resonators. We will also extend this model to multiple-resonator systems and discuss how to obtain expressions that can be fitted to the measured data.

4.1 Equivalent circuit model

In chapter 2 we state that at microwave frequencies fully ideal lumped-element components will never be possible to design, mainly due to fringing fields. This limitation would imply that a three-dimensional field analysis by solving Maxwell equations is required to describe our system. Nevertheless, if different parasitic contributions are understood and quantified, a distributed-element circuit could be employed, where infinitesimal lumped elements will be continuously distributed throughout the whole system. The same approach is used to describe a transmission line in chapter 2, however in the case of more complicated structures like interdigital capacitors, meander inductors or the whole resonator, the values of the infinitesimal lumped elements are not necessarily homogeneous, which can

lead to complicated models.

An example of a distributed model is represented in figure 4.1. It will in general have an infinite number of resonances, and solving it will require the application of calculus. Even though this is already a strong simplification compared to the field-analysis approach, one of the motivations for choosing a lumped-element architecture in this thesis has been the simplified description of such components. As discussed in chapters 2 and 3, if the operating frequencies are small enough compared to the self-resonant frequency of the components, an effective lumped-element model will still work for narrow frequency ranges. Since the main interesting regions of the resonators will be around their natural resonant frequencies, the simplification will still hold.

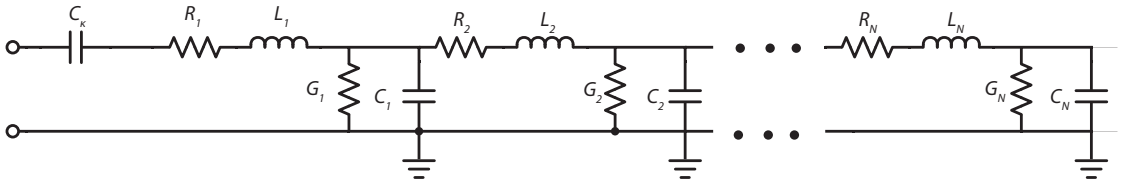

FIGURE 4.1: Example of a distributed-element model for a certain microwave component.

To emphasize the validity of this approach, we will show that the impedance of a short-circuited $\lambda/4$ line close to the resonance is equivalent to the impedance of a parallel RLC circuit. A short-circuited $\lambda/4$ line is a kind of distributed-element resonator which can be modelled as a loaded transmission line with $Z_L = 0$ [15]. The impedance of such a system was already derived in equation 2.20 but assuming a lossless line. The impedance for the same resonator including losses will be

$$Z_{in} = j\, Z_0 \tanh(\alpha + j\beta)\, d = Z_0 \frac{1 - j \tanh \alpha d \cot \beta d}{\tanh \alpha d - j \cot \beta d}, \tag{4.1}$$

where Z_0 is the characteristic impedance of the transmission line, α accounts for the losses of the line, β the complex propagation constant and d the length of the transmission line. The circuit will be resonant at the frequency for which $d = \lambda/4$. If we call the resonant frequency ω_0, we can write

$$\beta d = \frac{\omega d}{v_p} = \frac{(\omega_0 + \Delta\omega)\, d}{v_p} = \frac{\pi}{2} + \frac{\pi\, \Delta\omega}{2\, \omega_0}, \tag{4.2}$$

and then

$$\cot \beta d = \cot\left(\frac{\pi}{2} + \frac{\pi\, \Delta\omega}{2\, \omega_0}\right) \approx \frac{-\pi\, \Delta\omega}{2\, \omega_0}. \tag{4.3}$$

If we also assume small losses yielding $\tan \alpha \approx \alpha$, we can rewrite the impedance as

$$Z_{in} = Z_0\, \frac{1 + j\alpha d\, \pi\, \Delta\omega / 2\, \omega_0}{\alpha d + j\, \pi\, \Delta\omega / 2\, \omega_0} \approx \frac{Z_0}{\alpha d + j\, \pi\, \Delta\omega / 2\, \omega_0}. \tag{4.4}$$

Now let us write the impedance of a parallel RLC circuit:

$$Z_{RLC} = \left(\frac{1}{R} + j\omega C + \frac{1}{j\omega L} \right)^{-1}. \tag{4.5}$$

If we substitute with the expression $\omega = \omega_{0,RLC} + \Delta\omega$, where $\omega_{0,RLC} = \frac{1}{\sqrt{LC}}$ is the RLC resonant frequency, and consider the case $\Delta\omega \approx 0$, the impedance can be rewritten as

$$Z_{RLC} \approx \frac{1}{1/R + 2j\Delta\omega\, C}, \tag{4.6}$$

which allows us to see that it has the same form as equation 4.4. Thus we have seen that a distributed-element resonator near one of its resonances can be equivalent to an RLC circuit. It is important to note that aside from assuming small losses we did not assume the system to be in any lumped-element approximation, and the length of the resonator can have an arbitrary value. Based on the previous derivations and this example, we will proceed to describe our lumped-element resonator as a parallel RLC circuit.

4.2 Unloaded RLC parallel circuit

The equivalent circuit model used to describe our resonators is a parallel RLC circuit with a series coupling capacitor. This model takes into account all the designed lumped elements (shunt inductor, capacitor and coupling capacitor) and also the losses of the resonator, mainly due to the electric fields in the dielectric material. To understand better the properties of the circuit, we will start by considering only the RLC circuit without any external coupling, as show in figure 4.2. For completeness we will solve the circuit in two different ways: one by calculating the impedance [15] and the other by describing the system as an harmonic oscillator and writing down the equation of motion [19]. Using both methods will help us to better understand the meaning of the resonance frequency and the quality factor.

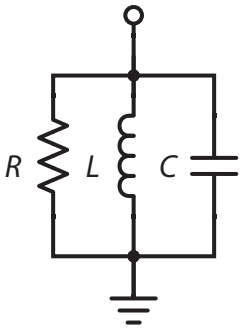

FIGURE 4.2: Circuit model of an unloaded RLC resonator.

4.2.1 Impedance method

In the RLC circuit model the resistor of the circuit will only dissipate energy, while the capacitor and the inductor will release and absorb energy in a periodic way. Because of this, the circuit will have a complex delivered power

$$P_{in} = V\, I^* = |I|^2\, Z_{RLC} = \frac{|V|^2}{Z_{RLC}} \tag{4.7}$$

where V and I are the root-mean-square of voltage and current. In particular the power dissipated by the resistor will be

$$P_R = \frac{|V|^2}{R}, \tag{4.8}$$

and by using the expressions of the energy stored in a capacitor and the energy stored in an inductor we will be able to write the average stored energy in each of these components as

$$U_C = \frac{1}{2}\, C\, |V|^2, \tag{4.9}$$

$$U_L = \frac{1}{2}\, L\, |I_L|^2. \tag{4.10}$$

By combining the previous expressions we can write the incident power as

$$P_{in} = P_R + 2\, j\omega\, (U_L - U_C), \tag{4.11}$$

and allowing to rewrite the impedance of the system as

$$Z_{RLC} = \frac{P_{in}}{|I|^2} = \frac{P_R + 2\, j\omega\, (U_L - U_C)}{|I|^2}. \tag{4.12}$$

We see that the imaginary part of the impedance will vanish when the average stored energies are identical in the capacitor as in the inductor, which will happen at the resonant frequency

$$\omega_0 = \frac{1}{\sqrt{LC}}. \tag{4.13}$$

Now we proceed to find the quality factor of the resonator. The quality factor is defined as

$$Q = 2\pi\, \frac{\text{Energy Stored}}{\text{Energy dissipated per cycle}} = \omega_0\, \frac{\text{Energy Stored}}{\text{Power Loss}}, \tag{4.14}$$

and it will in general describe the frequency selectivity of the circuit. For our circuit it will yield

$$Q = \omega_0\, \frac{U_L + U_C}{P_R} = \omega_0\, R\, C, \tag{4.15}$$

by using that U_L and U_C are equal at resonance.

4.2.2 Equation of motion method

Instead of calculating the impedance, we are going to write down the equation of motion of the circuit, starting by applying Kirchhoff's current law to the circuit in figure 4.2:

$$\sum_k I_k = I_L + I_C + I_R = 0. \tag{4.16}$$

And if we derive once with respect to time we get

$$\sum_k \dot{I}_k = \dot{I}_L + \dot{I}_C + \dot{I}_R = 0. \tag{4.17}$$

We can write each one of the terms as

$$\dot{I}_R = \frac{d}{dt}\left(\frac{V}{R}\right) = \frac{\dot{V}}{R}, \tag{4.18}$$

$$\dot{I}_L = \frac{V}{L}, \tag{4.19}$$

$$\dot{I}_C = \ddot{Q}_C = \frac{d^2}{dt^2}(C\,V) = C\,\ddot{V}, \tag{4.20}$$

allowing us to write

$$C\,\ddot{V} + \frac{\dot{V}}{R} + \frac{V}{L} = 0, \tag{4.21}$$

which if we divide by C will yield the equation of a damped harmonic oscillator:

$$\ddot{V} + \frac{\dot{V}}{R\,C} + \frac{V}{L\,C} = \ddot{V} + \gamma\,\dot{V} + \omega_0^2\,V = 0. \tag{4.22}$$

In this equation $\gamma = 1/RC$ is the loss rate and $\omega_0 = 1/\sqrt{LC}$. Having these parameters we can find the quality factor based on the previous definition:

$$Q = \omega_0 \frac{\text{Energy Stored}}{\text{Power Loss}} = \omega_0 \frac{1}{\gamma} = \omega_0\,R\,C. \tag{4.23}$$

4.3 Loaded RLC parallel circuit

We have obtained the resonance frequency of the unloaded resonator and the unloaded quality factor, also known as internal quality factor or Q_{int}. In those derivations we ignored any effects caused by the external circuitry. However, to be able to spectroscopically measure a resonator we will always require a coupled system. In our case we couple our resonators with an external coupling capacitor, which allows us to tune the coupling coefficient of our system. The rest of cables and the VNA are assumed to have a characteristic impedance of $50\,\Omega$, and therefore we can write the exact reflection coefficient at the input of the resonator as

$$\Gamma(\omega) = \frac{Z_T(\omega) - 50\,\Omega}{Z_T(\omega) + 50\,\Omega}, \tag{4.24}$$

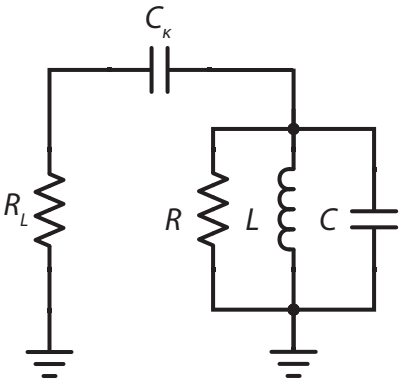

FIGURE 4.3: Circuit model of a loaded RLC resonator.

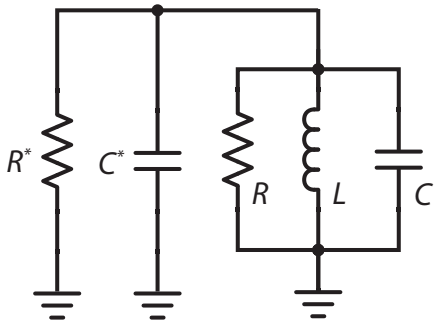

FIGURE 4.4: Norton equivalent circuit of a loaded RLC resonator.

where $Z_T = j\omega C_\kappa + Z_{RLC}$. It can be shown that such a system contains two resonances, corresponding to the unloaded and the loaded frequencies. Even though for most cases only the loaded frequency will matter, it will become difficult to identify the position of the resonance by using the previous expression for the reflection coefficient. To solve this, we first write the circuit of the whole system, as shown in figure 4.3, where we model the cables and the VNA with a $R_L = 50\,\Omega$ resistor. To understand in a simpler way the effect of the loading, we will start by neglecting the internal losses, which is equivalent to considering an infinite internal parallel resistor. The circuit now involves components in parallel and components in series, but we can write the Norton equivalent circuit of the external branch as a resistor and a capacitor in parallel, as seen in figure 4.4. The equivalent components can be expressed as

$$C^*(\omega) = \frac{C_\kappa}{1 + (\omega\, C_\kappa\, R_L)^2}, \tag{4.25}$$

$$R^*(\omega) = \frac{1 + (\omega C_\kappa R_L)^2}{(\omega C_\kappa R_L)^2}. \tag{4.26}$$

Since the two capacitors in parallel can be added together in a single component with capacitance $C + C^*$, we end up with a parallel RLC circuit as in the previous section, for which we already found the solution. If we now assume that $C^*(\omega)$ and $R^*(\omega)$ do not change appreciably close to resonance, we can take their value at the resonant frequency, so that $C^* = C^*(\tilde{\omega}_0)$ and $R^* = R^*(\tilde{\omega}_0)$. This allows us to write the resonant frequency of the system and the quality factor as

$$\tilde{\omega}_0 = \frac{1}{\sqrt{L\tilde{C}}} = \frac{1}{\sqrt{L\,(C + C^*)}}, \tag{4.27}$$

$$Q = \tilde{\omega}_0\, \tilde{R}\, \tilde{C} = \tilde{\omega}_0\, R^*\, (C + C^*). \tag{4.28}$$

Where Q will be the external quality factor, since it does not take into account any internal losses. We can also write down the expression for the external coupling

rate κ, the rate at which energy is lost through the transmission line, as

$$\kappa = \frac{1}{\tilde{R}\tilde{C}} = \frac{1}{R^*(C + C^*)}. \tag{4.29}$$

If we solve self-consistently the expression of $\tilde{\omega}_0$ we will get the loaded resonant frequency $\tilde{\omega}_0$. It is important to note that we have reduced the original system with two resonances to a system with a single resonance. This approximation has been done by assuming that the Norton-equivalent elements are frequency independent. Since the exact expression includes a dependence on the frequency, solving the circuit with any of the two previous methods will require to take the dependence into account. However this approximation will still hold for most weakly coupled cases.

If we take into account the internal losses of the resonator, the resonant frequency will remain unaffected, but the quality factor, the loaded Q for this case, will change since the effective resistor will now be $\tilde{R} = (1/R + 1/R^*)$. We can write it as

$$Q_L = \tilde{\omega}_0 \, \tilde{R} \, \tilde{C} = \tilde{\omega}_0 \, \frac{C + C^*}{1/R + 1/R^*}, \tag{4.30}$$

and for $C^* \ll C$ it can be written as

$$\frac{1}{Q_L} = \frac{1}{Q_{int}} + \frac{1}{Q_{ext}} = \frac{\gamma}{\tilde{\omega}_0} + \frac{\kappa}{\tilde{\omega}_0}. \tag{4.31}$$

4.4 Hamiltonian description for multiple coupled cavities

In this section we will derive a Hamiltonian of the system where several resonators are capacitively coupled. Such a description will be used together with input-output theory to derive the expression of the reflection coefficient as a function of the Hamiltonian parameters, which will be used to fit the measured data for two and more coupled resonators. It will also be important to use it as a bridge between the circuit and the Hamiltonian models, since it offers a simpler description for larger systems and will allow to model nonlinear and quantum effects, which is ultimately required to design arbitrary Hamiltonian parameters.

In a similar fashion to the input-output theory derivation for one single resonator, the Hamiltonian will not take into account the interaction with the external world, and neither the internal losses. These will be considered later when applying input-output theory. To start we will consider the Lagrangian of an electric circuit with N LC parallel oscillators coupled to each other capacitively, with the mode flux ($V_i = \dot{\phi}_i$) as coordinate [20]. It can be written as

$$\mathcal{L} = \sum_{i=1}^{N} \frac{1}{2} C_i \, \dot{\phi}_i^2 + \sum_{i=1}^{N} \frac{1}{2} C_{Ji} \, (\dot{\phi}_i - \dot{\phi}_{i+1})^2 - \sum_{i=1}^{N} \frac{1}{2L_i} \, \phi_i^2, \tag{4.32}$$

where the first contribution corresponds to the shunt capacitors, the second to the coupling capacitors and the third to the shunt inductances. We can also rewrite

the Lagrangian as

$$\mathcal{L} = \frac{1}{2}\,\dot{\Phi}^T\,C\,\dot{\Phi} - \frac{1}{2}\,\Phi^T\,L^{-1}\,\Phi, \tag{4.33}$$

where $\Phi = (\phi_1, \phi_2, \phi_3, ...)$ is a vector, C a tridiagonal capacitance matrix ($C_{i\,i} = C_i$, $C_{i\,i+1} = C_{i+1\,i} = C_{Ji}$) and L^{-1} the inverse of a diagonal inductance matrix ($L^{-1}_{i\,i} = 1/L_i$). We can now extract the generalized momentum, the charge, as

$$q_i = \frac{\partial \mathcal{L}}{\partial \dot{\Phi}_i} = C_{ij}\dot{\Phi}^j, \tag{4.34}$$

which allows us to write the Hamiltonian as

$$\mathcal{H} = \frac{1}{2}\,Q^T\,C^{-1}\,Q + \frac{1}{2}\,\Phi^T\,L^{-1}\,\Phi \tag{4.35}$$

where $Q = (q_1,\, q_2, ...)$ is the charge vector. We proceed now to upgrade the two canonical conjugate variables to operators described by the canonical commutation relation

$$\left[\hat{q}_i,\, \hat{\phi}_j\right] = -j\hbar\,\delta_{ij}. \tag{4.36}$$

Now we can define second-quantization operators to reach the expression

$$\mathcal{H} = \sum_{i=1}^{N} \hbar\,\omega_i \left(\hat{a}_i^\dagger \hat{a}_i + \frac{1}{2}\right) + \sum_{j>i} \hbar\,J_{ij}\left(\hat{a}_i^\dagger \hat{a}_j + \hat{a}_j^\dagger \hat{a}_i\right), \tag{4.37}$$

where

$$\omega_i = \sqrt{C_{ii}^{-1}\,L_{ii}^{-1}}, \tag{4.38}$$

$$J_{ij} = \frac{1}{2}\frac{C_{ij}^{-1}}{\sqrt{C_{ii}^{-1}\,C_{jj}^{-1}}}\sqrt{\omega_i\,\omega_j}. \tag{4.39}$$

Having the expression of the Hamiltonian we can now apply the input-output relations to obtain the different scattering parameters.

4.5 Input-output theory for a single resonator

In the previous section we found expressions which relate the values of the electrical circuit components to the resonant frequency and the quality factor. To be able to extract any of these parameters from the measurement of our resonators, it is necessary to fit the scattering parameters of the system, since this is the data that we will obtain by measuring with a VNA. For most of our geometries, the complex reflection coefficient will be the parameter to fit. We can directly use the expression of equation 4.24, which depends on R, L, C, C_κ, but in practice these parameters will be underdetermined and therefore several solutions will be compatible with the same reflection fit. A better solution is to fit a reflection coefficient which depends on the resonance frequency and the damping rates. To obtain these we will use input-output theory, which describes the viewpoint of an external observer that sends signals to the system and measures the reflected signals to extract

information from it. We will start by considering the Hamiltonian of a resonator in the linear regime, which is simply:

$$\mathcal{H} = \hbar\,\omega_0 \left(\hat{a}^\dagger \hat{a} + \frac{1}{2}\right), \tag{4.40}$$

where ω_0 is the resonant frequency of the resonator, and $\hat{a}$, $\hat{a}^\dagger$ correspond to the annihilation and creation operators of the field in the resonator. The Heisenberg equation can be derived for the model indicated in figure 4.5, obtaining the expression

$$\dot{\hat{a}}(t) = -\frac{j}{\hbar}\,[\hat{a}(t), \mathcal{H}] - \frac{\kappa+\gamma}{2}\,\hat{a}(t) + \sqrt{\kappa}\,\hat{a}_{\text{in}}(t), \tag{4.41}$$

which rewritten in Fourier space takes the form

$$-\,j\omega\,\hat{a}(\omega) = -j\omega_0\,\hat{a}(\omega) - \frac{\kappa+\gamma}{2}\,\hat{a}(\omega) + \sqrt{\kappa}\,\hat{a}_{\text{in}}(\omega). \tag{4.42}$$

And together with the input-output relation

$$\hat{a}_{\text{in}}(\omega) + \hat{a}_{\text{out}}(\omega) = \sqrt{\kappa}\,\hat{a}(\omega), \tag{4.43}$$

we can derive the expression

$$\Gamma_{\text{in-out}} = \frac{\hat{a}_{\text{out}}(\omega)}{\hat{a}_{\text{in}}(\omega)} = \frac{\sqrt{\kappa}\,\hat{a} - \hat{a}_{\text{in}}}{\hat{a}_{\text{in}}} = \frac{\kappa\,\hat{a}}{\left(-j(\omega-\omega_0) + \frac{\kappa+\gamma}{2}\right)\hat{a}} - 1$$

$$= \frac{\kappa}{\left(-j(\omega-\omega_0) + \frac{\kappa+\gamma}{2}\right)} - 1. \tag{4.44}$$

Here the parameters to be obtained from the fit are the resonance frequency ω_0, the coupling rate κ and the loss rate γ.

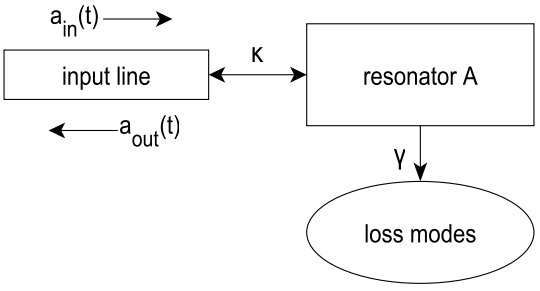

FIGURE 4.5: Schematic of input-output theory applied to a single-ended single resonator.

The reflection coefficient obtained from the impedance is equivalent to the one derived from input-output theory when the approximations of weak coupling considered in the previous section are applied. The expression 4.24 can be rewritten

as

$$\Gamma(\omega) = \frac{R_L + jX_\kappa}{R_L - jX_\kappa}\left(\frac{2j\,\tilde{\kappa}(\omega)}{\frac{\tilde{\omega}_0^2-\omega^2}{\omega} + j\,(\tilde{\kappa}(\omega)+\tilde{\gamma}(\omega))} - 1\right), \tag{4.45}$$

where $X_\kappa = 1/\omega\, C_\kappa$ is the reactance of the coupling capacitor and $\tilde{\kappa} = 1/(\tilde{C}\, R^*)$, $\tilde{\gamma} = 1/(\tilde{C}\, R)$ are effective damping rates. The term outside the parenthesis will have modulus 1 and therefore can be expressed as a frequency-dependent phase shift $\theta(\omega)$. If we consider again only a region close to the resonant frequency, we can approximate the phase shift $\theta(\omega) \approx \theta(\omega_0)$ as constant, and similarly $\tilde{\kappa}(\omega) \approx \tilde{\kappa}(\omega_0) = \tilde{\kappa}$, $\tilde{\gamma}(\omega) \approx \tilde{\gamma}(\omega_0) = \tilde{\gamma}$. We can also approximate $\tilde{\omega}_0^2 - \omega^2 = (\tilde{\omega}_0 - \omega)(\tilde{\omega}_0 + \omega) \approx (\tilde{\omega}_0 - \omega)2\omega$, yielding:

$$\Gamma(\omega) = e^{j\theta}\left(\frac{\tilde{\kappa}}{-j(\omega-\tilde{\omega}_0) + \frac{\tilde{\kappa}+\tilde{\gamma}}{2}} - 1\right). \tag{4.46}$$

In this section we only considered the case of a single resonator, however we note that input-output theory can be applied to any Hamiltonian, which allows to obtain the reflection coefficient for arrays of coupled resonators by using the Hamiltonian derivation from the previous section. An example for two coupled resonators can be found in [21].

4.6 Extraction of LC parameters

In this chapter we established a connection between the electric circuit parameters C, L, C_κ, R (internal resistance) and the resonators parameters ω_0, κ and γ. Naively one could think that the previous derivations allow to extract the circuit parameters by measuring the resonators parameters. However there are two limitations to such an approach. The first one is the requirement of an accurate calibration of the measurement device to precisely measure a resonator. This is particularly complicated for superconducting resonators, since a proper calibration would need to be done at cryogenic temperatures with calibration standards suitable for those temperatures. The second limitation is that even if the resonance frequency and the coupling and loss rates were precisely measured they would not be enough to determine the circuit parameters. An additional parameter, the phase shift ϕ far from resonance, would be needed, but even with an accurate calibration this phase will depend strongly on the external environment (characteristic impedance of the measurement lines), requiring also a precise study of the measuring setup to extract the parameters.

We conclude that the extraction of the parameters with measurement data from individual samples is in practice not going to be possible. In this section we will describe a method to extract all the relevant parameters which will require the measurement of two identical resonators but with extremely different coupling capacitors. First let us consider an extremely undercoupled resonator ($C_\kappa \approx 0$,

$\kappa \ll \gamma$, $Q_L \approx Q_{int}$), whose resonant frequency will be

$$\omega_0 \approx \frac{1}{\sqrt{L\,C}}, \tag{4.47}$$

since there will be no "loaded" contribution (for the moment we will not discuss the internal quality factor, since the internal losses cannot be easily modified by the design). Now let us consider a sample with the same shunt capacitor and shunt inductor but extremely overcoupled ($\kappa \gg \gamma$, $Q_L \approx Q_{ext}$), whose frequency will be given by

$$\tilde{\omega}_0 = \frac{1}{\sqrt{L\,\tilde{C}}} = \frac{1}{\sqrt{L\,(C+C^*)}} = \frac{1}{\sqrt{L\,(C+\frac{C_\kappa}{1+(\tilde{\omega}_0\,C_\kappa\,R_L)^2})}}, \tag{4.48}$$

and the external quality factor by

$$\begin{aligned} Q_{ext} &= \tilde{\omega}_0\,\tilde{R}\,\tilde{C} = \tilde{\omega}_0\,R^*(C+C^*) \\ &= \tilde{\omega}_0\,\frac{1+(\tilde{\omega}_0\,C_\kappa\,R_L)^2}{(\tilde{\omega}_0\,C_\kappa\,R_L)^2}\left(C+\frac{C_\kappa}{1+(\tilde{\omega}_0\,C_\kappa\,R_L)^2}\right). \end{aligned} \tag{4.49}$$

By measuring the two different samples we will obtain ω_0, $\tilde{\omega}_0$, Q_{ext}. By using their corresponding expressions, it can be shown that we can write the coupling capacitance as a function of the measured parameters:

$$C_\kappa = \frac{1}{Q_{ext}\,\tilde{\omega}_0\,R_L}\left(1-\frac{1}{1-\left(\frac{\omega_0}{\tilde{\omega}_0}\right)^2}\right), \tag{4.50}$$

from which we can now find the rest of relevant parameters:

$$C = \frac{1}{\left(\frac{\omega_0}{\tilde{\omega}_0}\right)^2-1}\frac{1}{1+(\tilde{\omega}_0\,C_\kappa\,R_L)^2}, \tag{4.51}$$

$$L = \frac{1}{\omega_0^2\,C}. \tag{4.52}$$

By also measuring Q_{int} of the undercoupled resonator, it would also be possible to obtain the value of R, as $R = Q_{int}/(\omega_0\,C)$.

We note that the above procuedure assumes a fixed and well-defined value of the characteristic impedance of the transmission line (R_L). However the values of C and L can be shown to be independent of the value of R_L.

Chapter 5

Theory of Josephson parametric amplifiers

In the field of quantum information processing and quantum optics the ability of measuring electromagnetic signals at the single-photon level is an essential requirement. In the optical frequency range, photon counters exist, but for microwave wavelengths there are no available single-photon detectors. Instead, quantum-limited amplifiers have to be used previous to the detection of single-photon microwave signals [9, 13, 14]. The amount of noise added by these devices to the amplified signal is only limited by vacuum fluctuations [22].

Among the different devices developed for quantum-limited amplification in the range of microwave frequency, parametric amplifiers (paramps) remain the most successful, and in recent years a great variety of paramps based on the Josephson effect have been built [9, 13, 14], allowing to characterize the quantum properties of microwave radiation in the context of circuit QED. In this section we will present the main properties and physical description of such systems, and focus in particular in paramps based on lumped-element nonlinear resonators and the advantages they might offer.

5.1 Parametric oscillation and amplification

A parametric oscillator is a harmonic oscillator which is driven by the variation of one of the system parameters at a different frequency than the resonant one. The most usually given example to illustrate this phenomenon is a child on a swing pumping the amplitude of the swing oscillation by moving forward and backward its legs. By doing so, the child will change the momentum of inertia of the system and therefore also its resonant frequency and the damping (parameters). By moving the legs at twice the natural frequency of the swing, the child is able to drive the swing oscillation, similar as described in [23]. Such a system would be described by the equation of a damped harmonic oscillator with time-dependent parameters:

$$\ddot{\theta} + \beta(t)\,\dot{\theta} + \omega^2(t)\,\theta = 0. \tag{5.1}$$

In contrast to the situation where a harmonic oscillator is directly driven (an adult pushing periodically the swing), for parametric driving the oscillation amplitude will remain zero if the system has no initial amplitude. However, if the oscillator is driven at its natural resonant frequency to a particular amplitude, the parametric oscillation will enhance this amplitude. This phenomenon is known as parametric excitation or parametric pumping, and is the basic idea behind how parametric amplifiers work [24].

In the field of quantum optics, parametric processes are usually associated to the mixing of different frequency components of light, which is due to a nonlinear refractive medium. In this context, a coherent pump field modulates the refractive index of the medium (parameter), which is dependent on the applied electric field, and effectively drives or stimulates the amplitude of fields at different frequencies. The frequency conversion can be caused by either a three-wave or a four-wave mixing process [24, 25]. In the first case, the refractive index depends linearly on the applied electric field ($\chi^{(2)}$ non-linearity, Pockels effect), and each pump photon is converted into a pair of signal and idler photons, their frequencies obeying the relation $\omega_P = \omega_S + \omega_I$. In the case of four-wave mixing, the refractive index depends linearly on the intensity of the electric field ($\chi^{(3)}$ non-linearity, Kerr effect), and in the process two pump photons will be converted into a pair of signal and idler photons with their frequencies obeying $\omega_P + \omega_P = \omega_S + \omega_I$. Such kind of processes are behind the phenomenon of spontaneous parametric down-conversion, where a laser beam incident on a non-linear crystal is used to generate entangled signal-idler pairs of photons [24].

When discussing electrical circuits, the oscillating parameter is usually the effective impedance of the system [9]. This can be done by varying the capacitance or inductance of the system over time. Experiments exploiting these ideas have been performed since the beginning of the 20$^{\text{th}}$ century, and parametric amplifiers were already used for the first time around 1913 for radio telephony in Europe [26]. These first paramps used variable inductances, and although other alternatives have been used over the years (varactor diodes, klystron tubes), Josephson parametric amplifiers are still based in inductance modification.

5.2 Theory of SQUID arrays

5.2.1 The Josephson Junction

A Josephson junction is a device consisting of two superconducting electrodes connected with a thin insulating layer. From BCS theory, we know that the electrons in a superconductor condensate to Cooper pairs, which due to their bosonic character can be described by a single wavefunction, allowing the superconductor to be described by a macroscopic phase and the local Cooper pair density. Brian Josephson theoretically showed in 1962 that if the insulating layer is thin enough the wavefunctions of each of the electrodes will overlap, which will allow Cooper

pairs to tunnel through the insulating layer as a dissipationless supercurrent [27]. This is known as the Josephson effect and it is described by the first and second Josephson relations:

$$I_J(t) = I_0 \sin \delta(t), \tag{5.2}$$

$$V = \frac{\Phi_0}{2\pi} \dot{\delta}, \tag{5.3}$$

where I_0 is the critical current of the junction, δ the gauge-invariant phase difference across the junction and Φ_0 the superconducting flux quantum. The first equation indicates that there will be a superconducting current across the junction proportional to the sine of the phase difference between the superconductors, without any external electromagnetic field. This is known as the dc Josephson effect [28]. If we now take the second Josephson relation and consider a fixed voltage between the two sides of the junction, we can solve the two relations yielding:

$$I(t) = I_0 \sin\left(\frac{\Phi_0}{2\pi} V t + \phi_0\right), \tag{5.4}$$

which indicates that the phase will vary linearly with time and the supercurrent will oscillate at a frequency $\frac{\Phi_0}{2\pi} V$, phenomenon known as the ac Josephson effect.

Using the two Josephson relations we can get the relation between current and voltage of the junction as

$$\dot{I} = I_0 \frac{2\pi}{\Phi_0} V \cos \delta, \tag{5.5}$$

and since in this expression there is a proportionality between the time-derivative of the current and the voltage difference across the junction, we can view our junction as an inductor with a Josephson inductance of

$$L_J = \frac{\Phi_0}{2\pi I_0 \cos \delta}. \tag{5.6}$$

Since the inductance depends on the cosine of the phase difference, which is related to the current, it is clear that it is a nonlinear inductance [29]. We can derive the energy associated to the Josephson inductance as

$$E_J = \int V I \, dt = \frac{\Phi_0 I_c}{2\pi} (1 - \cos \delta) = E_{J0} (1 - \cos \delta), \tag{5.7}$$

where E_{J0} is the intrinsic Josephson energy of the junction. If we consider the energy due to the charges at each side of the junction and obtain the corresponding capacitance, we can derive the energy of the Josephson capacitance as

$$E_C = \frac{(2\,e)^2}{2\,C} N^2 = E_{C0}\, N^2, \tag{5.8}$$

where E_{C0} is the charging energy of the junction and N the number of Cooper pairs. These two energies will characterize the Josephson Junction and it will be necessary to engineer their values for most of their applications.

5.2.2 Symmetric and asymmetric SQUIDs

A SQUID (acronym for Superconducting Quantum Interference Device) is a superconducting loop interrupted by one or more Josephson junctions. Its principal use is to very sensitively detect magnetic fields [28]. Here in the context of circuit QED we will only discuss the known as dc SQUID, which is basically constituted by two Josephson junctions in parallel [30]. The total current going across the two Josephson junctions is

$$I_{SQUID} = I_1 + I_2 = I_{0,1} \sin \delta_1 + I_{0,2} \sin \delta_2. \tag{5.9}$$

Since the change of the phase along the closed contour has to be a multiple of 2π we can write

$$\oint_C \nabla\theta \, dl = 2\pi n, \tag{5.10}$$

where θ is the macroscopic phase of the system. We can write the contour integral as a sum of the contribution from the junctions and the one from the superconductors:

$$\oint_C \nabla\theta \, dl = ((\theta_b - \theta_a) + (\theta_d - \theta_c)) + \left(\int_d^a \nabla\theta \, dl + \int_b^c \nabla\theta \, dl \right). \tag{5.11}$$

We can write the phase difference across the Josephson junctions as a function of the gauge-invariant phase difference and the vector potential $\mathbf{A}$:

$$(\theta_b - \theta_a) = -\delta_1 - \frac{2\pi}{\Phi_0} \int_a^b \mathbf{A} \cdot dl, \tag{5.12}$$

$$(\theta_d - \theta_c) = \delta_2 - \frac{2\pi}{\Phi_0} \int_b^d \mathbf{A} \cdot dl, \tag{5.13}$$

and the integrals across the superconductors as

$$\int_d^a \nabla\theta \, dl = \int_d^a (-\Lambda \mathbf{J} - \frac{2\pi}{\Phi_0} \mathbf{A}) \, dl, \tag{5.14}$$

$$\int_b^c \nabla\theta \, dl = \int_b^c (-\Lambda \mathbf{J} - \frac{2\pi}{\Phi_0} \mathbf{A}) \, dl, \tag{5.15}$$

where Λ is the London penetration depth and $\mathbf{J}$ is the current density. If the thickness of the superconductors is much larger than the London penetration depth, the integral can always be performed through a path in which $\mathbf{J} = 0$, allowing us to write the whole contour integral as

$$\oint_C \nabla\theta \, dl = \delta_2 - \delta_1 - \frac{2\pi}{\Phi_0} \oint_C \mathbf{A} \, dl = 2\pi n, \tag{5.16}$$

and since the total magnetic flux is $\Phi = \oint_C \mathbf{A} \, dl$, we reach the expression

$$\delta_2 - \delta_1 = 2\pi \left(n + \frac{\Phi}{\Phi_0} \right). \tag{5.17}$$

This allows us to rewrite the critical current from expression 5.9 as

$$I_0 = \sqrt{(I_{0,1} - I_{0,2})^2 + 4\, I_{0,1}\, I_{0,2} \cos^2\left(\pi \frac{\Phi_{ext}}{\Phi_0}\right)}, \tag{5.18}$$

where we have assumed that $\Phi \approx \Phi_{ext}$, since the field generated by the loop will in general be extremely smaller than the flux quantum [31]. This last equation shows that the SQUID is effectively a Josephson junction with a critical current which can be tuned with an external magnetic field. Now let us write down the expression for the SQUID critical current when both Josephson junctions have the same critical current:

$$I_0 = 2I_0 \left|\cos\left(\pi \frac{\Phi_{ext}}{\Phi_0}\right)\right|. \tag{5.19}$$

If we compare the last expression with equation 5.18, and analyse the tunability for arbitrary asymmetric values of the two junctions, it can be seen that an asymmetric SQUID will always have a narrower range of tunability, but it will also have smaller sensitivity to magnetic flux noise, specially on the extremal points. The tunability of the Josephson inductance will have a similar behaviour depending on the asymmetry of the SQUID, and if a SQUID is used as a non-linear inductor in an LC resonator, the range of tunability of its resonant frequency and its resilience to magnetic flux noise can also be modified by choosing desired values of the asymmetry. In the design of Josephson paramps, we will in most cases sacrifice the range of tunability in order to bound the tunable Josephson energies, which will make the paramp more insensitive to inhomogeneities when dealing with arrays of SQUIDs [9].

5.3 Josephson parametric amplification

In the previous sections we showed that a dc SQUID can be used as a non-linear tunable inductor. Because of such properties, by adding the SQUID with a shunt capacitor we can use it as a parametric amplifier [9], where the oscillating parameter will be the effective inductance of the SQUID. There will in general be two methods to do so. The first will use the non-linearity of the SQUID inductance with respect to the applied current with currents much smaller than the critical current

$$\begin{aligned} L_J &= \frac{\Phi_0}{2\pi I_0 \cos\delta} = \frac{\Phi_0}{2\pi I_0} \frac{1}{\cos(\arcsin(I/I_0))} \\ &\approx \frac{\Phi_0}{2\pi I_0} \frac{1}{1 - \frac{1}{2}(I/I_0)^2} \approx \frac{\Phi_0}{2\pi I_0}\left(1 + \frac{1}{2}\left(\frac{I}{I_0}\right)^2\right). \end{aligned} \tag{5.20}$$

This dependence is equivalent to a $\chi^{(3)}$ non-linearity, and can therefore be used for 4-wave mixing. The second method will use the tunability of the critical current in a SQUID [32], which for the symmetric case will depend on $|\cos\frac{\Phi}{\Phi_0}|$. If we consider only the external flux contribution, we can see that for values of Φ much smaller than the flux quantum, the critical current will depend quadratically on

the flux, yielding a 4-wave mixing process. However, an external dc flux can be applied such that the dependence of the critical current on small flux variations will be linear. If we set $\frac{\Phi_{dc}}{\Phi_0} = \frac{1}{4}$, we can write

$$I_{0,\,SQUID} = 2\,I_0 \left|\cos\left(\pi\,\frac{\Phi_{dc}+\Phi_{ac}}{\Phi_0}\right)\right| \approx 2\,I_0\left(\frac{1}{\sqrt{2}} - \frac{1}{\sqrt{2}}\left(\frac{\Phi}{\Phi_0}\right)\right), \tag{5.21}$$

and therefore

$$L_{J,0} = \frac{\Phi_0}{2\pi\,I_{0,\,SQUID}} \approx \frac{\Phi_0}{2\sqrt{2}\,\pi}\left(1+\frac{\Phi}{\Phi_0}\right). \tag{5.22}$$

The linear dependence will allow 3-wave mixing process ($\chi^{(2)}$-like).

The JPAs described in this thesis will all be based on 4-wave mixing processes by applying the pump tone as an ac current directly on the resonator. The alternative of an ac flux is not easy to implement in our system, since the use of SQUID arrays will difficult the application of an homogeneous external ac flux.

5.3.1 Classical response of a nonlinear oscillator

A resonator-based JPA is essentially a weakly nonlinear oscillator [33]. We can describe such a system by considering the Hamiltonian of an harmonic oscillator with a Kerr non-linearity K, where $K < 0$:

$$\mathcal{H} = \hbar\,\omega_0 \hat{a}^\dagger \hat{a} + \frac{\hbar\,K}{2}\,\hat{a}^\dagger \hat{a}^\dagger \hat{a}\,\hat{a}. \tag{5.23}$$

If the system has an external coupling and internal losses, we can take them into account by using input-output theory. We will first consider the case where only a strong coherent field α is applied which we can therefore model classically. Applying the usual input-output relations considering coupling and loss rates κ and γ will yield a cubic equation in $|\alpha|$,

$$iK\alpha\,|\alpha|^2 + \left(i(\omega_0-\omega_P) + \frac{\kappa+\gamma}{2}\right)\alpha = \sqrt{\kappa}\,\alpha_{in}, \tag{5.24}$$

where ω_P is the frequency of the strong applied signal (pump) and ω_0 is the resonant frequency of the linear system. This last expression can be solved analytically for α, and for weak input powers will give a single solution. However, as we keep increasing the input power, a critical value can be reached above of which the system has three different solutions, of which only two of them will be stable, therefore yielding a bistable solution. This behaviour can be observed in figure 5.1, where $\delta = \omega_P - \omega_0$. The green plot shows the oscillator with nonlinearity $K = 0$, the blue close to the bifurcation point where the slope becomes infinite, and the red a strongly nonlinear case, with a region having three solutions.

Once knowing the solutions of $|\alpha|$ we can write the reflection coefficient as

$$\Gamma = \frac{\kappa}{i(-(\omega_P-\omega_0) + K\,|\alpha|^2) + \frac{\kappa+\gamma}{2}} - 1, \tag{5.25}$$

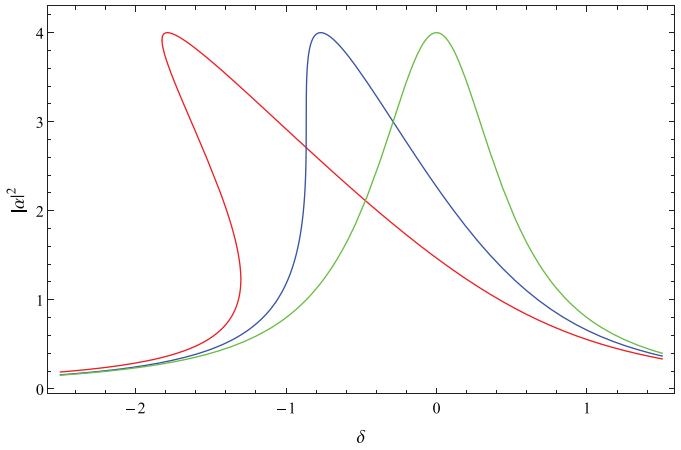

FIGURE 5.1: Population in the resonator as a function of the drive detuning δ, in units of κ, for a lossless nonlinear oscillator with three different nonlinearities, each corresponding to different regimes of the oscillator. The red plot corresponds to the strongest nonlinearity, the blue to an intermediate value and the green to the smallest.

where the value of $|\alpha|$ will depend on the frequency of the pump. Since $K < 0$ it will have the effect of redshifting the resonant frequency of the resonator as the input power increases.

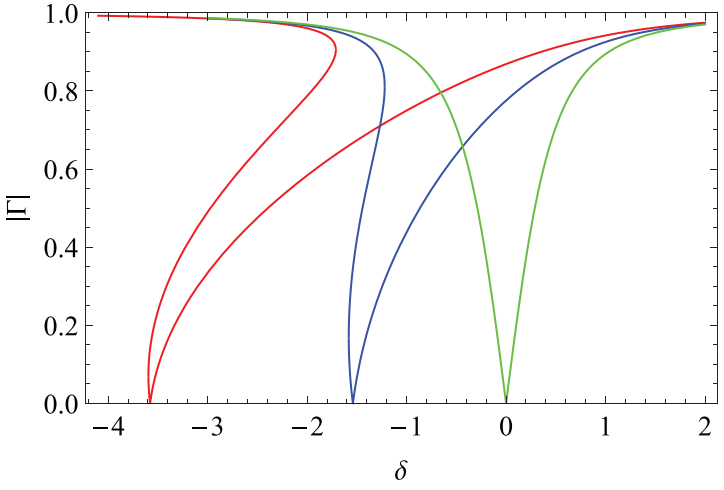

FIGURE 5.2: Reflection coefficient as a function of the drive detuning δ for a critically coupled nonlinear oscillator with varying nonlinearities. The red plot corresponds to the strongest nonlinearity, the blue to an intermediate value and the green to the smallest.

5.3.2 Gain in the linear regime

Let us now consider a weak quantum field $\hat{b}(t)$ together with the strong pump field $|\alpha|$, such that the input field obeys $\langle \hat{b}_{in}^{\dagger}(t)\hat{b}_{in}(t)\rangle \ll |\alpha_{in}|^2$. We can linearize the Hamiltonian such that only terms linear in $\hat{b}(t)$ will survive. We also consider overcoupling by $\kappa \gg \gamma$, and therefore ignore the internal losses. This allows us to write the same equations of motion for the classical drive as before, while the

quantum field will obey

$$\dot{\hat{b}}(t) = -i\tilde{\delta}\,\hat{b}(t) - iK\alpha^2\hat{b}^\dagger(t) + \sqrt{\kappa}\,\hat{b}_{in}(t), \tag{5.26}$$

$$\dot{\hat{b}}^\dagger(t) = i\tilde{\delta}\,\hat{b}^\dagger(t) + iK\alpha^2\hat{b}(t) + \sqrt{\kappa}\,\hat{b}^\dagger_{in}(t), \tag{5.27}$$

where $\tilde{\delta} = (-(\omega_P - \omega_0) - i\kappa/2 + 4K|\alpha|^2)$. These expressions can be rewritten in vector form as

$$\dot{\mathbf{b}}(t) = \mathcal{S}\,\mathbf{b}(t) + \sqrt{\kappa}\,\mathbf{b}_{in}(t), \tag{5.28}$$

specifically

$$\begin{pmatrix} \dot{\hat{b}}(t) \\ \dot{\hat{b}}^\dagger(t) \end{pmatrix} = \begin{pmatrix} -i\,\tilde{\delta} & -iK\alpha^2 \\ iK\alpha^{*2} & i\,\tilde{\delta} \end{pmatrix} \begin{pmatrix} \hat{b}(t) \\ \hat{b}^\dagger(t) \end{pmatrix} + \sqrt{\kappa} \begin{pmatrix} \hat{b}_{in}(t) \\ \hat{b}^\dagger_{in}(t) \end{pmatrix}. \tag{5.29}$$

Now we can use the Fourier transform

$$\hat{b}_i(t) = \frac{1}{\sqrt{2\pi}} \int_{-\infty}^{\infty} \hat{b}_i(\Delta) e^{-i\Delta t}\, d\Delta \tag{5.30}$$

where $\Delta = \omega_b - \omega_P$, and by introducing it to equation 5.28 will yield

$$\dot{\mathbf{b}}(\Delta) = (-\mathcal{S} - i\Delta)^{-1}\,\mathbf{b}_{in}(\Delta) = G(\Delta)\mathbf{b}_{in}(\Delta), \tag{5.31}$$

where $\mathbf{b}(\Delta) = (\hat{b}(\Delta), \hat{b}^\dagger(-\Delta))$. By using the input-output relation $\hat{b}_{out} = \sqrt{\kappa}\,\hat{b} - \hat{b}_{in}$ we can get to

$$\begin{aligned} b_{out}(\Delta) &= \kappa\, G_{11}(\Delta)\,\hat{b}_{in}(\Delta) + \kappa\, G_{12}(\Delta)\,\hat{b}^\dagger_{in}(-\Delta) - \hat{b}_{in}(\Delta) \\ &= g_{S,\Delta}\,\hat{b}_{in}(\Delta) + g_{I,\Delta}\,\hat{b}^\dagger_{in}(-\Delta), \end{aligned} \tag{5.32}$$

which shows that a signal at detuning from the pump Δ will get amplified by a factor $g_{S,\Delta}$ and also mixed with the components of the idle frequency with a factor $g_{I,\Delta}$.

The relevant properties which will characterize a parametric amplifier will be the maximum gain, the bandwidth and the dynamic range. The first two are given by the function $g_{S,\Delta}$, at a given pump-resonator detuning and input power $|\alpha_{in}|$ (if we only consider a single stable solution). However, the bandwidth will depend on the amplitude of the maximum gain [33], and it will in general not be wider than the linewidth of the resonator. Actually, as can be seen in figure 5.3, increasing the gain will reduce the bandwidth, which can be understood by approximating the curves as Lorentzians, implying that $|g_{S,0}|\,B \approx 1$.

The other relevant parameter, the dynamic range, characterizes the behaviour of the amplifier when the power of the signal is increased with a constant pump power. In the previous derivations we assumed that the signal to be amplified is always weak while the pump power is much stronger (stiff pump approximation), however, if we increase the signal power we may reach a regime in which the

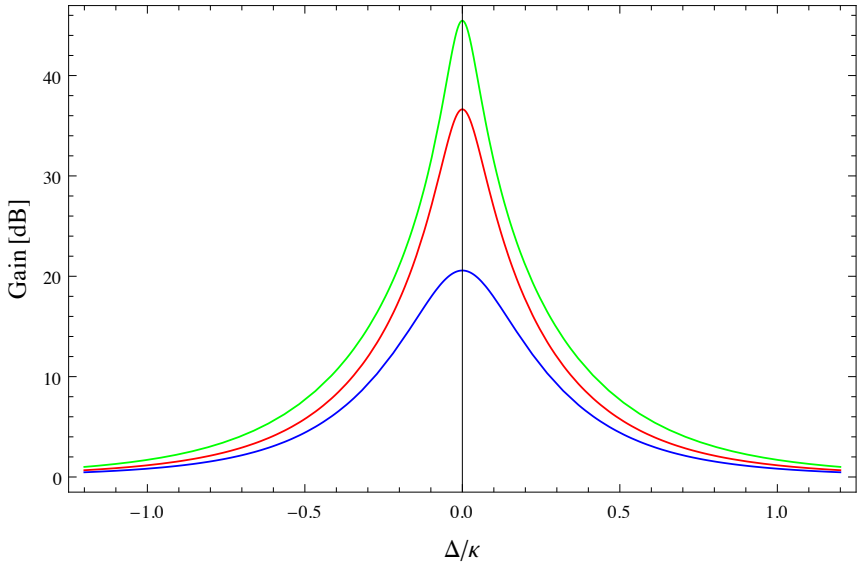

FIGURE 5.3: Gain curves as a function of Δ/κ for different pump powers. The green plot corresponds to the highest power and the green to the lowest.

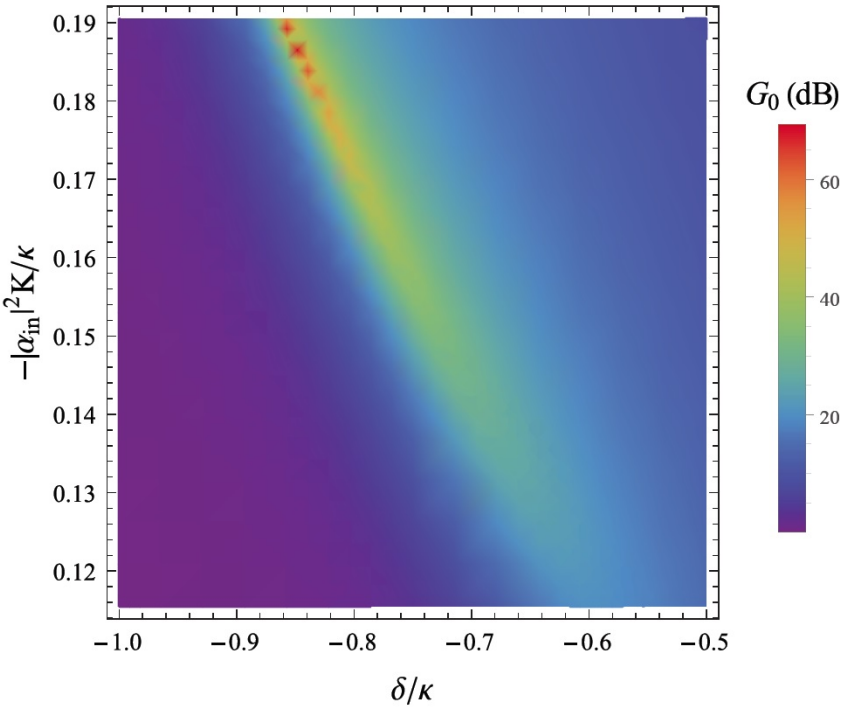

FIGURE 5.4: Phase diagram showing the gain of the amplifier at detuning $\Delta = 0$.

depletion of the pump power cannot be neglected, and for which the gain will start to decrease. As shown in [9], the 1 dB compression point of the JPA will increase for bigger values of the ratio κ/K. We conclude from this dependence that both the dynamic range and the bandwidth of the amplifier can be improved by increasing the coupling rate, and that decreasing the non-linearity will also help achieving a better dynamic range. We will address how to do so in the next subsection.

5.3.3 Lumped-element JPAs with asymmetric SQUID arrays

In this subsection we will describe the designed resonators with asymmetric SQUID arrays. We will start by considering a lumped-element resonator with a single shunting SQUID. The typical values for the shunt capacitance are $\sim 100-300$ fF, which leads to charging energies of $E_C \sim 50-200$ GHz, while typically the E_J of a SQUID is above 1 THz [34]. This implies that the resonator can be described by the Transmon Hamiltonian as

$$\mathcal{H} = 4\,E_C\,n^2 - E_J\cos\delta \approx 4\,E_C\,n^2 - E_J\left(1-\frac{\delta^2}{2}+\frac{\delta^4}{24}\right), \tag{5.33}$$

where we have approximated for small values of the gauge-invariant phase. By introducing creation and annihilation operators we can write the Hamiltonian in the form of a Duffing oscillator [35]

$$\mathcal{H} = -E_J + \sqrt{8\,E_J\,E_C}\left(\hat{a}^\dagger\hat{a}+\frac{1}{2}\right) - \frac{E_C}{12}\left(\hat{a}^\dagger+\hat{a}\right)^4, \tag{5.34}$$

which in the deep transmon limit ($E_J \gg E_C$) can be written as

$$\mathcal{H} = \sqrt{8\,E_J\,E_C}\left(\hat{a}^\dagger\hat{a}+\frac{1}{2}\right) - \frac{E_C}{2}\,\hat{a}^\dagger\hat{a}^\dagger\hat{a}\hat{a} = \hbar\,\omega_0\hat{a}^\dagger\hat{a} + \frac{\hbar\,K}{2}\hat{a}^\dagger\hat{a}^\dagger\hat{a}\hat{a}, \tag{5.35}$$

where $\omega_0 = 1/\sqrt{L_J\,C}$, $K = E_c/\hbar$ and where we removed the constant term $-E_J$. Now that we have shown that the transmon Hamiltonian is equivalent to the Daffing which we used for the previous derivations, let us address the question of improving the dynamic range and the bandwidth. Increasing the coupling rate κ is an option as we showed in the last subsection, but there are some limitations to an arbitrary increase of κ, since a stronger coupling will yield higher currents in the SQUID, whereas we assumed in several occasions that the currents across the SQUID were much smaller than the critical current. The important parameter is the ratio between the parametrically critical number of photons ($N_{\text{bifurcation}}$) and the number of photons corresponding to the critical current of the SQUID (N_{max}), which we want to keep as small as possible. In reference [33] this ratio is shown to be proportional to κ and in general much smaller in the lumped-element limit. This means that we will not be able to increase κ arbitrarily, but that lumped-element resonators are a better option than distributed-element ones.

We can still argue that the dynamic range can be improved by decreasing the non-linearity K. In the lumped-element case this could be done by increasing the shunt capacitance, but this is likely to increase the geometric inductance contribution, therefore forcing to reduce the bandwidth. Another option is using an array of M SQUIDs instead of a single SQUID with same Josephson energy. If we assume a Josephson energy of E_J/M for each SQUID and that the phase drop across each of them is δ/M, where δ is the phase drop across the whole array, we

can rewrite the Hamiltonian of eq. 5.33 as

$$\mathcal{H} = 4\,E_C\,n^2 - \sum_{i=1}^{M} M E_J \left(1 - \frac{1}{2}\left(\frac{\delta}{M}\right)^2 + \frac{1}{24}\left(\frac{\delta}{M}\right)^4\right)$$

$$= 4\,E_C\,n^2 - M^2 E_J - \frac{E_J}{2}\delta^2 + \frac{E_J}{24\,M^2}\delta^4, \tag{5.36}$$

from which we can extract that even if the Josephson inductance L_J, given by the quadratic term of the Hamiltonian, will be the same as for a single SQUID with E_J, the nonlinearity K, given by the quartic term, will be reduced by a factor of M^2. This yields then $K = E_C/M^2$, so that the nonlinearity was reduced while keeping the resonance frequency and the rest of parameters constant.

Last, there is an effect that should also be taken into account, the added noise. This noise can be introduced by the loss rate γ, which we assumed to be negligible, and it can only be reduced by identifying the loss sources and improving the design. However, there will also be another noise contribution given by fluctuations of the external magnetic flux, which will have stronger effects in the case of SQUID arrays. This contribution will originate fluctuations of the resonance frequency, which will reflect in a fluctuating effective gain. A way to cope with this effect is to reduce the frequency dependence on the magnetic flux fluctuations, which can be done by fixing the external dc flux at a sweet spot, but will limit the tunability. The solution we approach is the use of asymmetric SQUIDs, which as we saw in the previous section are more resilient to magnetic flux noise.

5.3.4 Degenerate and non-degenerate amplification

A parametric amplifier can be operated in two different regimes, depending on the detuning of the measured signal with respect to the pump frequency. In the degenerate or phase-sensitive amplification, the signal to be detected is centered around the pump frequency. In the non-degenerate, phase-insensitive or phase-preserving amplification, the detected signal is detuned far from the pump.

In the degenerate case, signal and idler occupy the same mode, and this leads to an interference effect which will noiselessly amplify one of the two quadratures of the mode while deamplifying the other quadrature. It is called phase-sensitive since by modifying the relative phase between the pump and the signal a generalized quadrature can be chosen to be amplified. This kind of amplification is usually used for fast dispersive readout of superconducting qubits, in which the state of the qubit can be encoded in only one of the quadratures [19].

In non-degenerate amplification signal and idler will be detuned by 2Δ, and both are equally amplified. This kind of amplification is used when the detection of the two quadratures of the signal is required, as for the measurement of photon

correlation functions, or also for multiplexed readouts [19].

For a JPA with a single resonance, as we have just seen, the gain will have a maximum at zero detuning from the pump frequency. This means that the signals to be amplified will have a limited detuning, and in general it will be more suitable for degenerate amplification. Since the pump is at the same frequency as the signal to be measured, it is necessary to cancel the pump in the output of the amplifier, to avoid saturation and noise in the measurement scheme. It is also important to note that the previous definitions for degenerate and non-degenerate amplification are in general valid for 4-wave mixing with a single pump. In situations with two pump signals or 3-wave mixing, degenerate amplification can be performed at a finite detuning from the pump [32].

5.4 Multi-cavity LE paramp

In this section we will describe the properties of Josephson parametric amplifiers where two or more coupled nonlinear resonators are involved. The interest for these kind of devices is found in their performance as parametric amplifiers [9], but also in their potential use for the quantum simulation of many-body systems.

The structure of these devices can be understood by combining the coupled linear resonators described in chapter 3, where parallel LC oscillators are coupled through a finger capacitor, with the use of SQUID arrays as nonlinear inductors as described in this chapter. The coupled system will display more than one eigenfrequency (as many as coupled resonators) with a detuning proportional to the effective coupling J. This means that degenerate amplification can be easily performed at each of these frequencies, each of them effectively behaving as a single resonator. However, if we choose two of those resonances and apply a pump at exactly the center between those frequencies, the 4-wave mixing process will allow to perform non-degenerate amplification, in which the pump and the idler can be considerably detuned from the amplified signal. The system can therefore be operated in the two different regimes, and it allows to amplify signals at very different frequencies simultaneously. A description and experimental test of a system of two coupled resonators were described by Eichler et al. in [9].

The Hamiltonian that describes nonlinear coupled resonators can be obtained from equation 4.37 and introducing the Kerr term for each one of the resonators we get to

$$\mathcal{H} = \sum_{i=1}^{N} \hbar\omega_i \left(\hat{a}_i^\dagger \hat{a}_i + \frac{1}{2}\right) + \sum_{j>i} \hbar J_{ij} \left(\hat{a}_i^\dagger \hat{a}_j + \hat{a}_j^\dagger \hat{a}_i\right) + \sum_{i=1}^{N} \frac{K}{2} \hat{a}_i^\dagger \hat{a}_i^\dagger \hat{a}_i \hat{a}_i. \tag{5.37}$$

If we consider all resonator-resonator coupling interactions to be equal and only afecting nearest-neighbours, the Hamiltonian can be rewritten as

$$\mathcal{H} = -J \sum_{\langle i,j \rangle} \hat{a}_i^\dagger \hat{a}_j + \sum_i \epsilon_i \hat{n}_i + \frac{U}{2} \sum_i \hat{n}_i(\hat{n}_i - 1), \tag{5.38}$$

where $\epsilon_i = \hbar\omega_i$, $J = -\hbar J_{i,i+1}$, $U = \hbar K$ and $\hat{n}_i = \hat{a}_i^\dagger \hat{a}_i$ is the photon number operator. This is exactly the Hamiltonian of the Bose-Hubbard model, which approximately describes the interaction of bosons in a lattice [36]. This is a Hamiltonian that has been intensely studied and experimentally implemented in systems of ultracold atoms in optical lattices [37]. The reason is that as the ratio of U/J is tuned, this Hamiltonian displays a quantum phase transition between a superfluid and Mott insulators states, and the quantum simulation of such systems can shine light into condensed matter problems which are difficult to solve with classical computers [1].

5.4.1 The Josephson Parametric Trimer

In this last subsection we will comprehensively describe the properties of a device composed of three coupled nonlinear resonators from theoretical calculations. In analogy to the previously designed two-resonator amplifier we call this device the Josephson parametric trimer (JPT), as it is a circuit realization of a Bose-Hubbard trimer. Even though we have designed coupled systems with a higher number of resonators, the JPT is the natural continuation of the JPD and it is also the smallest system which can show next-nearest neighbour interactions. In this particular thesis we will focus on it use as a parametric amplifier although many of the results could be useful for quantum simulations.

The Hamiltonian of the system can be written as

$$\mathcal{H} = \sum_{i=1}^{3} \hbar\omega_0 \left(\hat{a}_i^\dagger \hat{a}_i + \frac{1}{2} \right) + \sum_{j>i} \hbar J_{ij} \left(\hat{a}_i^\dagger \hat{a}_j + \hat{a}_j^\dagger \hat{a}_i \right) + \sum_{i=1}^{3} \frac{K}{2} \hat{a}_i^\dagger \hat{a}_i^\dagger \hat{a}_i \hat{a}_i, \tag{5.39}$$

where we consider the coupling between next-nearest neighbours, even though it is much smaller than the nearest-neighbour. We also consider that the resonance frequencies of the three resonators are the same. If we diagonalize the Hamiltonian by ignoring the nonlinear term and considering $J_{13} \approx 0$, we find three hybridized modes which can be written as

$$a_+ = \frac{(a_R + a_L) + \sqrt{2} a_C}{2}, \tag{5.40}$$

$$a_0 = \frac{a_R - a_L}{\sqrt{2}}, \tag{5.41}$$

$$a_- = \frac{(a_R + a_L) - \sqrt{2} a_C}{2}, \tag{5.42}$$

and with eigenfrequencies $\omega_+ = \omega_0 + \sqrt{2}J$, $\omega_C = \omega_0$, $\omega_- = \omega_0 - \sqrt{2}J$, where ω_0 is the bare resonance frequency of the resonators. The nonlinear term will shift the three eigenfrequencies proportionally to the applied coherent drive. If we solve the system by considering a strong classical field, as done in the previous section, we can plot the number of photons present in each of the resonators as a function of the detuning from the bare frequency, as shown in figures 5.5 and 5.6 for the linear and strongly nonlinear cases.

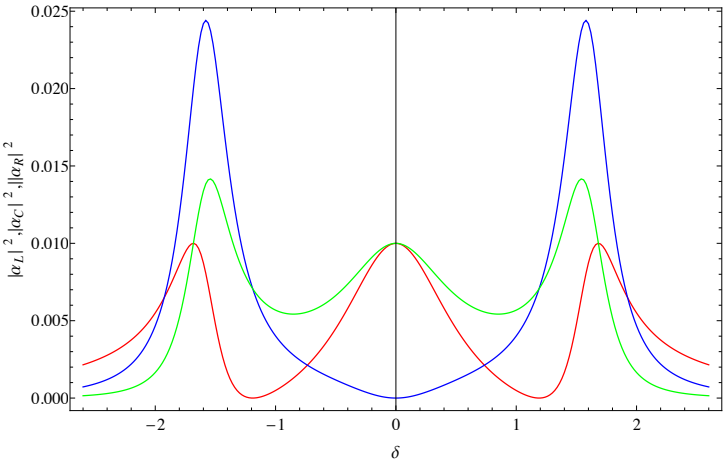

FIGURE 5.5: Number of photons present in each of the resonators in a linear trimer as a function of the applied frequency, written as the detuning from the bare resonance frequency in units of κ.

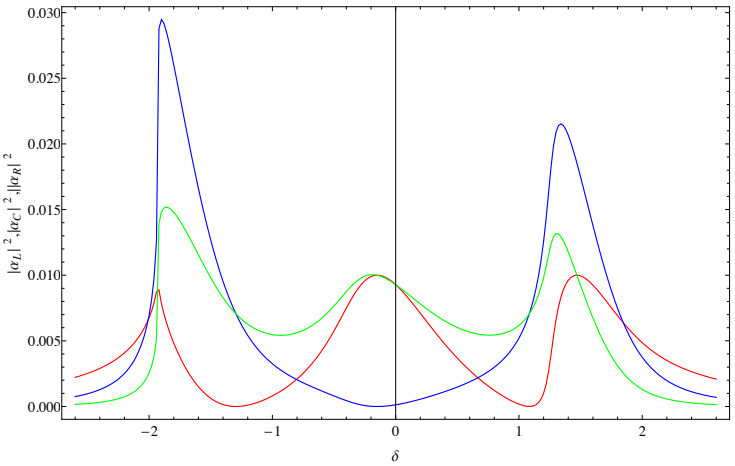

FIGURE 5.6: Number of photons present in each of the resonators in a nonlinear trimer as a function of the applied frequency, written as the detuning from the bare resonance frequency in units of κ.

By considering the operation of the trimer in the linear regime, we can calculate the gain in a similar way as with the single resonator case. However, since the trimer has three resonance modes, non-degenerate amplification will be possible by applying the pump at these frequencies, and the maximum of gain will not necessarily be at $\Delta = 0$. Therefore, to extract relevant information from solving

the gain equations it is necessary to take into account the values of Δ at which we might have strong gain. For the case of degenerate gain, we plot a phase diagram in the same way as for the single resonator, showing the gain at $\Delta = 0$ as a function of the two tunable parameters, the input power and the detuning δ. In the phase diagram seen in figure 5.7 we can distinguish the three resonance frequencies red-shifted as the power is increased.

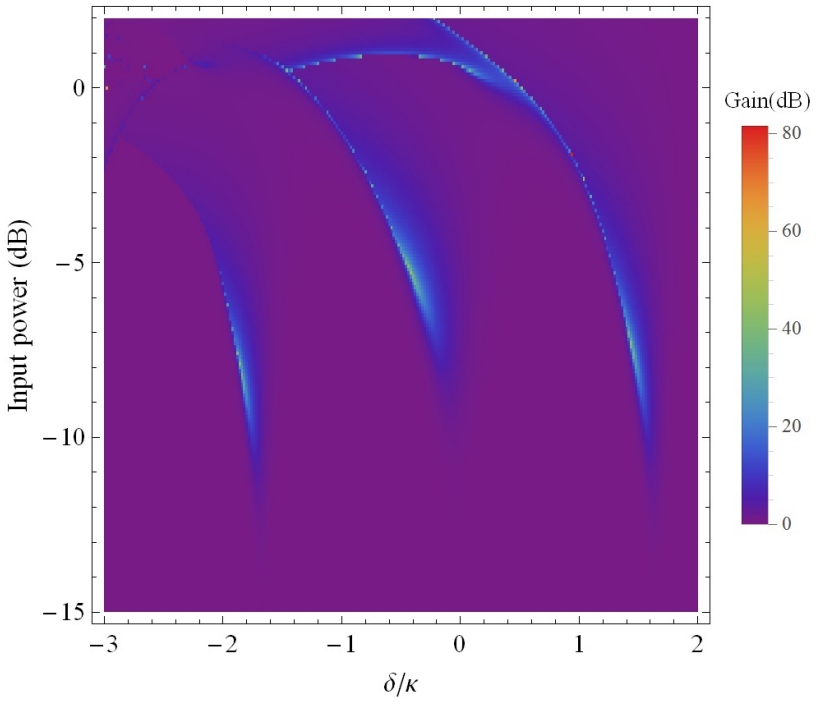

FIGURE 5.7: Degenerate phase diagram of the trimer, the value of the gain corresponds to its value at $\Delta = 0$. The input power in the coordinate axis has been chosen to make clearer the comparison with the experimental results. It can be expressed as $(|\alpha_{in}|^2 U/\kappa^2)(1 + \delta/\omega_0)$.

To show the non-degenerate behaviour in a phase diagram, a finite value of Δ (pump and signal detuned) has to be chosen. Since the trimer has three eigenfrequencies, we expect three different non-degenerate gains, each of them corresponding to the applied pump exactly between the eigenfrequencies. If we choose to observe the gain at the eigenfrequencies ω_+, ω_-, the pump will have to be at the eigenfrequency ω_0, and the detuning of maximum gain will be at $\Delta = \pm\sqrt{2}J$. We plot the phase diagram corresponding to this gain in figure 5.8, which we have obtained by finding the maximum in a narrow region around $\Delta = \pm\sqrt{2}J$.

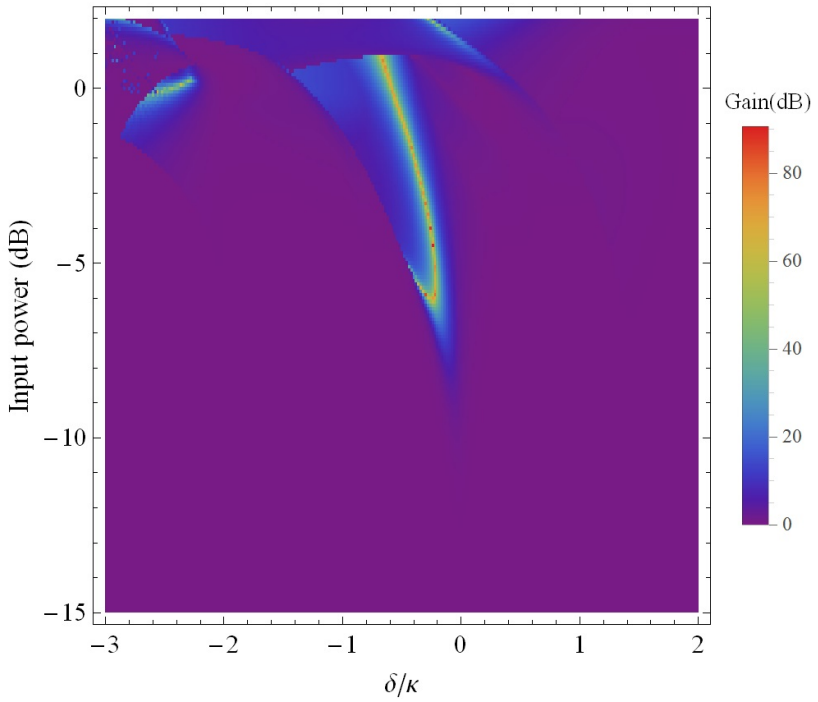

FIGURE 5.8: Non-degenerate phase diagram of the trimer, the value of the gain corresponds to its value at $\Delta \approx \sqrt{2}\,J$. The input power in the coordinate axis has been chosen to make clearer the comparison with the experimental results. It can be expressed as $(|\alpha_{in}|^2 U/\kappa^2)(1 + \delta/\omega_0)$.

In contrast to the results shown by the JPD [9], the JPT can be operated at the same power and detuning as a degenerate and a non-degenerate parametric amplifier, by applying the pump close to the central eigenfrequency, therefore obtaining gain at all the eigenfrequencies simultaneously. This is shown in figure 5.9, where this simultaneous behaviour can be observed.

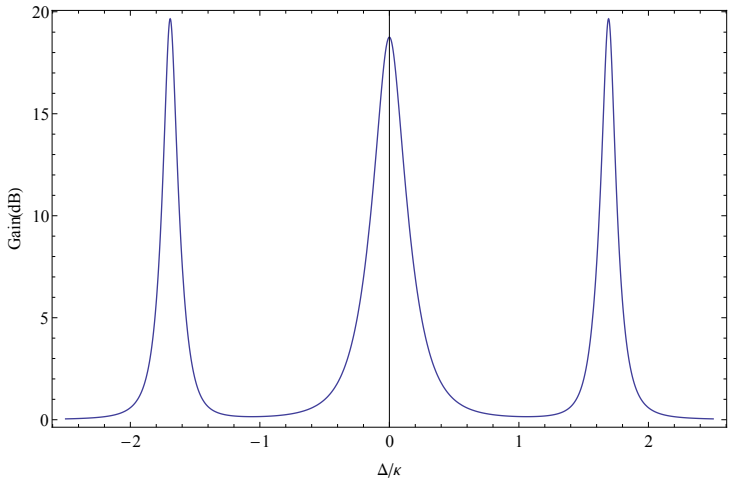

FIGURE 5.9: Gain as a function of the signal detuning Δ/κ, for a regime where both degenerate and non-degenerate amplification are equally strong.

Chapter 6

Experimental setup

The lumped-element superconducting resonators described in this thesis were characterized with two different setups. Samples without nonlinear SQUIDS were measured using a dipstick in a liquid helium dewar, where the temperatures attained of 4.2 K are already below the superconducting critical temperature of 9.2 K of niobium. In the case of non-linear resonators, with an aluminium SQUID array placed instead of the niobium meander inductor, temperatures lower than 1 K are needed and these measurements were done in a dilution refrigerator, which gets down to a few mK. Some of the linear samples were also measured in the dilution refrigerator to get the insight on the behaviour of the quality factor at mK temperatures. In the present section we will describe the details of each of these setups.

6.1 Dipstick measurements

All the measurements of frequencies and quality factors of linear resonators have been realized by a dipstick device in a liquid helium dewar, to thermalize them at 4.2 K. In this section we will summarize the procedure and calibration, comment on typical issues and model the cable structure.

6.1.1 The measuring procedure

The liquid helium dewar is chosen to have a wide enough neck for the dipstick to fit in. During the insertion of the dipstick the manometer is checked constantly to make sure that the pressure due to evaporated helium does not get too high, otherwise the dipstick could be ejected by excessively high internal pressure. To avoid this it is important to insert the dipstick slowly and carefully, and wait for the pressure to decrease whenever it rises notoriously. The insertion of the dipstick usually takes 3 minutes.

While the sample is superconducting, its resonance frequency is temperature-dependent due to kinetic inductance, as described by equation 3.1. To measure

all the samples at the same temperature, it is imperative that the sample is submerged far below the liquid Helium level and to wait for at least 5 minutes before proceeding with the measurement, since this will allow the pressure to be released to ambient pressure.

The dipstick we used has 8 ports, as seen in figures 6.1 and 6.2. SMA connectors on top of the dipstick are connected to the VNA and SMP connectors at the bottom are connected to the sample via bullets. The pins of this SMP connectors are particularly fragile and one has to be careful to avoid breaking or bending them while inserting the calibration standards samples.

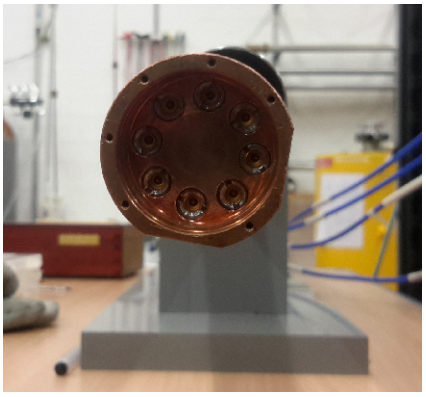

FIGURE 6.1: Picture of the lower part of the dipstick, with 8 SMP connectors which connect to the sample.

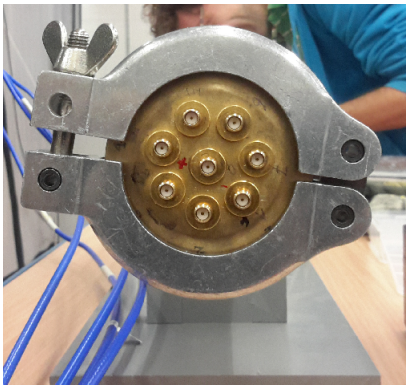

FIGURE 6.2: Picture of the upper part of the dipstick, with 8 external SMA connectors.

The VNA used for the scattering matrix measurements is the Agilent N5230. It has 4 ports, which means that we can measure all resonators of each sample by doing two measurements with the VNA. This can either be done by changing the connections to the dipstick while the sample is still inside the dewar or by taking out the sample and changing its position. The first has the advantage that the whole sample can be measured with a single dip in helium, while on the other case one has to wait for the sample to be at room temperature to change its position and dip it again. But on the other hand, for the latter method only a single calibration of the dipstick has to be done, the connections are not manipulated, and therefore the calibration can be better.

Once the whole setup is prepared, the spectrum is observed to find the resonance frequency and also to detect the presence of additional spurious modes. Then the data is collected with a narrower spectrum but covering the whole band of the resonance, around 5 times the linewidth. The whole 4-port scattering matrix is stored. This allows to study not only reflection measurements but also crosstalk between different samples on a chip.

In order to obtain from the measured files the resonance frequency and the different quality factors the measured spectra are fitted using the method described in the appendix A.

6.1.2 The calibration process

Before doing any measurement of the sample, it is necessary to perform a calibration of the dipstick cables through the VNA. This is specially required for the measurement of undercoupled and overcoupled samples. In reflection measurements it is usually enough to calibrate the cables which connect the network analyser to the device under test, which can be done by using electronic calibration. However, since at the end of the dipstick the cables are rigid and in the sample holder SMP connectors are used, electronic calibration is not possible. Therefore it has to be done manually with the Rosenberger SMP calibration kit (DUT: SMP Qudev, Male). The kind of calibration performed is the so-called short-open-load-reciprocal-thru (SOLR)[38]. It requires to measure each of the 4 ports with the 3 different standards and also a thru connection with one other specific port (1-2, 1-3, 1-4). This process consists of 15 steps which have to be done carefully to avoid breaking connector pins or connecting the standards weakly. For samples which only require reflection measurements, individual SOL calibration to each port can be performed, which can be loaded as four independent calibrations.

For a good calibration it is important to take a suitable amount of points, a bandwidth as narrow as possible and the same power as for the measurements which are intended to be done. This last point can be extremely important, as our particular VNA changes the calibration configuration every 10 dBm of calibration power difference. This can lead to the appearance of standing wave wiggles which would not be seen with a calibration at the corresponding power.

6.1.3 Possible issues

To perform the measurement properly the following issues have to be considered:

- High power: Using high powers for the measurement decreases the need of averaging, but the high electric current through the resonator might cause observable nonlinear effects and even reach the critical current, where superconductivity is broken down. A power of -30 dBm is a good choice for most samples, given by a compromise between avoiding non-linearities and having a large signal-to-noise ratio.
- Calibration: An excellent calibration is the main ingredient for collecting correct data. Without a proper calibration, standing wave modes given by the cables will appear in the measurement, as well as a frequency dependent phase shift due to phase delay.

- Incorrect closing of the sample holder: The sample holder has to be closed completely, without letting empty space between the two parts of the sample holder, as otherwise spurious microwave modes might be observed with the VNA. To be able to do so it is important to check the state of the pins and the bullets, which need to be of the right size (19k1).
- High temperature noise subtraction: Defects like phase delay are taken into account in the calibration, but since the measurements are done at cryogenic temperatures while the calibration is done at room temperature, the calibration will not be exact enough.
- Temperature stability: As discussed above, the sample should be introduced as deep as possible to ensure proper thermalization of the sample.

6.1.4 Model for cable reflection

To understand why some calibrated VNA measurements show a reflection coefficient with values higher than 1, we describe a simple model for the dipstick [39]. In the model we consider the VNA and the measured resonator at each side of the measurement setup, while the connections are simplified in two parts: the cables of the dipstick and the conductors of the PCB.

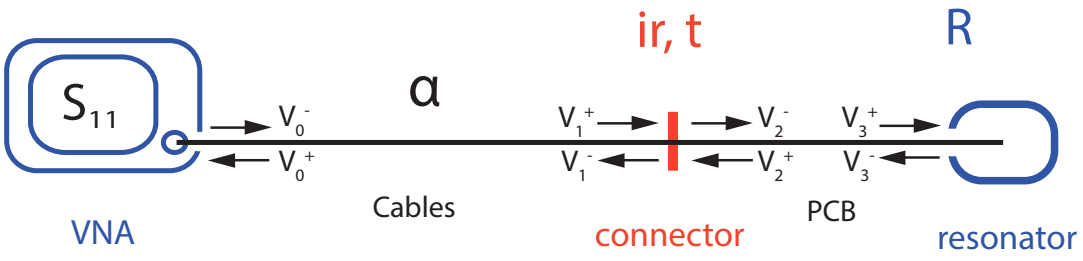

FIGURE 6.3: Sketch of the model used for characterizing cable reflection.

We can model the incoming and outcoming signals in the VNA, in the resonator and also in the two sides of the connector between the PCB and the cables of the dipstick. We consider only attenuation losses in the cable (α), but phase shifts for both the cables and the PCB. We also consider reflection and transmission coefficients of the connector (r, t) and the reflection coefficient R of the resonator. Having taken these into account we can now write the relations between the different signals. First, the attenuation and phase shift of the cables are described by

$$V_1^+ = \alpha e^{i\phi_1} V_0^-, \tag{6.1}$$

$$V_0^+ = \alpha e^{i\phi_1} V_1^-, \tag{6.2}$$

while the relationship between the signals near the connector is described by the expression

$$\begin{pmatrix} V_2^- \\ V_1^- \end{pmatrix} = \begin{pmatrix} t & ir \\ ir & t \end{pmatrix} \begin{pmatrix} V_1^+ \\ V_2^+ \end{pmatrix}. \tag{6.3}$$

The phase shift in the PCB is given by

$$V_3^+ = e^{i\phi_2} V_2^-, \tag{6.4}$$
$$V_2^+ = e^{i\phi_2} V_3^-, \tag{6.5}$$

and the reflection of the resonator leads to

$$V_3^- = iRV_3^+. \tag{6.6}$$

If we now proceed to solve the previous expressions, we can derive the expression for the reflection coefficient [39]

$$S_{11} = \frac{V_0^+}{V_0^-} = \alpha^2 i e^{-2i\phi_1} \frac{Re^{-2i\phi_2} + r}{1 + rRe^{-2i\phi_2}}, \tag{6.7}$$

which for small values of r can be rewritten as

$$S_{11} \approx \alpha^2 i e^{-2i\phi_1} \left(Re^{-2i\phi_2}(1 - rRe^{-2i\phi_2}) + r \right). \tag{6.8}$$

If we assume that the calibration of the VNA normalizes the measured reflection parameter, we have to take into account that the attenuation losses will be different for the helium measurements with respect to the room temperature measurements. Therefore the final expression for the approximated case will be

$$S_{11} \approx \frac{\alpha_{He}^2}{\alpha_{RT}^2} i e^{-2i\phi_1} \left(Re^{-2i\phi_2}(1 - rRe^{-2i\phi_2}) + r \right). \tag{6.9}$$

Since the losses should be smaller for the helium case, the calibrated reflection coefficient can have absolute value bigger than 1.

6.2 The Vericold dilution refrigerator

All the measurements of parametric amplifiers were performed with the measurement setup of the dilution refrigerator Vericold. A graphic depicting the basic structure of our measurement setup is shown in figure 6.4, based on the figure and details given in the PhD thesis of Arjan Van Loo [40].

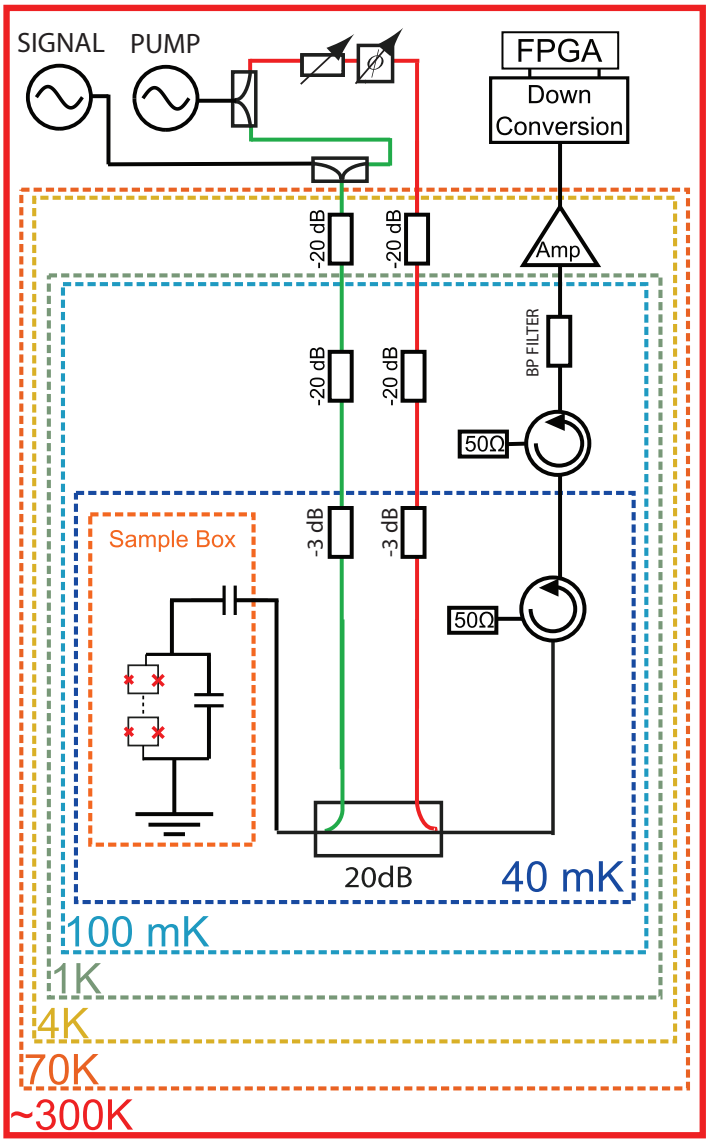

FIGURE 6.4: Schematic of the cabling in the Vericold fridge for the measurement of nonlinear samples.

Chapter 7

Experimental results

In this chapter we present the measurement results and the analysis. The first three sections are focused on characterizing linear resonators and extracting the circuit parameters from the measurements. The last two sections analyse the tunability of nonlinear resonators and their use as parametric amplifiers.

7.1 Parameter extraction and design model

To be able to precisely design resonators with specific circuit parameters (capacitances and inductances) it is desirable to have a simple model which yields an estimate of the resulting circuit parameters given the design parameters (number of fingers, meander turns). The simulations discussed in chapter 3 can be used together with the measured frequencies to extract all parameters. However, by using the method explained in chapter 4, it is possible to extract all the circuit parameters only from the measurements. In this section we will show such an extraction by measuring the resonances of two identical unloaded resonators, one with very weak coupling and the other with very strong. The results will then be used to extract the circuit parameters from three different studies (shunt capacitance, shunt inductance and coupling capacitance) and build a design model.

7.1.1 Weak-Strong Coupling (WSC)

The design details of the Weak/Strong Coupling samples are shown in table 7.1. We expect the weakly coupled sample to have a coupling capacitance of around 1 fF, which is considerably smaller than the expected shunt capacitance, allowing us to ignore the contribution due to coupling to the resonance frequency.

	C. capacitor	**S. capacitor**	**Inductor**	**Sim.** $C\kappa$	**Sim.** C
Weak (1)	Gap of 70 μm	8 fingers	21 turns	1.26 fF	133 fF
Strong (2)	12 fingers	8 fingers	21 turns	65.7 fF	135 fF

TABLE 7.1: Table showing the design parameters of the chip WSC 1. It is important to note that the strongly coupled sample has a smaller finger width and gap than the rest of fabricated samples, to increase the coupling strength.

The strongly coupled resonator has a very small quality factor, and this leads to a larger uncertainty in the measurements, and therefore they have been repeated several times for different identical samples. In table 7.2 we show the measured parameters, where the uncertainty has been determined by repeating the measurement for each of the samples. Since the interaction with the environment is very strong, already different connectors may lead to different measured values. The uncertainties shown for the mean are equal to the standard deviation of the measurements.

	Weak f_0 **(GHz)**	**Strong** f_0 **(GHz)**	**Strong** Q_L
WSC1 1	10.492(1)	8.70(2)	20.4(15)
WSC1 2	10.561(1)	8.65(2)	17.7(15)
WSC1 3	10.574(1)	8.72(2)	19.4(15)
Mean	10.54(4)	8.70(3)	19.2(15)

TABLE 7.2: Summary of the measurement results of the weak and strongly coupled samples together with their mean.

From the measured data and the equations at the end of section 4 we can extract the parameters with their corresponding propagated uncertainty, as shown in table 7.3. The obtained capacitance values are within the values obtained from Maxwell dc simulations, shown in table 7.1, and the value of the inductance is slightly higher than the one expected from the calculations in chapter 3, which was of around 1.5 nH. This additional contribution can be explained by the additional inductance from the island, which has been estimated to be around 0.15 nH. Also a small contribution will come from kinetic inductance, but it has been estimated to be smaller than 0.03 nH, as explained in appendix B.

	C **(fF)**	C_κ **(fF)**	L **(nH)**
WSC1 1	124(9)	57(4)	1.86(14)
WSC1 2	122(11)	59(5)	1.86(16)
WSC1 3	126(10)	63(5)	1.81(15)
Mean	124(11)	60(5)	1.84(16)

TABLE 7.3: Extracted circuit parameters obtained from the resonator measurements.

7.1.2 Shunt Capacitance (SC)

The results obtained from the mean values of the measured parameters in the last subsection have been used to extract the parameters from three different studies where shunt capacitance, shunt inductance and coupling capacitance were swept with the rest of parameters kept constant and identical to those of the WSC weak resonator. The study SC1 determines how shunt capacitance changes with the variation of the number of fingers. In table 7.4 we show the number of fingers on the shunt capacitor, the measured frequencies and the extracted shunt capacitances of each measured sample compared to the values obtained from dc Maxwell simulations. The extracted and simulated values show agreement within their uncertainty. In figure 7.1 we represent the inverse square of the frequency, which is proportional to the product LC, as a function of the number of shunt fingers, which together with a linear fit shows the linear behaviour of the shunt capacitance as a function of the finger number.

Sample	**Fingers**	f_0 **(GHz)**	**Extracted** C **(fF)**	**Simulated** C **(fF)**
SC1 1	0	16.924	48(4)	46.6(7)
SC1 2	1	16.645	49(4)	48.3(9)
SC1 3	2	14.808	63(5)	63.8(12)
SC1 4	4	12.868	83(7)	84.0(15)
SC1 6	10	9.967	138(12)	145(3)
SC1 7	17	8.452	192(16)	205(4)
SC1 8	26	7.137	269(24)	295(6)

TABLE 7.4: Measured resonance frequencies of the sample SC1 and corresponding extracted and simulated shunt capacitances. The extracted capacitance has been calculated as $C = f_0^{-2}/L$, where the value of L was taken from table 7.3.

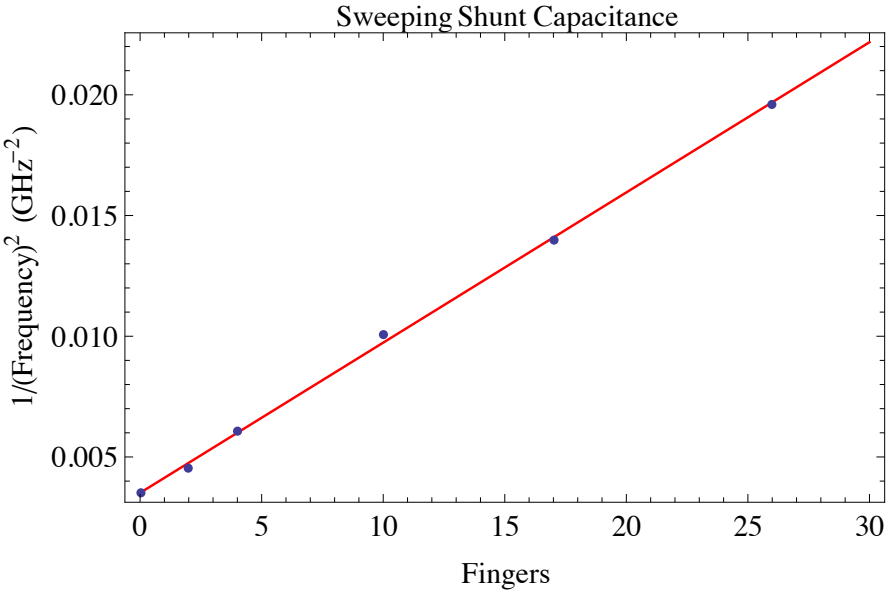

FIGURE 7.1: Plot of the inverted square of the measured frequencies of SC1 as a function of the sweeping parameter, the number of shunt capacitor fingers. The red curve is a linear fit of the measured points.

7.1.3 Shunt Inductance (SI)

In table 7.5 we show the swept number of meander turns, the measured frequencies and the extracted inductances, obtained by using the value of C from table 7.3. We also show the values of inductance obtained from the measured frequencies and the simulated capacitances, which are in agreement with the extracted parameters, though they are also higher than the estimations from chapter 3, which are also shown in the last column. In figure 7.2 we represent the inverse square of the frequency as a function of the number of meander turns and a corresponding linear fit, which clearly indicates the linear dependence of the inductance as a function of the number of turns (stripes).

Sample	**Stripes**	f_0 **(GHz)**	**Extr.** L **(nH)**	**Sim.** L **(nH)**	**Calc.** L **(nH)**
SI1 2	1	18.728	0.58(5)	0.54(1)	0.10(5)
SI1 3	2	17.735	0.65(6)	0.60(1)	0.20(5)
SI1 4	3	16.868	0.72(6)	0.66(1)	0.25(5)
SI1 5	10	13.355	1.15(11)	1.06(2)	0.40(5)
SI1 6	14	11.936	1.44(13)	1.33(2)	1.10(5)
SI1 7	21	10.416	1.89(17)	1.74(3)	1.50(5)
SI1 8	30	9.165	2.45(19)	2.25(4)	1.95(5)

TABLE 7.5: Measured resonance frequencies of the sample SI1 and corresponding extracted, simulated and calculated inductances. The extracted capacitance has been calculated as $L = f_0^{-2}/C$, where the value of C was taken from table 7.3.

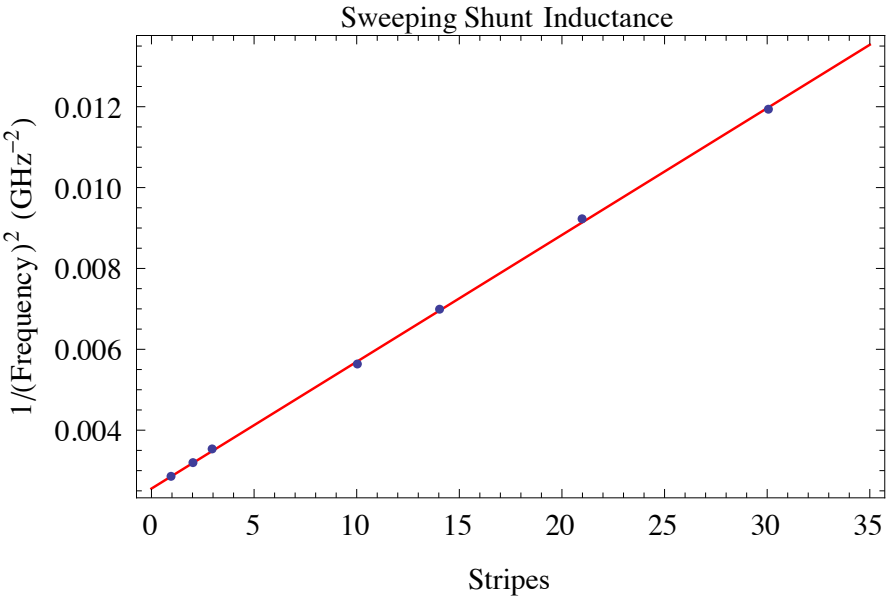

FIGURE 7.2: Plot of the inverted square of the measured frequencies of SI1 as a function of the sweeping parameter, the number of meander inductor turns. The red curve is a linear fit of the measured points.

7.1.4 Coupling Capacitance (CC)

In table 7.6 we show the swept number of coupling capacitor fingers, the measured frequencies and the extracted and simulated coupling capacitances. The extracted and simulated values show worse agreement for the weakly coupled cases, due to the fact that the extraction method considers the coupling capacitance to be practically zero for these cases. In figure 7.3 we represent the inverse square of the frequency as a function of the number of capacitor fingers and a corresponding linear fit, in which the linear behaviour is only appreciable for small coupling, due to the increase in the uncertainty of the resonance frequency.

	Fingers	f_0 **(GHz)**	Q_{loaded}	**Extracted** C_κ **(fF)**	**Simulated** C_κ **(fF)**
CC1 1	0	10.536	1671.3	0.094(8)	0.86(1)
CC1 2	2	10.128	300.5	10.3(9)	8.05(14)
CC1 3	3	9.991	150.0	14.0(12)	13.2(3)
CC1 4	4	9.783	76.0	19.9(17)	18.2(4)
CC1 5	7	9.387	30.7	33(3)	33.7(6)
CC1 6	10	8.849	29.8	53(5)	48.7(9)
CC1 7	17	8.054	13.3	94(8)	84.6(15)
CC1 8	25	7.633	10.7	120(9)	125(2)

TABLE 7.6: Measured resonance frequencies of the sample CC1 and corresponding extracted and simulated coupling capacitances.

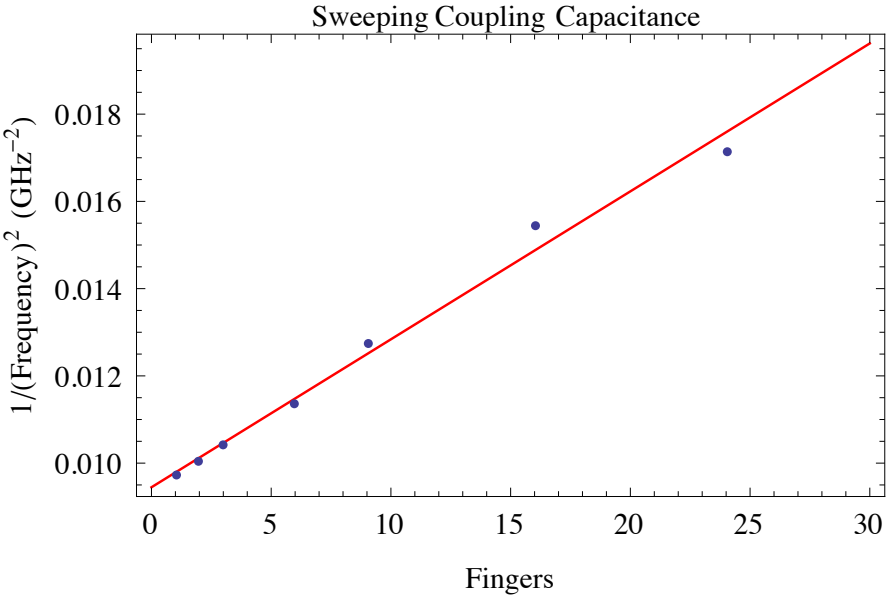

FIGURE 7.3: Plot of the inverted square of the measured frequencies of CC1 as a function of the sweeping parameter, the number of fingers. The red curve is a linear fit of the measured points.

Similar conclusions about the linear parameter dependence have been obtained from the analysis of previous studies with a slightly different circuit design. These results are shown in appendix B.

7.1.5 Design model

With the extracted values of shunt capacitance, coupling capacitance and shunt inductance we are able to construct a model which estimates the circuit parameters as a function of the design parameters. To do so we assumed a linear dependence on the design parameters (number of fingers or turns), which is supported by the linear fits shown for each of the studies and also by the dc simulations from chapter 3. This linear dependence can also be explained by assuming the contribution to the reactive parameters of each finger capacitor or meander turn to be identical. The expressions which model each of the components of the resonators are

$$C_{SC} = a_{SC} \cdot n_{SC} + b_{SC}, \tag{7.1}$$

$$L_{SI} = a_{SI} \cdot n_{SI} + b_{SI}, \tag{7.2}$$

$$C_{CC} = a_{CC} \cdot n_{CC} + b_{CC}, \tag{7.3}$$

where n_{SI} is the number of meander turns on the inductor and $n_{SC} + 1$, $n_{CC} + 1$ are the number of finger capacitors on the shunt and coupling capacitors. The extracted coefficients of the model obtained by the linear fits of each study are shown in table 7.7.

	a	**b**
SC	8.62(16) fF	55.0(18) fF
SI	0.0644(5) nH	0.525(8) nH
CC	5.03(18) fF	5(2) fF

TABLE 7.7: Coefficients of the design model obtained from a linear fit of the extracted parameters for the shunt capacitor (SC), shunt inductor (SI) and coupling capacitor (CC) studies.

The obtained designed model can be used to predict the resonance frequency and the coupling rates of designed resonators. To show the agreement between the estimated and the measured values, we plot in figures 7.4, 7.5, 7.6 the measured frequencies as a function of the design parameters together with a curve given by the design model and equation 4.47.

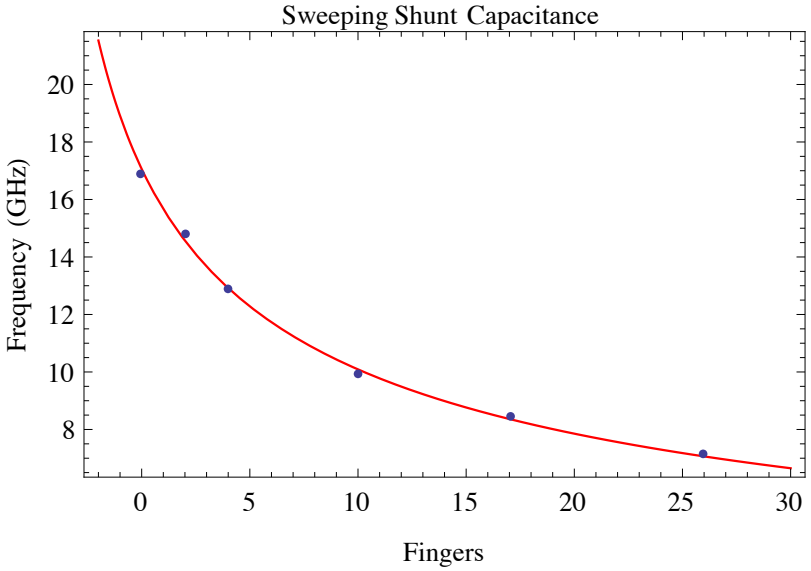

FIGURE 7.4: Plot of the measured frequencies of SC1 as a function of the number of shunt capacitor fingers. The red curve shows the estimated frequencies determined by our design model.

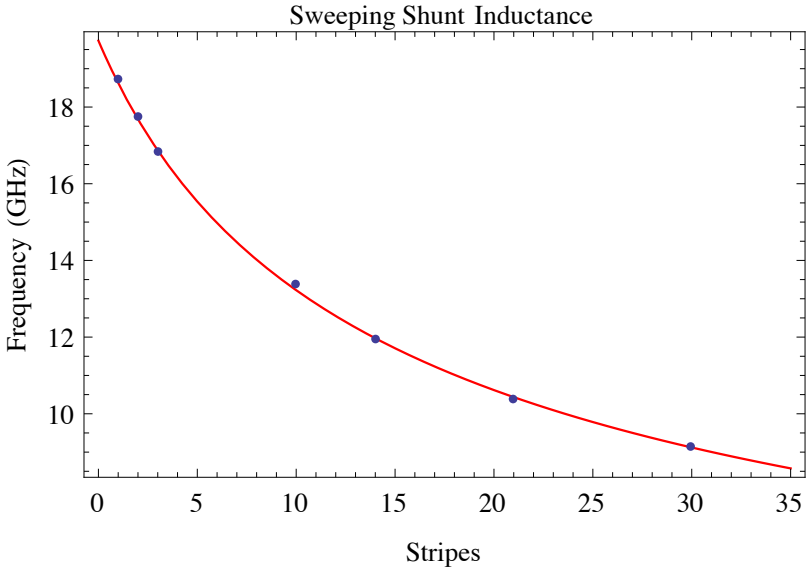

FIGURE 7.5: Plot of the measured frequencies of SI1 as a function of the number of meander turns. The red curve shows the estimated frequencies determined by our design model.

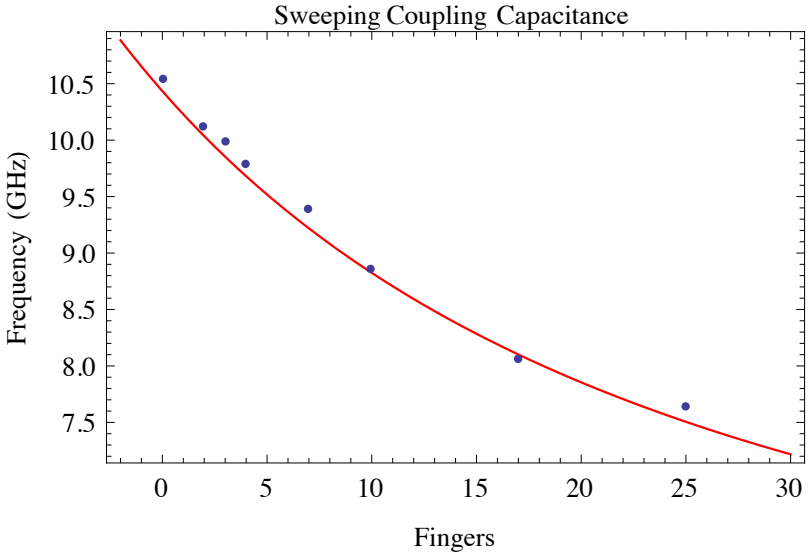

FIGURE 7.6: Plot of the measured frequencies of CC1 as a function of the number of coupling capacitor fingers. The red curve shows the estimated frequencies determined by our design model.

The worse agreement for the coupling capacitor study might be explained by a deviation of the ideal 50 Ω characteristic impedance of the transmission line.

7.2 Design model applied to coupled resonators

As described in chapter 3, arrays of two and three coupled linear resonators were fabricated with the same design characteristics as the single resonators. In figure 7.7 we show the measured reflection coefficient of a sample with three coupled resonators, whose fitted parameters are shown in 7.8. This sample has the same design parameters as the measured JPT for parametric amplification in section 7.5.

	Bare res. freq. (GHz)			**Coupling rates (MHz)**				
	$\omega_{0,1}$	$\omega_{0,2}$	$\omega_{0,3}$	J_{12}	J_{23}	J_{13}	κ	γ
JPT	7.665	7.651	7.418	392	387	-9	375	2

TABLE 7.8: Parameters obtained from the fit of the measured reflection coefficient of figure 7.7.

By using the design model shown in the previous section and calculating the impedance of the equivalent circuit it is possible to calculate the estimated eigenfrequencies of the samples with coupled resonators and compare them to the measured experimental values. This has been done for samples with two and three coupled resonators by using the parameters of tables 7.9 and 7.10. The discrepancies between the expected and experimental frequencies are represented in figures 7.8 and 7.9. The discrepancy is obtained by subtracting the measured frequencies from the estimated ones and normalizing with the measured frequency. The

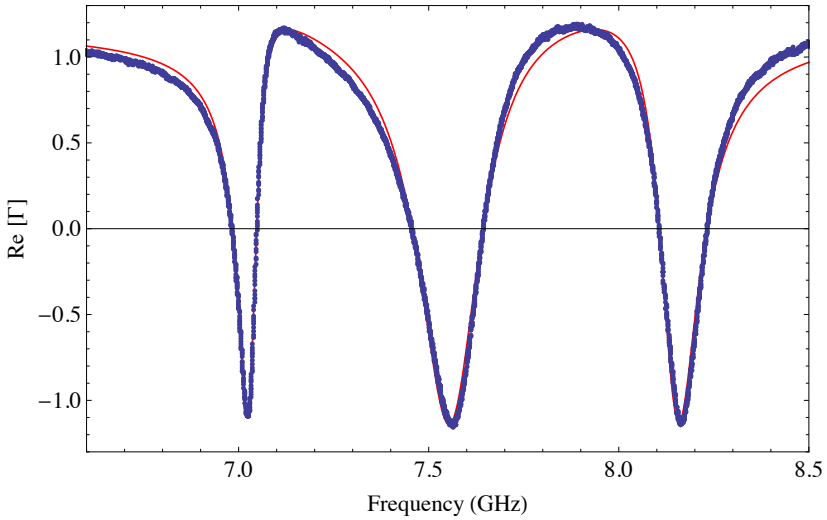

FIGURE 7.7: Measured real part of the reflection coefficient as a function of the applied frequency. The red plot shows a fit based on the reflection function obtained from input-output theory whose parameters are shown in 7.8.

agreement between the eigenfrequencies obtained from the model and the measured ones is shown to be better than 1% for the two cases, though the accuracy is better for the case of three coupled resonators. This is probably caused by the fact that the samples with two coupled resonators have much stronger coupling, as is shown in figures 3.8, 3.9.

Dimer Parameters		
	a	**b**
SC	8.75 fF	73 fF
SI	0.0649 nH	0.53 nH
CC	4.85 fF	3 fF
J	4 fF	0 fF

TABLE 7.9: Design model parameters used to obtain the eigenfrequencies of the dimer samples in figure 7.8.

Trimer Parameters		
	a	**b**
SC	8.62 fF	55 fF
SI	0.0639 nH	0.517 nH
CC	4.85 fF	3 fF
J	4.45 fF	3 fF

TABLE 7.10: Design model parameters used to obtain the eigenfrequencies of the trimer samples in figure 7.9.

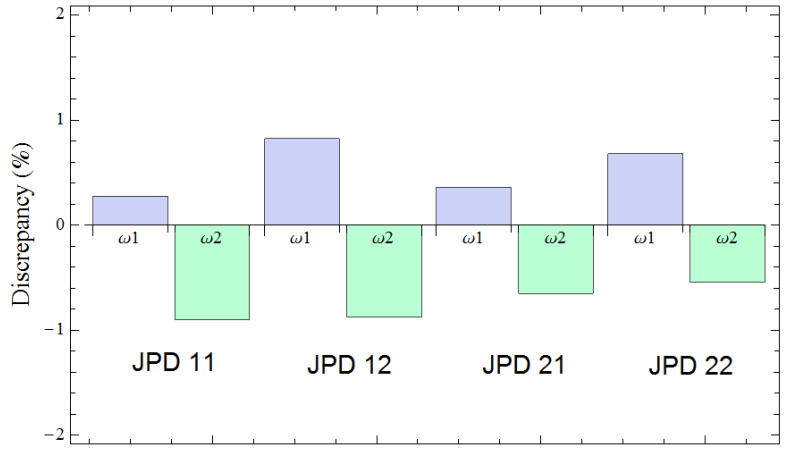

FIGURE 7.8: Chartbar of the relative discrepancies of the two eigenfrequencies of 4 different samples with two coupled resonators (JPD 11, JPD 12, JPD 21, JPD 22).

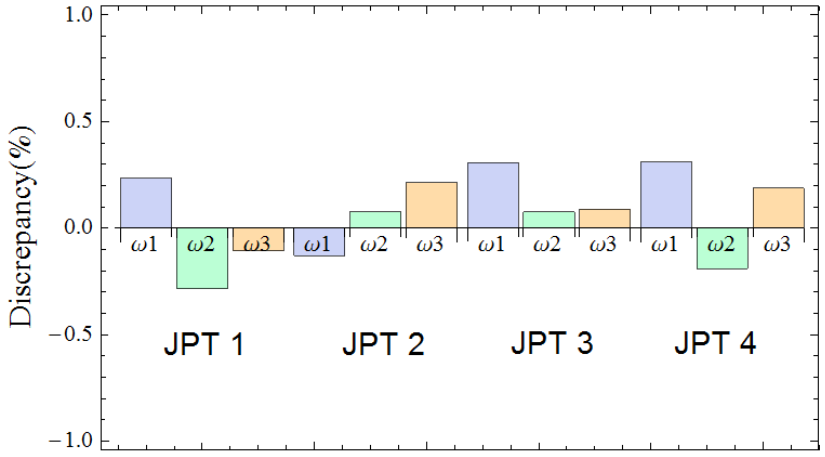

FIGURE 7.9: Chartbar of the relative discrepancies of the three eigenfrequencies of 4 different samples with three coupled resonators (JPT 1, JPT 2, JPT 3, JPT 4).

7.3 Reproducibility of the sample measurements

An important topic to be discussed is the impact of fabrication uncertainty on the reproducibility of the resonators. Due to wafer inhomogeneities or limited lithographic precision, different resonators designed to be identical can display different frequencies or quality factors, corresponding to variations on the fabricated structures. To get an idea of this effect, the weakly coupled resonator used to extract the parameters in the previous section (WSC 1) was fabricated and measured in two copies of a chip with 8 of these resonators (EWC). The results are shown in figure 7.10, and it can clearly be seen that there is a frequency shift between the samples which had a vertical and an horizontal arrangement on the chip. This points to a fabrication anisotropy, probably originated during the photolithographic process of the mask. The uncertainty in the frequency of the fabricated samples is around 20 MHz, but if we take into account this asymmetry it is smaller than 10 MHz. A

similar result has been obtained from measurements of another mask, obtaining the results of figure 7.11, which also agree with the recent results.

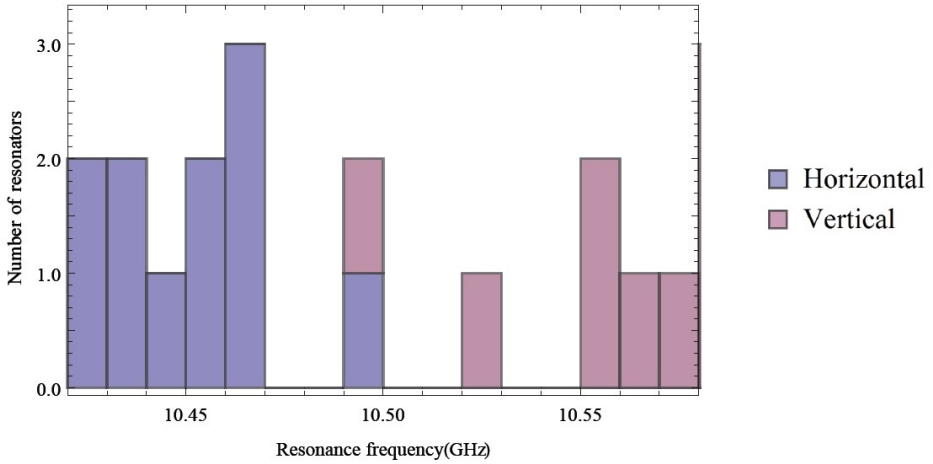

FIGURE 7.10: Histogram of the resonance frequencies of 17 samples identical in design of the chip EWC in mask 40.

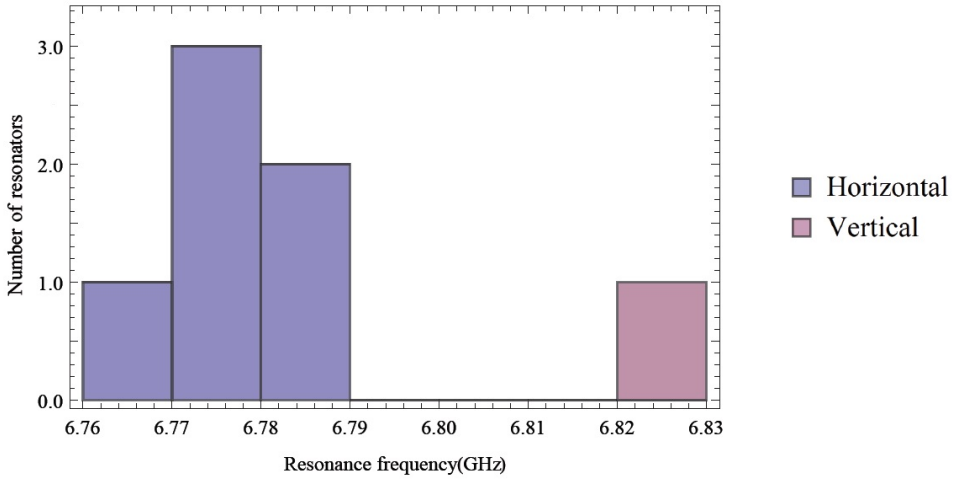

FIGURE 7.11: Histogram of the resonance frequencies of 7 samples identical in design from mask 36.

7.4 Single nonlinear resonator

In this section we present the results obtained from measuring single nonlinear resonators in the Vericold setup. First we are going to consider these samples as frequency tunable resonators. To do so, a magnetic field has been applied to the samples with an external coil on the base of the sample holder, which will tune the SQUIDs' effective critical current, as described in equation 5.18. In figure 7.12 we plot the measured phase in a reflection measurement as a function of the applied frequency and the voltage on the magnetic coils. We can see how the resonance

frequency is tuned by modifying the voltage applied to the coils, as explained in chapter 5.

	FINGER NUMBER		**SQUID ARRAYS**	
	C_k **fingers**	C **fingers**	**Number of SQUIDs**	**Asymmetry**
JPM	12	12	30	1/3

TABLE 7.11: Design parameters of the chips JPM1, JPM2, each having two nonlinear resonators. The 4 samples have the same values of the parameters, though in JPM2 the position of the fingers is flipped. SC refers to Shunt Capacitor.

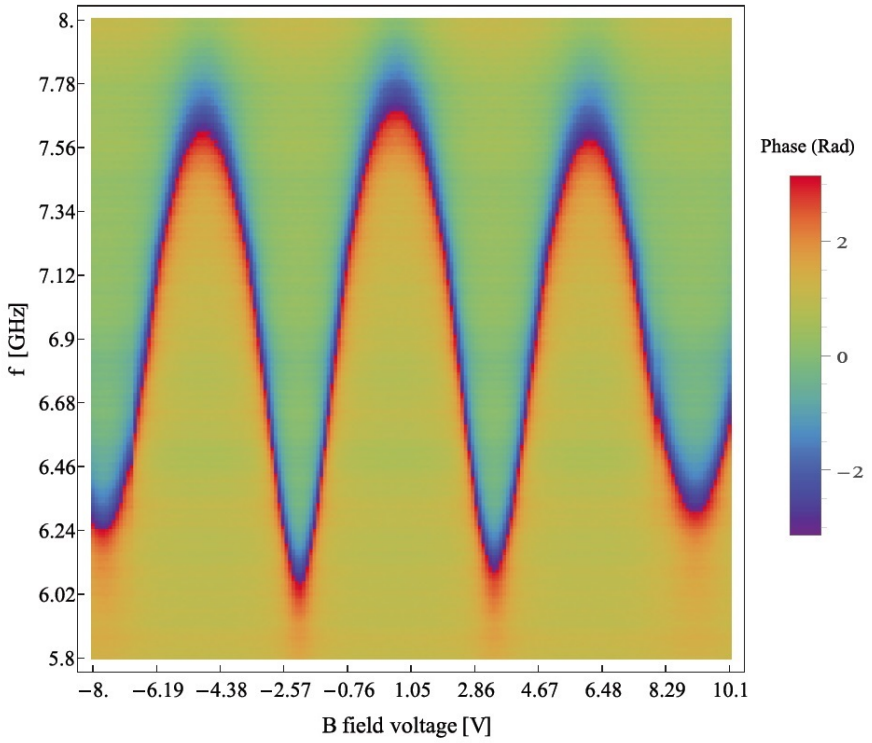

FIGURE 7.12: Reflected phase of resonator JPM12 1 as a function of the applied frequency and the voltage in the magnetic coil.

By fitting each of the slices at a particular B field coil voltage we have obtained the resonance frequency as a function of the magnetic field, as shown in figure 7.13. By fitting this dependence for four different resonators we are able to obtain the values presented in table 7.12. We also show the approximated value of the Josephson energy obtained from room temperature measurements of the resistance of the junctions. From the results of the table we can deduce that the fabrication uncertainty of E_J is close to 6 %. Fabrication uncertainty on a single chip is of a similar value.

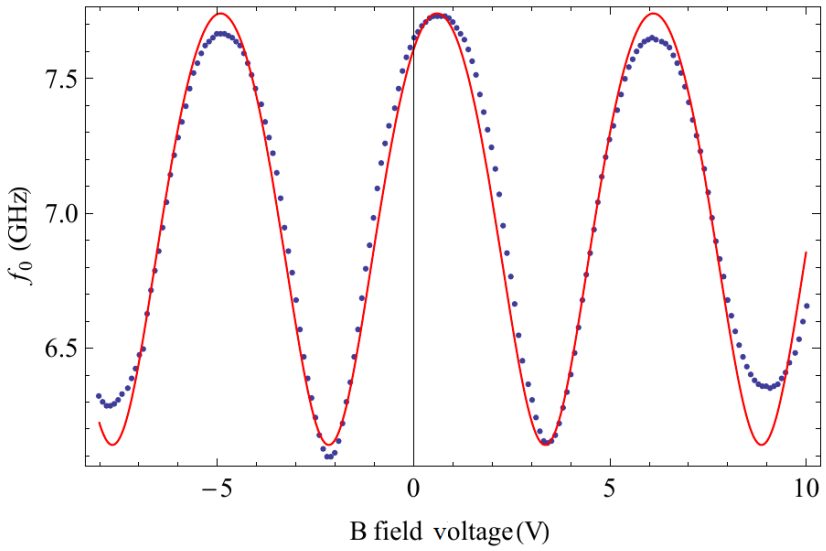

FIGURE 7.13: Resonance frequency as a function of the applied magnetic field for resonator JPM12 1 and corresponding fit.

JPM	$f_{\min}$ - $f_{\max}$**(GHz)**	$L_{\min}$ - $L_{\max}$**(nH)**	E_J**(THz)**	E'_J**(THz)**
12_1	6.12(1) - 7.74(1)	2.02(1) - 3.20(1)	3.23(3)	3.29(3)
12_2	6.13(1) - 7.52(1)	2.14(1) - 3.19(1)	2.99(3)	3.29(3)
22_1	6.55(1) - 7.99(1)	1.90(1) - 2.80(1)	3.50(3)	3.64(3)
22_2	6.42(5) - 7.86(5)	1.93(3) - 2.92(5)	3.43(7)	3.64(3)

TABLE 7.12: Parameters of the SQUID arrays obtained by fitting the frequency dependence on the applied magnetic field. The inductance values have been obtained using the design model from table 7.7, and E_J using equation 5.7 and L_{max}, taking into account the island inductance contribution of 0.5 nH. E'_J denotes the value measured from the resistance of the array at room temperature [31].

To measure the gain of a nonlinear resonator operated as a degenerate JPA, we apply a strong signal at a fixed frequency (pump) and measure the reflection of a weak signal detuned by 5 kHz with respect to the pump. By measuring this reflected signal with the power of the pump on and off, we can obtain the gain of the signal. By sweeping the B field and the applied pump power, we can obtain the phase diagram, which is displayed in figure 7.13, and shows a similar behaviour as the one obtained by simulation in figure 5.4. The additional gain region present at high power is probably due to bistability, which was not taken into account in the plotted simulated diagram.

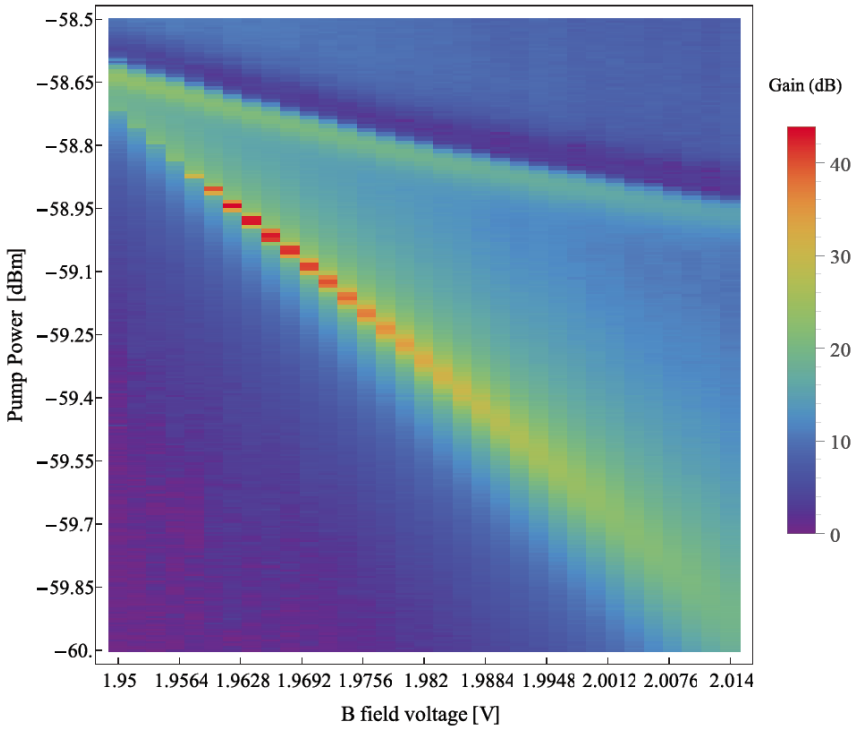

FIGURE 7.14: Phase diagram of gain in a JPA as a function of the pump power and B field coil voltage, which is equivalent to sweeping signal frequency. The applied pump power has been calculated assuming a cabling attenuation of 65 dB.)

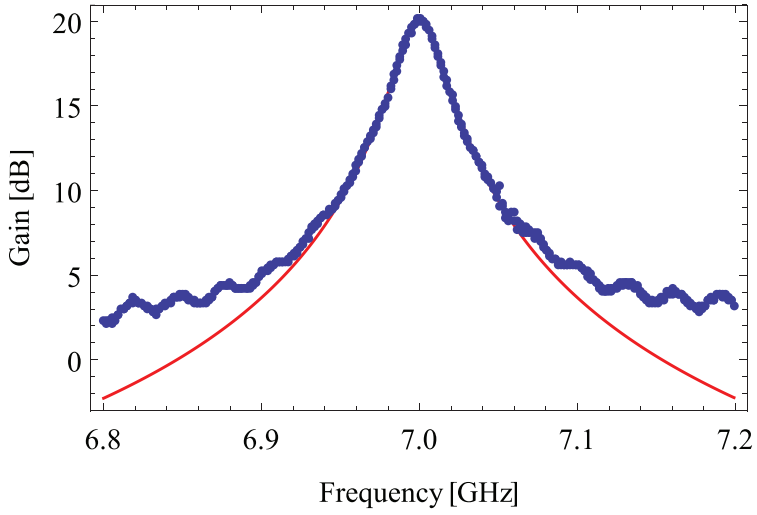

FIGURE 7.15: Plot of the measured signal gain as a function of the signal frequency with fixed pump power and frequency. The red line indicates a Lorentzian fit to the gain.

Figure 7.15 has been obtained by choosing a point of the phase diagram with a moderate gain (close to 20 dB) and using the corresponding B field voltage and pump power parameters, while sweeping the frequency of the applied signal. The

obtained gain can be fitted to a Lorentzian, as showed by the red curve. The parameters obtained from fit are a gain-bandwidth product of 315 MHz, a central frequency of 7 GHz and a maximum gain of 19.96 dB.

7.5 Josephson Parametric Trimer

In this section the results of the measurements of the trimer sample JPT4 3 are described. The design details of this sample are displayed in table 7.13. The phase measurement in reflection as a function of the applied frequency and B field voltage are shown in figure 7.16, where the tunability of the three eigenfrequencies can be observed. The effect of inhomogeneities can be seen at higher voltages, and it is a consequence of an asymmetry of the bare resonance frequencies due to an asymmetric coupling to the magnetic flux. The source of the inhomogeneity comes from the magnetic field not being perfectly uniform and from SQUID fabrication inhomogeneities.

	Finger number				**SQUID arrays**	
	C_κ	**SC1**	**SC2**	**SC3**	**C_J**	**Num. of SQUIDs**	**Asymmetry**
JPT 4	12	12	15	18	5	30	1 / 3

TABLE 7.13: Design parameters of the sample JPT4. SC refers to Shunt Capacitor, where SC1 is the one closest to the external coupling capacitor. C_J is the coupling capacitor between the resonators.

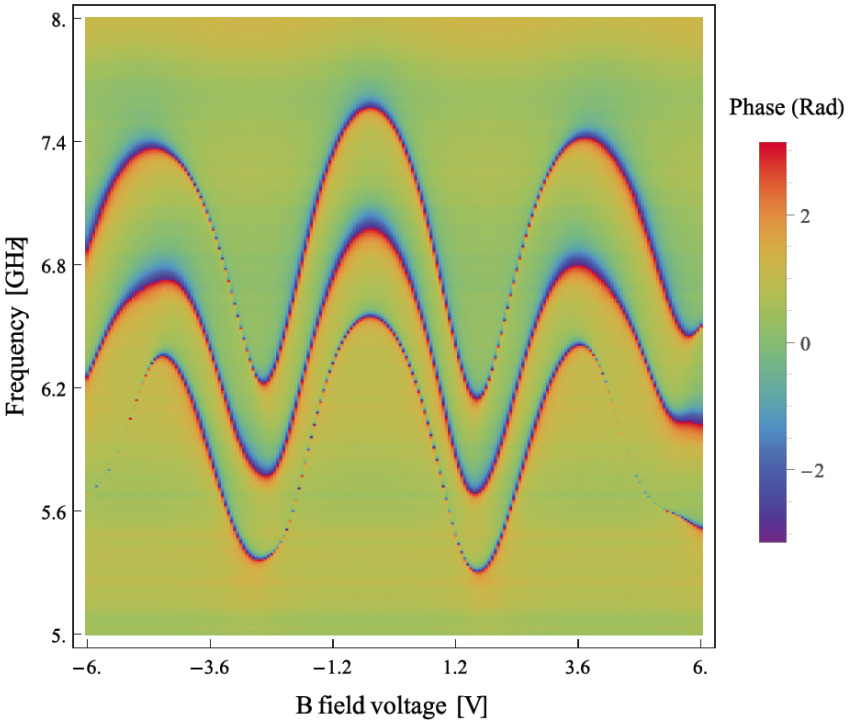

FIGURE 7.16: Reflected phase of trimer JPT4 as a function of the applied frequency and the voltage in the magnetic coil.

Degenerate and non-degenerate amplification has been studied for different regimes in the trimer. To compare with the plots of the simulations shown in chapter 5, degenerate and non-degenerate phase diagrams have been measured by sweeping the frequency and power of the pump. In the degenerate case, the signal frequency was fixed at a detuning of 5 kHz to the pump, and the measured gain phase diagram is shown in figure 7.17. The B field was fixed at the point which yielded maximum eigenfrequencies in figure 7.16, close to zero voltage, since it behaves as a *sweet spot* and offers weak flux noise dependence. The degenerate phase diagram shows gain at three different frequency regions, corresponding to these three eigenfrequencies. Those will get redshifted as the power is increased, in the same way as it was described for the theoretical study.

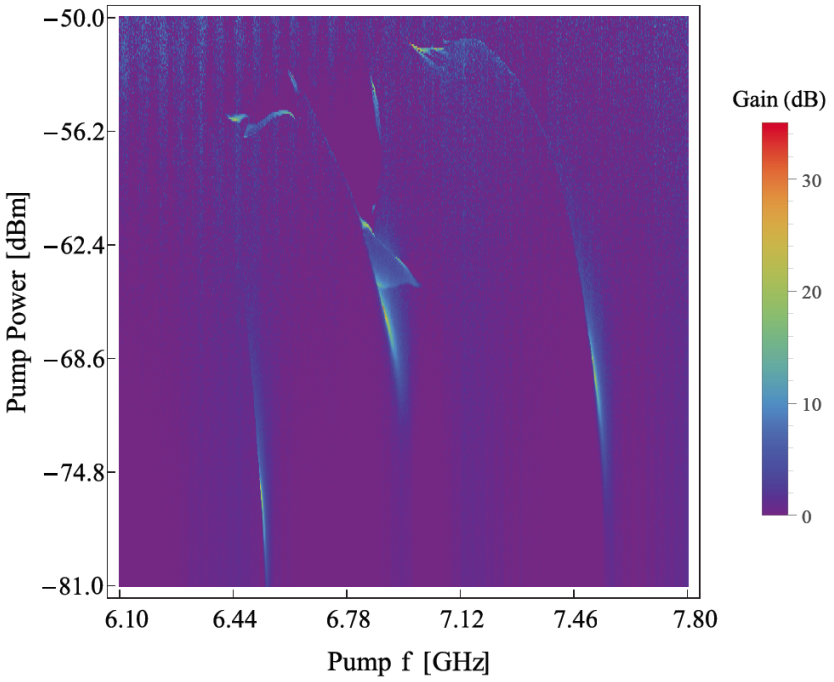

FIGURE 7.17: Phase diagram of the degenerate gain in a JPT as a function of the pump power and pump frequency. The applied pump power has been calculated with a cabling attenuation of 65 dB.

To measure the non-degenerate phase diagram it is important to optimize the detuning between the pump and the signal, since a single gain point is measured for each configuration of pump frequency and power. To do so, we first fixed the pump at a moderate power and then swept the pump frequency around the central eigenfrequency and the signal frequency around one of the two other eigenfrequencies (the higher one in this case). After doing so we perform a linear regression between the two frequencies such that it maximizes the gain. This linear relation between the signal and the pump can be fixed during the measurement, allowing to measure a two-dimensional phase diagram by changing the pump frequency and power. The results are shown in figure 7.18.

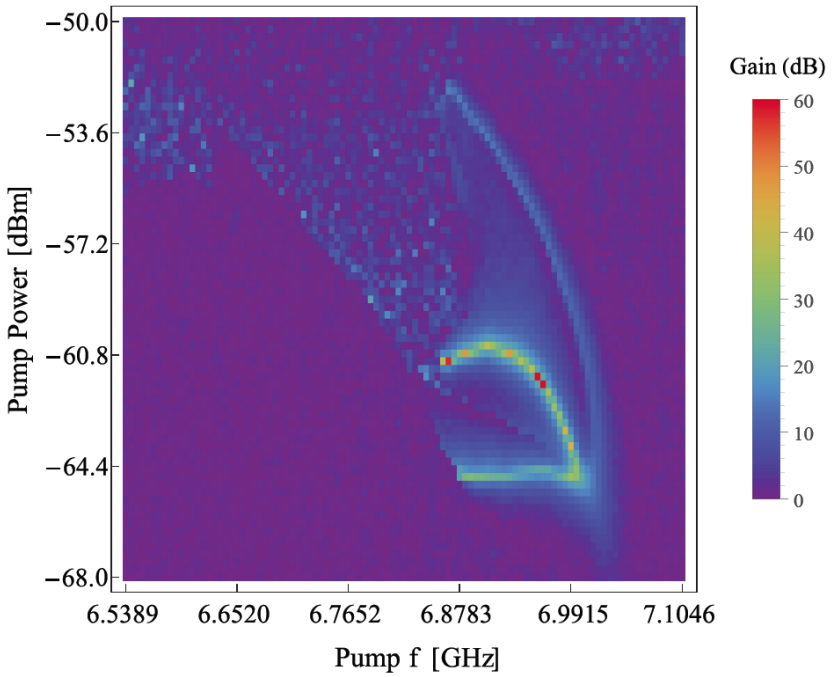

FIGURE 7.18: Phase diagram of the non-degenerate gain in a JPT as a function of the pump power and frequency. Pump and signal frequencies obey the relation $f_P = 1.13 f_S - 1.494$ GHz, obtained from a previous measurement. The applied pump power has been calculated with a cabling attenuation of 65 dB.

By selecting the points with high gains from the phase diagram, we can measure degenerate and non-degenerate gain spectra where we only sweep the applied signal frequency. As discussed in chapter 5, since most of these gains are essentially analogous to the ones that can be measured with a JPD [9], we focus here only in showing the gain obtained by applying the pump close to the central eigenfrequency. There the gain will be both degenerate and non-degenerate. Three different regimes are explored by sweeping the pump power and keeping the pump frequency constant in figures 7.19, 7.20, 7.21. We note good agreement with the simulations presented in chapter 5.

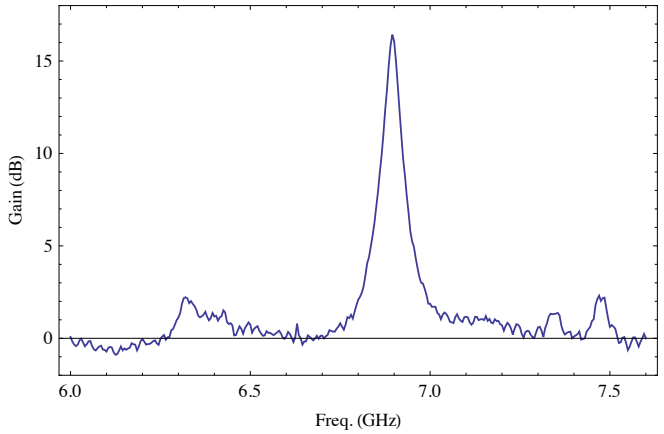

FIGURE 7.19: Measured gain as a function of the signal frequency for a regime close to the purely degenerate amplification of the central eigenfrequency. The pump is applied at a frequency of 6.9 GHz and at a power of -66 dBm.

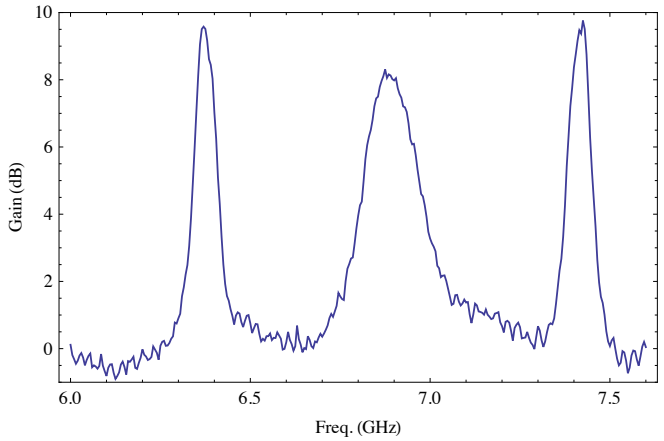

FIGURE 7.20: Measured gain as a function of the signal frequency for a regime where both degenerate and non-degenerate amplification are equally strong. The pump is applied at a frequency of 6.9 GHz and at a power of -65.1 dBm.

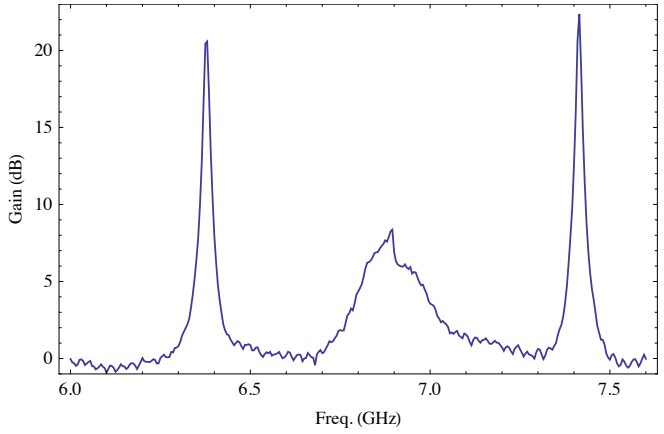

FIGURE 7.21: Measured gain as a function of the signal frequency for a regime close to the purely non-degenerate amplification of the high and low eigenfrequencies. The pump is applied at a frequency of 6.9 GHz and at a power of -64.8 dBm.

Chapter 8

Conclusions

In the present work we have described the design and experimental characterization of both individual resonators and one-dimensional arrays of several coupled resonators. Nonlinear samples have also been realized, whose frequency tunability was studied and which were used as Josephson parametric amplifiers.

The results obtained from the high-frequency finite element simulation of our structures indicate that the operation frequencies are well below (around seven times) the self-resonant frequencies of each of the individual elements, allowing to model the whole system as a lumped-element LC circuit with reactive parameters renormalized by their parasitic contributions. A method for the extraction of the circuit parameters has been described and experimentally realised, which allowed us to generate a design model for our resonators, whose predictions for the resonance frequency have been compared to the measured values showing an agreement within 1 %. This model can now be used to design future samples with desired Hamiltonian parameters.

The reproducibility of the resonators has been studied for both the linear and the nonlinear terms. In the case of linear resonators, several resonators identical in design have been fabricated and their resonance frequencies measured, indicating a fabrication uncertainty of 20 MHz and an asymmetry between samples fabricated horizontally or vertically in our chips. If this asymmetry is taken into account, it leads to a value of 10 MHz fabrication uncertainty. For the case of nonlinear resonators, the parameters of the fabricated SQUID arrays have been extracted from four nonlinear resonators by measuring the tunability of their resonance frequencies and using the predictions of the design model. Our measurements show that SQUID arrays can be fabricated within 6 % uncertainty. With our effective model we have successfully fabricated three coupled resonators with the desirable properties.

The use of nonlinear resonators for the realization of parametric amplification has also been studied for the cases of an individual resonator and of an array of three coupled resonators, the Josephson Parametric Trimer. Both results show

qualitative agreement with the theoretical predictions. With the trimer sample it has been possible to perform both degenerate and nondegenerate parametric amplification. This could improve the JPA performance, which could be switched between the two operational modes by only modifying the applied power.

8.1 Outlook

The results from the measurement and the theoretical predictions obtained from input-output theory for the JPT indicate that the amplification bandwidth of JPTs could be improved by reducing the capacitive coupling between the resonators, which would merge the bandwidths of the three eigenfrequencies together, and which by increasing the number of coupled resonators would allow the realization of a broadband parametric amplifier.

The fabrication process has to be improved in order to decrease the shift between horizontal and vertical resonators. This will be especially important for future experiments with periodic boundary conditions, as circular resonators arrays.

Regarding the use of the described arrays of nonlinear resonators as analogue quantum simulators, an important step towards the control of the Hamiltonian parameters will be the design of arrays with tunable coupling between the resonators, which can be achieved by using SQUIDs as coupling capacitors. Such a progress would be essential for the study of quantum phase transitions with superconducting circuits.

Acknowledgements

The realization of this thesis could not have been possible without the help provided by many people during these last six months. First of all I would like to thank professor Andreas Wallraff, who offered me the chance of working in the Quantum Device Lab on such a motivating project for my master thesis.

I want to thank especially the two members of the "Lumped Element Team" (LE Team), Anton and Michele. Anton supervised my work and advised me whenever I needed it in the course of this work. I have learned most of what I know of experimental physics thanks to him, but I am also grateful to him for his lessons of skiing, bouldering and skating, without which I could not have survived the hard Swiss winter. To Michele I owe for all his tips and experience, which saved the day in a lot of experimental situations, and also for the enjoyable evenings we spent in the lab cooking *Chäschüechli* or discussing the endless applications of the cute piece of software TinyTake.

I also want to acknowledge other members of the lab whose work has been essential for this thesis. I thank Mintu for his work in the photolithography and the dicing of our masks and Markus for the tips in the design of the SQUIDs and the actual writing of the arrays in the clean room. Philipp was of great help when measuring gain for the first time, and together with Theo his assistance when cabling and measuring in Blufors was really appreciated. In the setup of Vericold I owe all help to Marek, who made it straightforward to measure our samples.

I of course would like to thank the whole Quantum Device Lab for the nice time I spent in the last six months, not only in the lab but also in other activities as skiing, jogging or football playing. Outside of the lab I also want to thank the great friends I have met in Zurich, and which helped me from time to time to disconnect and forget about the thesis work.

Last I would like to acknowledge the support I received from Barcelona. By far the two most important people to who I owe for this Helvetic experience are my parents, who always encouraged me to go abroad and offered me the means. I want to thank with a lot of affection Anna, Leo and Júlia, whose adventures made my working days lighter and who reminded me when it had been too long without visiting my family. Last I want to acknowledge "Fundació La Caixa" for

believing in my project and granting me the economical support I needed for the whole Master studies.

Appendix A

The fitting procedure

Once the scattering matrix coefficients have been measured, either by the VNA or by an FPGA measuring setup, it is exported to be read with a Mathematica notebook to proceed to the fitting of the reflection coefficient [41]. In this appendix we describe the procedure done in this notebook and its different parts.

A.1 Circle fit

Once the values of the reflection coefficients are imported, the data is represented on a polar plot and it is fitted to a circumference, obtaining the values of the center and the radius. By taking the real part of the reflection as x and the imaginary as y, we are able to fit the expression of a circumference

$$(x - x_0)^2 + (y - y_0)^2 = R^2. \tag{A.1}$$

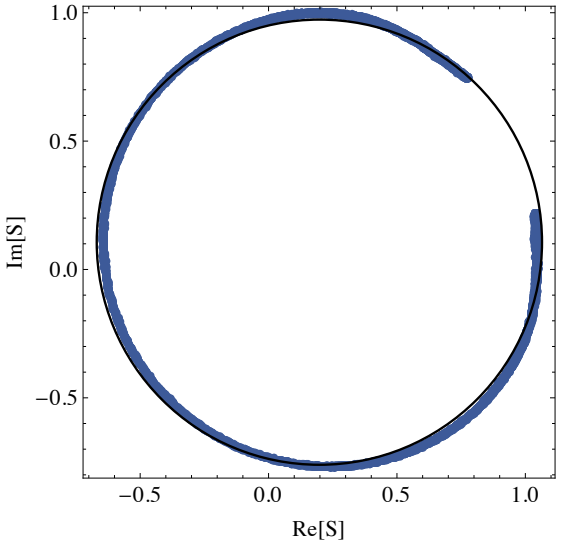

FIGURE A.1: Polar plot of the reflection data together with the circumference fit.

A.2 Phase fit

Using the data from the circle fit, the data is translated so that the center is on the origin of coordinates, and it is also rotated so that the points far from the resonance have zero phase, therefore already obtaining a first estimation of the phase shift of the measured data. Next, the phase of each of the points is obtained and it is plotted as a function of frequency. This data is fitted to obtain the frequency of the resonance and the loaded quality factor. The used expression is

$$\phi(\nu) = \phi_0 + \tau\nu + 2\arctan\left(2\,Q_L\left[1 - \frac{\nu}{\nu_0}\right]\right), \tag{A.2}$$

where ν_0 is the resonance frequency, Q_L the loaded quality factor, τ the phase delay and ϕ_0 a phase shift.

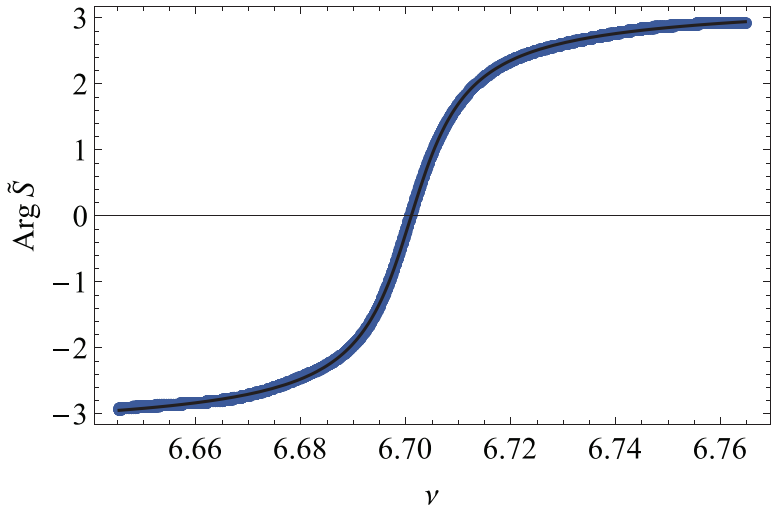

FIGURE A.2: Plot of the phase after the translation and corresponding fit.

Once the loaded quality factor and the frequency has been obtained, it is possible to obtain the coupling rate κ and the loss rate γ by using the fitted radius from the circle fit to determine the proportion between the internal and external quality factor. However, due to the fact that the calibration is done at room temperature but the measurements are at cryogenic temperatures, the data measured is not properly normalized and it might also have additional reflections, which means that the obtained values for the coupling and loss rate might not be accurate.

A.3 Complex Lorentzian fit

In many situations the loaded quality factor and the resonance frequency are enough to characterize the measured resonator. However, in many cases it will be

necessary to also fit the complex reflection coefficient obtained from input-output theory, as they can be used to extract the coupling and loss rates, and in the case of samples with coupled resonators. Because of the non-cryogenic calibration, in this fit we will also take into account a normalization of the whole expression that is caused by the VNA calibration and in some cases also the offset term. Results of the fit of a particular resonator are shown in figure A.3.

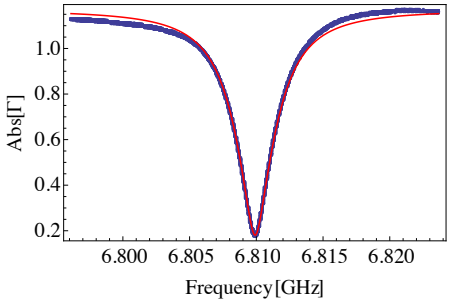

(A) Data and fit of the absolute part.

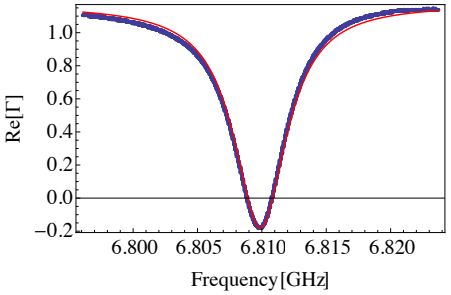

(B) Data and fit of the real part.

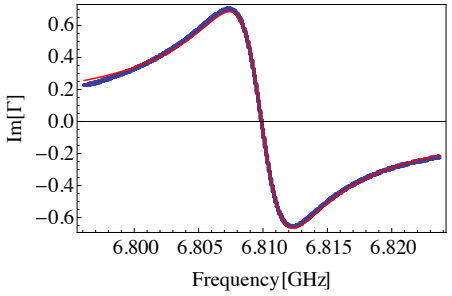

(C) Data and fit of the imaginary part.

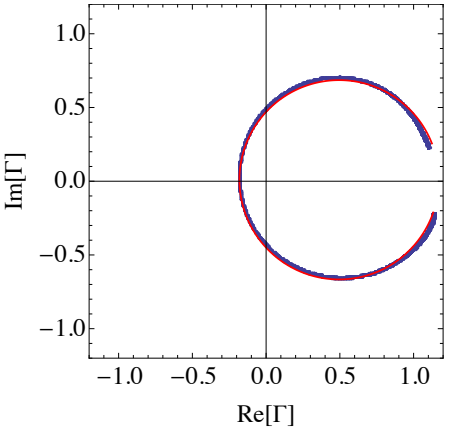

(D) Polar plot of the data and fit.

FIGURE A.3: Results of the Lorentzian fit, showing the absolute, real, imaginary and polar plots.

Appendix B

Characterization of linear resonators

The first mask measured was mask 36, whose main objective was to characterize the different component contributions in linear resonators. This characterization includes an estimation of the dependence of the circuit parameters on the design, exploring the regimes of strong and weak external coupling, study the quality factor at mK temperatures and estimating the effects of kinetic inductance.

B.1 Parameter sweeping

Studies SC0, SI0 and CC0 were devoted to sweeping the shunt capacitance, shunt inductance and coupling capacitance respectively. By plotting the squared inverse of the measured frequencies we can infer a linear dependence of the circuit parameters on the design parameters for the three studies, as seen in figures B.1, B.2, B.3.

The design parameters of the island between the inductor and the capacitor have also been swept to analyse their contribution. In figure B.4 we show the approximated island inductance as a function of the total length of the island. This approximated value was obtained by extracting the total inductance from the measured resonance frequency and the expected total capacitance and removing the estimated contribution from the inductor. Even though the contribution of the island is probably overestimated, the linear behaviour can be appreciated.

By using values of the capacitance obtained from dc Maxwell simulations and the measured frequencies a design model like the one in 7.3 has also been obtained. The model parameters are shown in B.1.

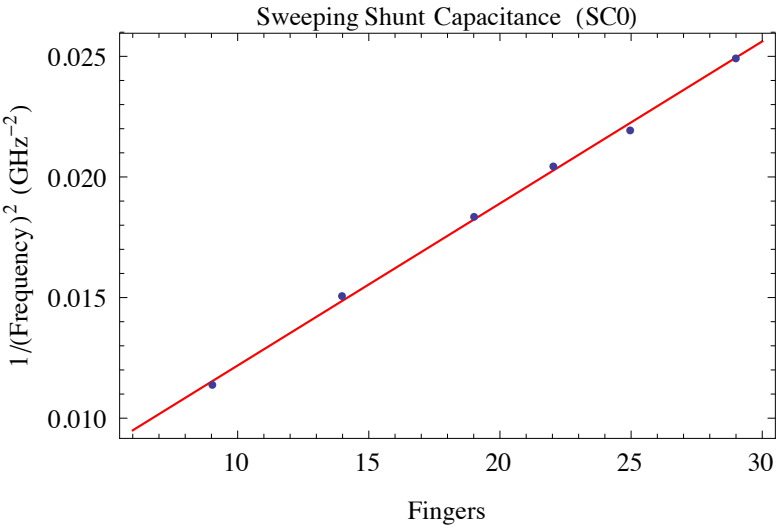

FIGURE B.1: Plot of the inverted square of the measured frequencies of SC0 as a function of the sweeping parameter, the number of shunt capacitor fingers. The red curve is a linear fit of the measured points.

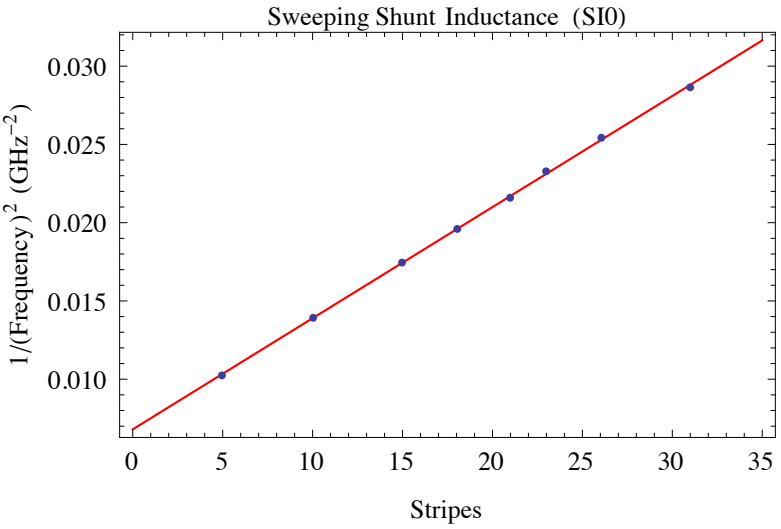

FIGURE B.2: Plot of the inverted square of the measured frequencies of SI0 as a function of the sweeping parameter, the number of shunt capacitor fingers. The red curve is a linear fit of the measured points.

	a	**b**
SC	10.5 fF	70) fF
SI	0.05 nH	0.5 nH
CC	5 fF	3 fF

TABLE B.1: Coefficients of the design model obtained from a linear fit of the extracted parameters for the shunt capacitor (SC), shunt inductor (SI) and coupling capacitor (CC) studies.

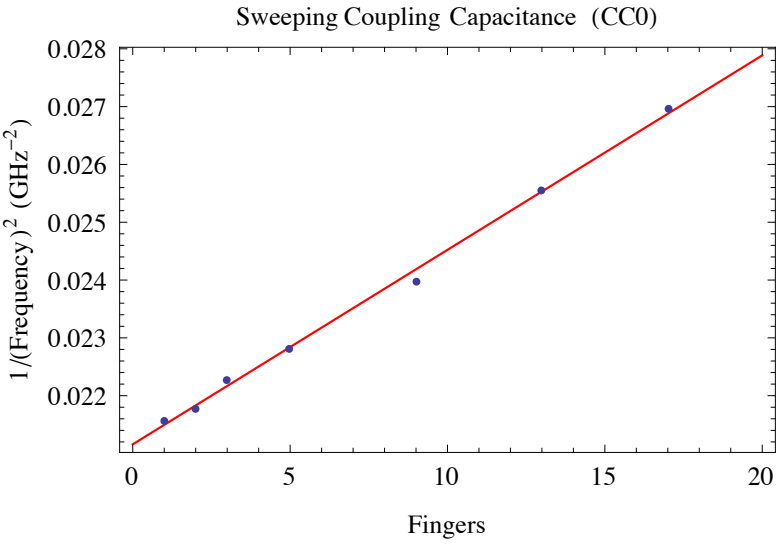

FIGURE B.3: Plot of the inverted square of the measured frequencies of CC0 as a function of the sweeping parameter, the number of shunt capacitor fingers. The red curve is a linear fit of the measured points.

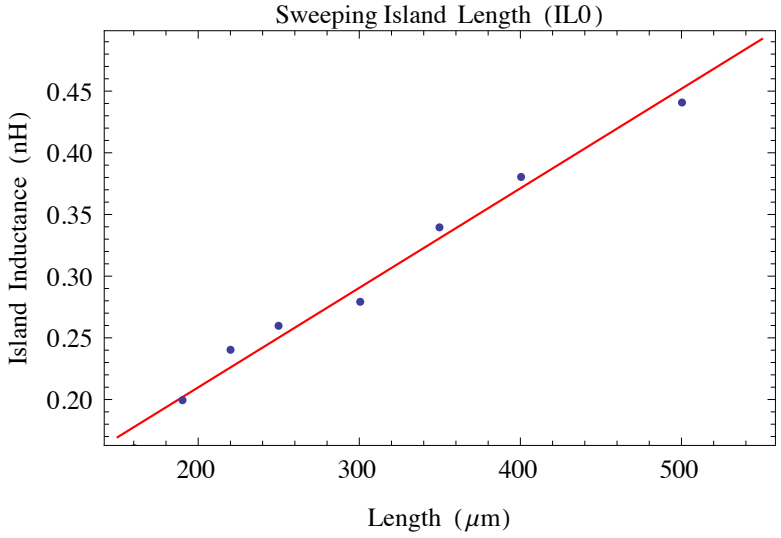

FIGURE B.4: Plot of the extracted island inductance as a function of the island length. The inductance has been extracted from measurements by using capacitance simulations and approximating the meander inductance as $L = 1.47$ nH.

B.2 Varying coupling capacitance

Samples CC0 and CCS0 of mask 36 were dedicated to the analysis of the resonance frequencies and the quality factors of samples with extremely different couplings. The quality factor for the resonators in these studies as a function of the simulated coupling capacitance is shown in figure B.5.

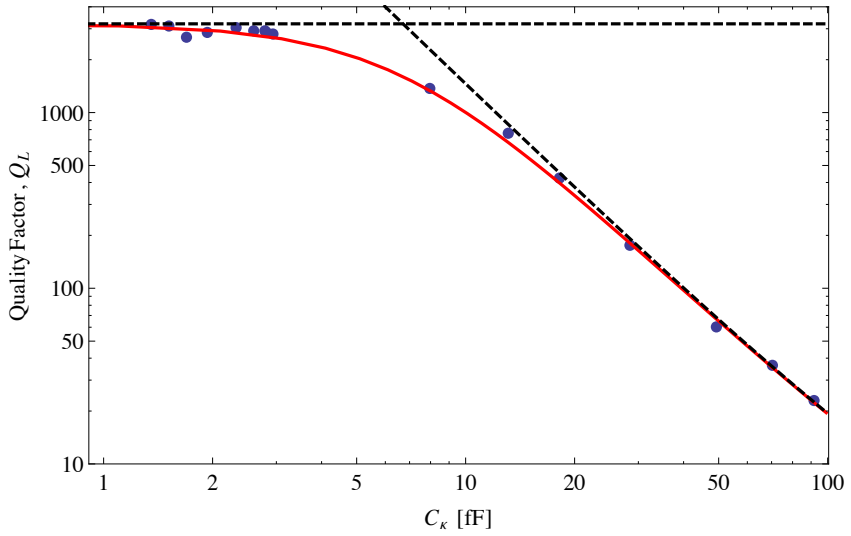

FIGURE B.5: Graphic showing the loaded quality factor as a function of the simulated coupling capacitance for 15 resonators with designed big (CC0) and small (CCS0) coupling capacitances. The red curve is given by the prediction of Q_L given by the RLC model of chapter 4. The dashed lines indicate the expected Q_L for the two limiting cases of small and strong coupling.

From figure B.5 we can conclude that the internal quality factor at 4.2 K is around 3000. By using the value of the resonance frequency we can estimate the internal resistor (losses) to have a value of 225000 Ω.

B.3 Low-temperature measurements

All the results shown in the previous two subsections were obtained by measuring superconducting resonators at a temperature of 4.2 K by using a dipstick inside a helium dewar. Since the experiments involving SQUIDs will require dilution fridge temperatures, it is important to estimate how the losses in our resonators behave at such temperatures. To do so, the sample CCS0 8, which has the smallest coupling of mask 36, was measured at temperatures close to 17 mK in a Blufors dilution refrigerator. The resonance frequency was found at 6.9 GHz, slightly higher than the value of 6.83 GHz measured at helium temperatures, which is expected due to smaller kinetic inductance. The high quality factors allow to determine the resonance frequency very precisely, and in figure B.6 we plot its value as a function of the applied power. It can be observed that it decreases monotonously as we increase the power. The reason for such a behaviour could be an increase in kinetic inductance due to a reduction of the cooper pair density, but it could also be associated to other kinds of nonlinearities.

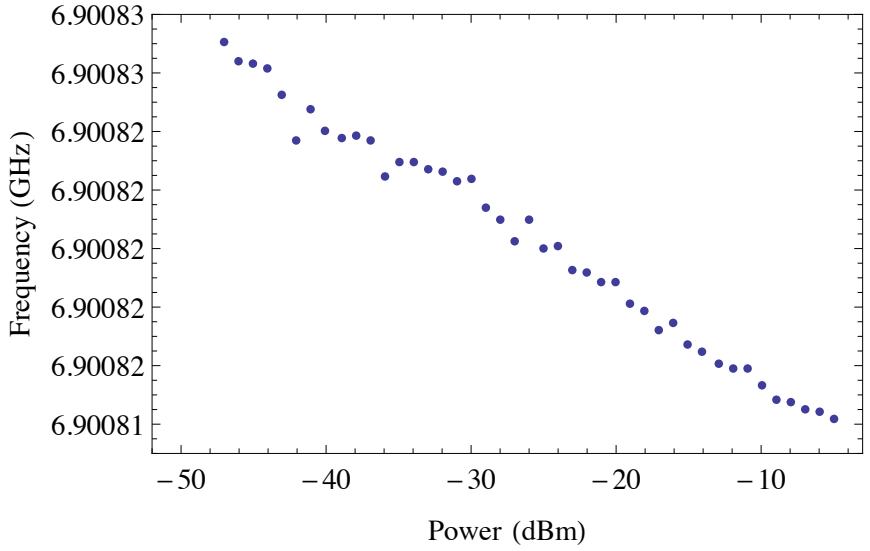

FIGURE B.6: Graphic showing the dependence of the resonance frequency on the input power.

The measurement of the quality factor showed an increase with increasing input powers, as seen in figure B.8. The Lorentzian fit of the resonances indicates that the external quality factor keeps essentially constant for the measured powers, at a value of $Q_{ext} \approx 77900$, and that it is the internal quality factor which increases. This has also been observed in weakly coupled coplanar waveguide resonators, and can be explained by the dependence of dielectric losses on the number of photons in the cavity for low drive powers [31]. However no saturation of the quality factor was observed for high powers, which suggests that the quality factor could reach even higher values for strong drives.

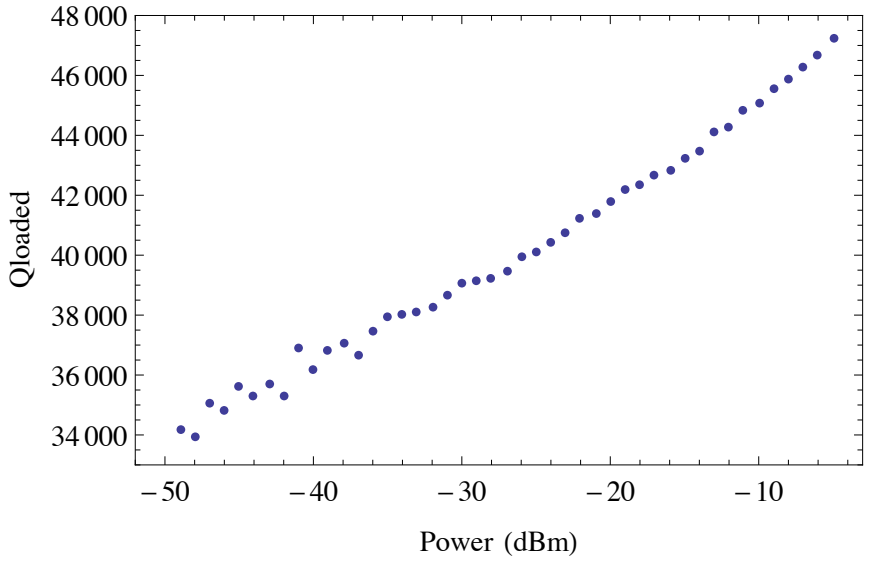

FIGURE B.7: Graphic showing the dependence of the loaded quality factor on the applied input power. As the power increases the quality factor improves.

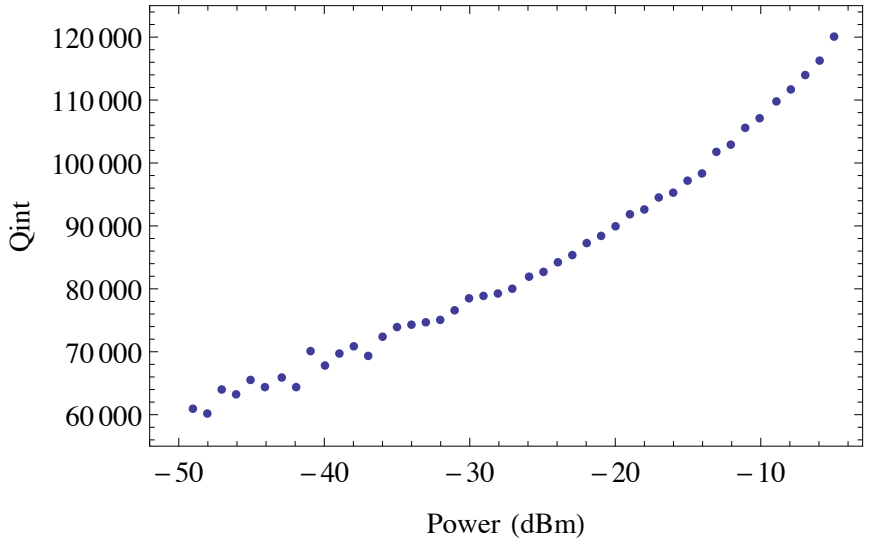

FIGURE B.8: Graphic showing the fitted internal quality factor of the resonator as a function of the applied power. The power dependence of the dielectric losses is the reason for such rise.

B.4 Kinetic Inductance

As discussed in chapter 3, the inductance in a superconducting resonator will also have a contribution from kinetic inductance, which will depend on the temperature of the superconductor as expressed by equation 3.1. By using the pulse-tube cooler based cryostat ARCTIC, which setup details can be found in [42], we have been able to measure the resonance frequency of our resonators at different controlled temperatures. The measured frequencies as a function of temperature have been fitted to extract the kinetic inductance and the critical temperature. To do so, simulated values of the resonator capacitance have been used to fix the total capacitance constant, while T_c and each of the inductance contributions have been fitted by the expression given by [18]

$$f_0(T) = \frac{1}{2\pi\sqrt{C(L_G + L_K(0)/(1 - T/T_c))}}. \tag{B.1}$$

The fit to the measured data is shown in figure B.9. The extracted values from the fit are $L_G = 1.87$ nH, $L_K(0) = 0.04$ nH and $T_c = 8.97$ K. By using these values we have extrapolated the kinetic inductance contribution at different temperatures, which can be seen in figure B.10. We note that the values are less reliable below 4 K, since the approximate function is derived only for temperatures close to T_C. Nevertheless we can estimate the kinetic inductance at 4.2 K to be 0.06 nH, which is around 3 % of the geometric inductance value.

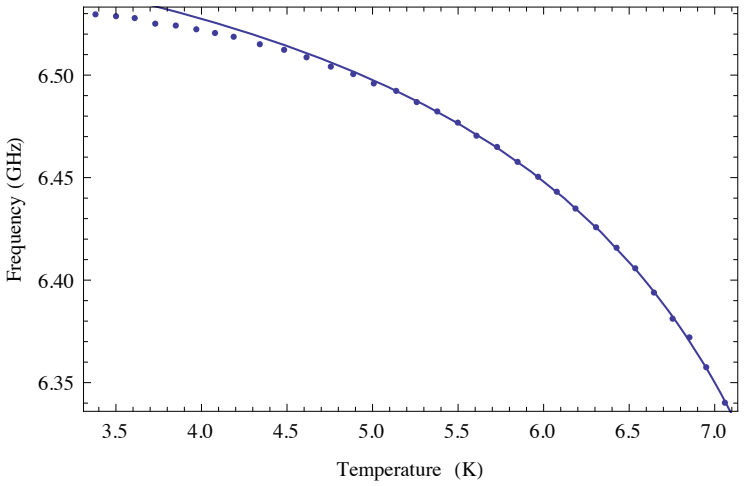

FIGURE B.9: Plot of the resonance frequency of a superconducting resonator as a function of the cryostat temperature. The blue line indicates a fit to B.1.

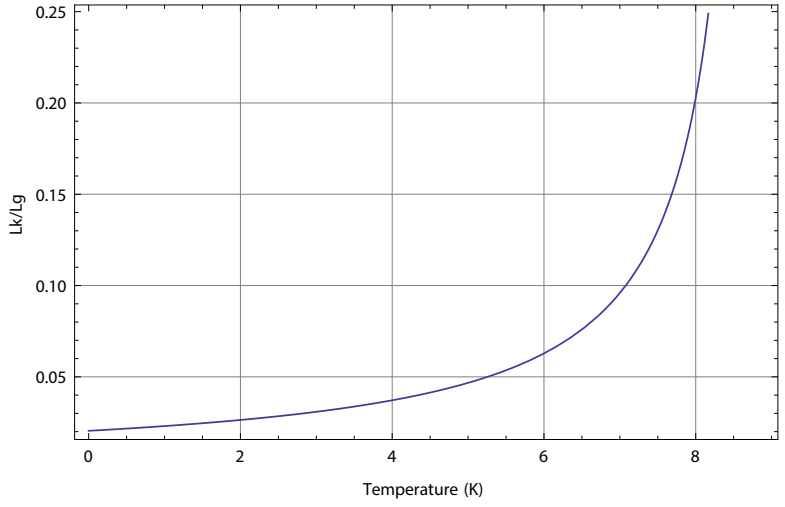

FIGURE B.10: Plot of the estimated ratio between kinetic and geometric inductance for all temperatures at which niobium is superconductor. This estimation is only accurate close to the critical temperature.

Bibliography

[1] Iulia Buluta and Franco Nori. Quantum simulators. *Science.* **326**,(5949), 108–111, 2009. doi: 10.1126/science.1177838. URL http://www.sciencemag.org/cgi/content/abstract/326/5949/108.

[2] R Miller, T E Northup, K M Birnbaum, A Boca, A D Boozer, and H J Kimble. Trapped atoms in cavity QED: coupling quantized light and matter. *J. Phys. B: At., Mol. Opt. Phys.* **38**,(9), S551, 2005. URL http://stacks.iop.org/0953-4075/38/i=9/a=007.

[3] Ferdinand Brennecke, Tobias Donner, Stephan Ritter, Thomas Bourdel, Michael Kohl, and Tilman Esslinger. Cavity QED with a Bose-Einstein condensate. *Nature.* **450**,(7167), 268–271, November 2007. ISSN 0028-0836. URL http://dx.doi.org/10.1038/nature06120.

[4] A. Blais, R.-S. Huang, A. Wallraff, S. M. Girvin, and R. J. Schoelkopf. Cavity quantum electrodynamics for superconducting electrical circuits: An architecture for quantum computation. *Phys. Rev. A.* **69**, 062320, 2004.

[5] M.J. Hartmann, F.G.S.L. Brandao, and M.B. Plenio. Quantum many-body phenomena in coupled cavity arrays. *Laser & Photon. Rev.* **2**,(6), 527–556, 2008. ISSN 1863-8899. URL http://dx.doi.org/10.1002/lpor.200810046.

[6] Andrew D. Greentree, Charles Tahan, Jared H. Cole, and Lloyd C. L. Hollenberg. Quantum phase transitions of light. *Nat. Phys.* **2**,(12), 856–861, December 2006. ISSN 1745-2473. URL http://dx.doi.org/10.1038/nphys466.

[7] Dimitris G. Angelakis, Marcelo Franca Santos, and Sougato Bose. Photon-blockade-induced mott transitions and xy spin models in coupled cavity arrays. *Phys. Rev. A.* **76**,(3), 031805–, September 2007. doi: 10.1103/PhysRevA.76.031805. URL http://link.aps.org/doi/10.1103/PhysRevA.76.031805.

[8] A. Tomadin, V. Giovannetti, R. Fazio, D. Gerace, I. Carusotto, H. E. Türeci, and Ataç İmamoğlu. Signatures of the superfluid-insulator phase transition in laser-driven dissipative nonlinear cavity arrays. *Phys. Rev. A.* **81**,(6), 061801, Jun 2010. doi: 10.1103/PhysRevA.81.061801.

[9] C. Eichler, Y. Salathe, J. Mlynek, S. Schmidt, and A. Wallraff. Quantum limited amplification and entanglement in coupled nonlinear resonators. *arXiv:1404.4643.* 2014. URL http://arxiv.org/abs/1404.4643.

[10] M. Hatridge, S. Shankar, M. Mirrahimi, F. Schackert, K. Geerlings, T. Brecht, K. M. Sliwa, B. Abdo, L. Frunzio, S. M. Girvin, R. J. Schoelkopf, and M. H. Devoret. Quantum back-action of an individual variable-strength measurement. *Science.* **339**,(6116), 178–181, 2013. doi: 10.1126/science.1226897. URL http://www.sciencemag.org/content/339/6116/178.abstract.

[11] C. Eichler, D. Bozyigit, C. Lang, L. Steffen, J. Fink, and A. Wallraff. Experimental state tomography of itinerant single microwave photons. *Phys. Rev. Lett.* **106**,(22), 220503–4, Jun 2011. doi: 10.1103/PhysRevLett.106.220503. URL http://prl.aps.org/abstract/PRL/v106/i22/e220503.

[12] G. de Lange, D. Riste, M. J. Tiggelman, C. Eichler, L. Tornberg, G. Johansson, A. Wallraff, R. N. Schouten, and L. DiCarlo. Reversing quantum trajectories with analog feedback. *Phys. Rev. Lett.* **112**,(8), 080501–, February 2014. URL http://link.aps.org/doi/10.1103/PhysRevLett.112.080501.

[13] M. A. Castellanos-Beltran and K. W. Lehnert. Widely tunable parametric amplifier based on a superconducting quantum interference device array resonator. *Appl. Phys. Lett.* **91**,(8), 083509–3, August 2007. URL http://link.aip.org/link/?APL/91/083509/1.

[14] J. Mutus, T. White, R. Barends, Y. Chen, Z. Chen, B. Chiaro, A. Dunsworth, E. Jeffrey, J. Kelly, A. Megrant, C. Neill, P. O Malley, P. Roushan, D. Sank, A. Vainsencher, J. Wenner, K. Sundqvist, A. Cleland, and J. Martinis. Strong environmental coupling in a josephson parametric amplifier. *arXiv:1401.3799.* 2014. URL http://arxiv.org/abs/1401.3799.

[15] David M. Pozar. *Microwave engineering.* John Wiley & Sons, Inc., 4th ed. edition, 2011.

[16] I. Bahl. *Lumped Elements for RF and Microwave Circuits.* Artech House, 2003.

[17] M. Damjanovic G. Stojanovic, L. Zivanov. Compact form of expressions for inductance calculation of meander inductors. *Serbian Journal of Electrical Engineering.* 2004.

[18] A. J. Annunziata, D. F Santavicca, L. Frunzio, G. Catelani, M.J. Rooks, Frydman A., and D. E. Prober. Tunable superconducting nanoinductors. *Nanotechnology.* **21**,(445202), 2010.

[19] Christopher Eichler. *Experimental Characterization of Quantum Microwave Radiation and its Entanglement with a Superconducting Qubit.* PhD thesis, ETH Zurich, 2013. URL http://qudev.phys.ethz.ch/content/science/Documents/phd/PhD_Eichler.pdf.

[20] S M Girvin. Superconducting qubits and circuits: Artificial atoms coupled to microwave photons. 7 2011. Lectures delivered at Ecole d'Eté Les Houches; To be published by Oxford University Press.

[21] Felix Winterer. Characterization of the linear response and the tunability of two coupled lc oscillators. Master's thesis, Laboratory of solid state physics, ETH Zurich, 09 2013.

[22] A. A. Clerk, M. H. Devoret, S. M. Girvin, Florian Marquardt, and R. J. Schoelkopf. Introduction to quantum noise, measurement, and amplification. *Rev. Mod. Phys.* **82**,(2), 1155–1208, Apr 2010. doi: 10.1103/RevModPhys.82.1155.

[23] W. B. Case. The pumping of a swing from the standing position. *Am. J. Phys.* **64**, 1996.

[24] G. Grynberg, A. Aspect, and Fabre C. *Introduction to Quantum Optics*. Cambridge University Press, 2010.

[25] D. F. Walls and G. J. Milburn. *Quantum Optics*. Springer Verlag, Berlin, 2 edition, 2008.

[26] Ernst F. W Alexander. A magnetic amplifier for audio telephony.. *Proceedings of the Institute of Radio Engineers*. **4**, 1916.

[27] B. D. Josephson. Possible new effects in superconductive tunnelling. *Physics Letters*. **1**,(7), 251–253, July 1962. doi: 10.1016/0031-9163(62)91369-0. URL http://www.sciencedirect.com/science/article/B6X44-47RBX8S-5/2/31fc71946bd983d4a8fd06a69e777173.

[28] M. Tinkham. *Introduction to Superconductivity*. McGraw-Hill International Editions, 1996.

[29] Lev S. Bishop. *Circuit Quantum Electrodynamics: Volume II*. PhD thesis, Yale University, 2009.

[30] R.P. Feynman, M. Sands, and R.B. Leighton. *The Feynman Lectures on Physics Vol.3*. Addison-Wesley, 1971.

[31] M. Göppl. *Engineering Quantum Electronic Chips - Realization and Characterization of Circuit Quantum Electrodynamics Systems*. PhD thesis, ETH Zurich, 05 2009. URL http://qudev.phys.ethz.ch/content/science/thesis/dr_Goppl.pdf.

[32] T. Yamamoto, K. Inomata, M. Watanabe, K. Matsuba, T. Miyazaki, W. D. Oliver, Y. Nakamura, and J. S. Tsai. Flux-driven Josephson parametric amplifier. *Appl. Phys. Lett.* **93**,(4), 042510–3, July 2008. URL http://link.aip.org/link/?APL/93/042510/1.

[33] Christopher Eichler and Andreas Wallraff. Controlling the dynamic range of a josephson parametric amplifier. *EPJ Quantum Technology*. **1**,(1), 2, 2014. ISSN 2196-0763. doi: 10.1140/epjqt2. URL http://www.epjquantumtechnology.com/content/1/1/2.

[34] Johannes Fink. *Quantum nonlinearities in strong coupling circuit QED*. PhD thesis, ETH Zurich, 10 2010. URL http://qudev.phys.ethz.ch/content/science/Documents/phd/PhD_Thesis_Fink_17x24.pdf.

[35] Castellanos-Beltran. Bandwidth and dynamic range of a widely tunable Josephson parametric amplifier, 2009.

[36] H. A. Gersch and G. C. Knollman. Quantum cell model for bosons. *Phys. Rev.* **129**, 1963.

[37] Markus Greiner, Olaf Mandel, Tilman Esslinger, Theodor W. Hansch, and Immanuel Bloch. Quantum phase transition from a superfluid to a mott insulator in a gas of ultracold atoms. *Nature*. **415**,(6867), 39–44, January 2002. ISSN 0028-0836. URL http://dx.doi.org/10.1038/415039a.

[38] Matija Karalic. Characterization of coupled microwave resonator arrays. Master's thesis, ETH Zürich, 2014. URL http://qudev.phys.ethz.ch/content/science/Documents/semester/Matija_Karalic_semesterthesis_140127.pdf.

[39] Network analyzer basics. Technical report, Agilent technologies, 2004.

[40] Arjan van Loo. *Interactions in waveguide quantum electrodynamics*. PhD thesis, ETH Zurich, 2014.

[41] P.J. Petersan and S.M. Anlage. Measurement of resonant frequency and quality factor of microwave resonators: Comparison of methods. *J. Appl. Phys.* **84**, 1998.

[42] Gabriel Fernando Puebla-Hellmann. *DC, Microwave and Optical Measurement Schemes for Nano-Scale Devices*. PhD thesis, ETH Zurich, 01 2013. URL http://qudev.phys.ethz.ch/content/science/Documents/phd/PhD-Gabriel-Puebla-Hellmann.pdf.

Eidgenössische Technische Hochschule Zürich
Swiss Federal Institute of Technology Zurich

Declaration of originality

The signed declaration of originality is a component of every semester paper, Bachelor's thesis, Master's thesis and any other degree paper undertaken during the course of studies, including the respective electronic versions.

Lecturers may also require a declaration of originality for other written papers compiled for their courses.

I hereby confirm that I am the sole author of the written work here enclosed and that I have compiled it in my own words. Parts excepted are corrections of form and content by the supervisor.

Title of work (in block letters):

Josephson Parametric Amplifiers with Lumped-element Coupled Resonators

Authored by (in block letters):
For papers written by groups the names of all authors are required.

Name(s):	**First name(s):**
Rubio Abadal	Antonio

With my signature I confirm that

- I have committed none of the forms of plagiarism described in the 'Citation etiquette' information sheet.
- I have documented all methods, data and processes truthfully.
- I have not manipulated any data.
- I have mentioned all persons who were significant facilitators of the work.

I am aware that the work may be screened electronically for plagiarism.

Place, date	**Signature(s)**
Zürich, 27th of April 2015	

For papers written by groups the names of all authors are required. Their signatures collectively guarantee the entire content of the written paper.